

Phase Field Modeling of Static and Dynamic Wetting

vom Fachbereich Maschinenbau und Verfahrenstechnik
der Technischen Universität Kaiserslautern
zur Verleihung des akademischen Grades
Doktor-Ingenieur (Dr.-Ing.)
genehmigte Dissertation

von
Dipl.-Ing. Felix Diewald
aus Kaiserslautern

Hauptreferent:	Prof. Dr.-Ing. Ralf Müller
Korreferentin:	Prof. Dr. Bai-Xiang Xu
Vorsitzender:	Prof. Dr.-Ing. Hans Hasse
Dekan:	Prof. Dr.-Ing. Tilmann Beck

Tag der Einreichung:	16.10.2019
Tag der mündlichen Prüfung:	17.12.2019

Kaiserslautern, 2020

D 386

Herausgeber

Lehrstuhl für Technische Mechanik
Technische Universität Kaiserslautern
Gottlieb-Daimler-Straße
Postfach 3049
67653 Kaiserslautern

© Felix Diewald

Ich danke der „Prof. Dr. Hans Georg und Liselotte Hahn Stiftung“ für die finanzielle Unterstützung.

Druck

Technische Universität Kaiserslautern
Hauptabteilung 5 – Bau-Technik-Energie
Abteilung 5.6 – Foto-Repro-Druck

Alle Rechte vorbehalten, auch das des auszugsweisen Nachdrucks, der auszugsweisen oder vollständigen Wiedergabe (Photographie, Mikroskopie), der Speicherung in Datenverarbeitungsanlagen und das der Übersetzung.

ISBN 978-3-942695-19-0

Vorwort

Die vorliegende Arbeit entstand während meiner Tätigkeit als wissenschaftlicher Mitarbeiter am Lehrstuhl für Technische Mechanik der Technischen Universität Kaiserslautern.

Mein besonderer Dank gilt Herrn Professor Dr. Ralf Müller für die in jeder Hinsicht hervorragende Betreuung. Ich bedanke mich für das mir entgegengebrachte Vertrauen, die vielen hilfreichen Ratschläge in fachlichen und außerfachlichen Angelegenheiten, sowie die großen Freiräume für eigene Ideen.

Herrn Professor Dr. Hans Hasse danke ich für die zahlreichen konstruktiven wissenschaftlichen Diskussionen im Zuge unserer Projekttreffen, sowie für die Bereitschaft zur Übernahme des Vorsitzes der Promotionskommission. Frau Professorin Dr. Bai-Xiang Xu danke ich für das Interesse an meiner Arbeit, sowie für die bereitwillige Übernahme des Korreferates.

Mein herzlicher Dank gilt allen Mitarbeiterinnen und Mitarbeitern des LTM für das großartige Lehrstuhlklima. Danke für die gegenseitige Unterstützung, den fachlichen Austausch und die zahlreichen außeruniversitären Aktivitäten. Ich möchte mich besonders bei Frau Dr. Charlotte Kuhn für den engen fachlichen Austausch, sowie bei Frau Julia Hettesheimer und Herrn Dr. Christian Sator für die Übernahme zahlreicher organisatorischer Angelegenheiten bedanken. Herrn Oscard Teto, Herrn Raphael Bilz, Herrn Matthias Gellrich, Herrn Lennart Kneip und Herrn Marco Hoffmann danke ich für ihre studentischen Arbeiten.

Den Mitarbeiterinnen und Mitarbeitern des SFB 926 danke ich für den intensiven fachlichen Austausch über die Grenzen der Fachbereiche hinweg. Mein besonderer Dank gilt Frau Michaela Heier, Herrn Juniorprofessor Dr. Kai Langenbach, Herrn Dr. Martin Horsch und Herrn Dr. Martin Lautenschläger. Herrn Professor Dr. Kristoffer van der Zee danke ich für seine Gastfreundschaft und den fachlichen Austausch während meines Forschungsaufenthaltes in Nottingham.

Ich danke meiner Frau und meinem Sohn, meinen Brüdern und meinen Eltern für ihre Unterstützung auf meinem Lebensweg.

Kaiserslautern, im Januar 2020

Felix Diewald

Abstract

This work describes the development of a continuum phase field model that can describe static as well as dynamic wetting scenarios on the nano- and microscale.

The model reaches this goal by a direct integration of an equation of state as well as a direct integration of the dissipative properties of a specific fluid, which are both obtained from molecular simulations. The presented approach leads to good agreement between the predictions of the phase field model and the physical properties of the regarded fluid.

The implementation of the model employs a mixed finite element formulation, a newly developed semi-implicit time integration scheme, as well as the concept of hyper-dual numbers. This ensures a straightforward and robust exchangeability of the constitutive equation for the regarded fluid.

The presented simulations show good agreement between the results of the present phase field model and results from molecular dynamics simulations. Furthermore, the results show that the model enables the investigation of wetting scenarios on the microscale. The continuum phase field model of this work bridges the gap between the molecular models on the nanoscale and the phenomenologically motivated continuum models on the macroscale.

Kurzfassung

Die vorliegende Arbeit beschreibt die Entwicklung eines Kontinuum-Phasenfeldmodells, welches eine Beschreibung des statischen sowie dynamischen Benetzungsverhaltens von Tropfen auf der Nano- und Mikroskala erlaubt.

Das Modell erreicht dieses Ziel durch die direkte Integration einer Zustandsgleichung sowie die direkte Integration der dissipativen Eigenschaften eines bestimmten Fluids, welche beide aus molekularen Simulationen gewonnen werden. Der vorgestellte Ansatz führt zu einer guten Übereinstimmung zwischen den Vorhersagen des Phasenfeldmodells und den physikalischen Eigenschaften des betrachteten Fluids.

Die Implementierung des Modells bedient sich einer gemischten Finite-Elemente-Formulierung, eines neu entwickelten semi-impliziten Zeitintegrationsschemas sowie des Konzeptes der hyper-dualen Zahlen. Dies ermöglicht einen raschen und reibungslosen Austausch der konstitutiven Gleichung des betrachteten Fluids.

Die vorgestellten Simulationen zeigen eine gute Übereinstimmung der Ergebnisse des vorliegenden Phasenfeldmodells mit Ergebnissen aus Molekulardynamik-Simulationen. Darüber hinaus zeigen die Ergebnisse, dass das Modell die Untersuchung von Benetzungsszenarien auf der Mikroskala ermöglicht. Das Kontinuum-Phasenfeldmodell dieser Arbeit schließt die Lücke zwischen den molekularen Modellen auf der Nanoskala und den phänomenologisch motivierten Kontinuum-Modellen auf der Makroskala.

Contents

1	Introduction	1
1.1	Motivation	1
1.2	Scope and Objective of this Work	2
1.3	Structure of this Work	4
2	Fundamentals of Wetting	7
2.1	Interfaces and Surface Tension	7
2.2	Contact Angle	9
2.3	Wetting States on Rough Surfaces	10
3	Phase Field Modeling of Wetting	13
3.1	The Phase Field Approach	13
3.2	The Concept of Stress	16
3.3	Balance Laws	17
3.3.1	Mass Balance	18
3.3.2	Linear and Angular Momentum Balance	19
3.3.3	Energy Balance	20
3.3.4	Entropy Balance	20
3.4	Model Derivation	21
3.4.1	Mass, Momentum, Energy, and Entropy Balance	21
3.4.2	Coleman-Noll Procedure	23
3.4.3	Global Energy Dissipation Relation	27
3.5	Static Case	27
3.5.1	Derivation from the General Model	28
3.5.2	Equivalence to the Variational Formulation	30
4	Choices for the Helmholtz Free Energy and Viscosity	33
4.1	Empirical Helmholtz Free Energy	33
4.2	Equation of State Based Helmholtz Free Energy	38
4.3	Viscosity	49

5	FE Implementation	53
5.1	Temporal Discretization	54
5.1.1	Backward Euler Scheme	54
5.1.2	Semi-Implicit Energy Stable Scheme	57
5.2	Weak Form and Spatial Discretization	63
5.2.1	Dynamic Navier-Stokes-Korteweg Model	66
5.2.2	Static Allen-Cahn Model	70
5.3	Hyper-Dual Numbers	73
6	Numerical Results	77
6.1	Static Scenarios using the empirical Helmholtz Free Energy	77
6.1.1	Wetting of Plane Surfaces	78
6.1.2	Wetting of Structured Surfaces	79
6.1.3	Stability of the Solution	81
6.2	Static Scenarios using the EoS based Helmholtz Free Energy	89
6.2.1	Phase Separation	89
6.2.2	Planar Interface	90
6.2.3	Liquid Droplet in Vapor Phase	93
6.3	Dynamic Scenarios using the EoS based Helmholtz Free Energy	98
6.3.1	Wetting of Structured Surfaces	98
6.3.2	Droplets on Surfaces with Wettability Gradient	99
6.3.3	Semi-Implicit Time Integration Scheme	106
7	Scale Bridging	113
7.1	Adaption of the Equation of State Based Helmholtz Free Energy	113
7.2	Droplet on Tilted Surface with Wettability Gradient	116
8	Conclusion and Outlook	121
A	Details of the Continuous Global Energy Dissipation Relation	125
B	Details of the Discrete Global Energy Dissipation Relation	127
C	Details of the Analytic Total Phase Field Potential	131
	Bibliography	133

List of Symbols and Abbreviations

Latin Letters

A	surface area of an interface
a^e	function for the local part of the empirical Helmholtz free energy per mass
a_{ij}	parameter of the viscosity correlation
a^{PeTS}	local part of the Helmholtz free energy per mass based on the PeTS EoS
$B_I^{\vec{v}}$	B-matrix for \vec{v} and node I
B_I^μ	B-matrix for μ and node I
B_I^ρ	B-matrix for ρ and node I
\vec{b}	volume force
\vec{b}_0	non-conservative volume force
c	constant
c_1^{scal}	constant for the local part of the scaled Helmholtz free energy per mass
c_2^{scal}	constant for the local part of the scaled Helmholtz free energy per mass
c^{tint}	scalar quantity depending on the time integration scheme and Δt
D	damping matrix
D_{IJ}^{ab}	submatrix of the damping matrix
E	energy
e	counter
e_{tol}	tolerance for abandoning the evolution equation
\vec{e}_g	gravitational orientation

F	phase field potential
F_d	analytic phase field potential for droplet in vapor phase
F_h	analytic phase field potential for homogeneous density distribution
\vec{f}^s	entropy flux
$\vec{f}^{\mathcal{A}}$	flux of \mathcal{A}
f_1	local part of the phase field potential density
f_2	gradient dependent part of the phase field potential density
$d\vec{f}$	stress resultant force
G	non-linear function
g	gravitational acceleration
H^n	constant from time step n
h	interpolation function
h^n	constant from time step n
h_1	constant
h_2	constant
I	counter
i	counter
\mathbf{J}	Jacobian matrix
J	counter
j	counter
\mathbf{K}	stiffness matrix
K	curvature
K_{IJ}^{ab}	submatrix of the stiffness matrix
k	counter for the Newton-Raphson iteration
k_B	Boltzmann constant
l	length
l^e	interface width for empirical Helmholtz free energy

l^{scal}	interface width for scaled Helmholtz free energy
l^{t}	interface width computed by tangent construction
l^{10-90}	interface width computed by 10 – 90 thickness
M	parameter for evolution equation
M^{LJ}	mass per particle
m	mass
$m_{\mathcal{B}}$	mass in \mathcal{B}
N_I	shape function with value 1 at node I
$N_I^{\vec{v}}$	shape function for \vec{v} with value 1 at node I
N_I^{λ}	shape function for λ with value 1 at node I
N_I^{μ}	shape function for μ with value 1 at node I
N_I^{ρ}	shape function for ρ with value 1 at node I
n	current time step
n_{b}	number of finite element boundary edges
n_{dof}^{ρ}	number of global degrees of freedom for ρ
n_{e}	number of finite elements
n_{n}	number of nodes per element
n_{p}	number of quadrature points
\vec{n}	outer normal unit vector
p	counter
\mathbf{p}^{h}	hydrostatic pressure tensor
p^{h}	hydrostatic pressure
p_{l}^{h}	hydrostatic pressure of liquid phase
p_{v}^{h}	hydrostatic pressure of vapor phase
p^{s}	entropy production
p^{scal}	scaling factor
$\mathbf{p}^{\gamma_{\text{lv}}}$	surface tension pressure tensor

$p^{\mathcal{A}}$	production of \mathcal{A}
q	heat supply
\vec{q}	heat flux
\vec{R}	global residual vector
\vec{R}_I	nodal residual vector for node I
$\vec{R}_I^{\vec{v}}$	residual of momentum balance for node I
R_I^{μ}	residual of equation for chemical potential for node I
R_I^{ρ}	residual of mass balance for node I
R^{λ}	residual of conservation of mass
\vec{R}^{ρ}	global residual vector for ρ
r	radius
r_e	equimolar radius
r_{ini}	initialization radius
r^{LJ}	distance between two particles
r_c^{LJ}	cut-off radius for the LJTS potential
\mathbf{S}	system matrix
\mathbf{S}_{sol}	system matrix for solution state
S_{IJ}^{ab}	submatrix of the system matrix
s	entropy per mass
s^s	entropy supply
$s^{\mathcal{A}}$	supply of \mathcal{A}
\vec{s}	eigenvector
T	absolute temperature
t	time
t_r	total computational runtime
\vec{t}	Cauchy stress vector
\vec{u}	global degree of freedom vector

u^{LJ}	LJ potential
u^{LJTS}	LJTS potential
\vec{v}	velocity vector
$\vec{v}_{\partial\mathcal{B}_s}^\perp$	normal velocity on $\partial\mathcal{B}_s$
$\vec{v}_{\partial\mathcal{B}_s}^{\text{tan}}$	tangential velocity on $\partial\mathcal{B}_s$
$\delta\vec{v}$	test function
w_p	weight for quadrature point p
x	coordinate
x_c	x -coordinate of the centroid
x_g	gravitational height
\vec{x}	position in space
y	coordinate

Greek Letters

α	angle
α^e	factor for the local part of the empirical Helmholtz free energy per mass
α^s	stabilization parameter for the convex-concave splitting
α^{scal}	factor for the local part of the scaled Helmholtz free energy per mass
β^e	factor for the gradient part of the empirical Helmholtz free energy per mass
β^s	stabilization parameter for the convex-concave splitting
β^{scal}	factor for the gradient part of the scaled Helmholtz free energy per mass
γ_{lv}	liquid-vapor surface tension
γ_{sl}	solid-liquid surface tension
γ_{sv}	solid-vapor surface tension
ε	internal-energy per mass
ε^{LJ}	energy parameter of the LJ potential
ϵ_1	imaginary unit

ϵ_2	imaginary unit
η	(natural) coordinate
η^v	viscosity
Θ	contact angle
κ	factor for the gradient part of the EoS based Helmholtz free energy per mass
Λ	eigenvalue
λ	Lagrange multiplier
$\delta\lambda$	test function
μ	chemical potential
μ'	chemical potential in a homogeneous liquid phase
$\delta\mu$	test function
ξ	(natural) coordinate
$\vec{\xi}$	position in space in natural coordinates
$\vec{\xi}_p$	position of quadrature point p
ρ	mass density
ρ'	mass density of liquid phase
ρ''	mass density of vapor phase
ρ_l	mass density of liquid phase for non-planar interfaces
ρ_v	mass density of vapor phase for non-planar interfaces
ρ_η^n	density value between ρ^n and ρ^{n+1}
ρ_ξ^n	density value between ρ^n and ρ^{n+1}
$\vec{\rho}$	global degree of freedom vector for ρ
$\delta\rho$	test function
σ	Cauchy stress tensor
σ^v	viscous stress tensor
σ^ψ	Korteweg stress tensor
σ^{LJ}	size parameter of the LJ potential

ϕ	surface energy per mass
ϕ^e	surface energy per mass for the empirical Helmholtz free energy
ϕ^{PeTS}	surface energy per mass for Helmholtz free energy based on the PeTS EoS
φ	order parameter
φ'	value of φ in (liquid) bulk phase
φ''	value of φ in (vapor) bulk phase
ψ	Helmholtz free energy per mass
ψ^e	empirical Helmholtz free energy per mass
ψ^{PeTS}	Helmholtz free energy per mass based on the PeTS EoS
ψ^{scal}	Helmholtz free energy per mass based on the PeTS EoS and scaled
Ω^e	excess free energy for empirical Helmholtz free energy
Ω^{PeTS}	excess free energy for Helmholtz free energy based on the PeTS EoS
Ω^{scal}	excess free energy for scaled Helmholtz free energy
ω	homogeneous excess free energy density

Letterlike Symbols

\mathcal{A}	physical quantity
\mathcal{B}	domain fixed in space
\mathcal{B}_e	finite element
\mathcal{B}_t	material volume
\mathcal{B}_\square	reference element
$\partial\mathcal{B}$	boundary of \mathcal{B}
$\partial\mathcal{B}_e$	finite element edge on boundary
$\partial\mathcal{B}_s$	solid surface
$\partial\mathcal{B}_t$	boundary of \mathcal{B}_t

Other Denotations

$\mathbf{1}$	identity matrix
--------------	-----------------

\det	determinant
div	divergence
div_s	surface divergence
$\frac{d(\cdot)}{dt}$	material time derivative
Im	imaginary value
tr	trace
$\Delta(\cdot)$	increment of (\cdot)
$\delta_b a$	first variation of a with respect to b
∇	gradient
∇^s	symmetric gradient
\otimes	dyadic product
\times	cross product
\cdot	dot product
$:$	double contraction
$\dot{(\cdot)}$	material time derivative
$\hat{(\cdot)}$	denotes that an assumption for the dependencies of (\cdot) was made
$(\cdot)^*$	denotes that (\cdot) is nondimensionalized
$(\cdot)_e$	interpolated value of (\cdot) within a finite element
$(\cdot)_{\text{HD}}$	hyper-dual number, real value $(\cdot)_0$, imaginary values $(\cdot)_1, (\cdot)_2, (\cdot)_{12}$
$(\cdot)_I$	value of (\cdot) at node I
$(\cdot)_J$	value of (\cdot) at node J
$ \cdot $	Euclidean norm

Abbreviations

BE	backward Euler
EoS	equation of state
FE	finite element

LJ Lennard-Jones

LJTS Lennard-Jones truncated and shifted

MD molecular dynamics

PeTS perturbed truncated and shifted

PF phase field

SI semi-implicit

1 Introduction

1.1 Motivation

More than 70,000 years ago, wetting scenarios were important for early humans who wore clothes as weather protection during the ice ages [Balter 2009]. Fiber discoveries in Georgia suggest that humans were even engaged in dyeing their clothes more than 30,000 years ago [Kvavadze et al. 2009]. The ability of humans to control the process of wetting for their own benefit has increased ever since. Modern humans apply controlled wetting on a daily basis for washing, cleaning, or when using a fountain pen.

To control and understand wetting processes does also play an important role in engineering applications. Many examples are given in [Law and Zhao 2016]. The applications include the development of self-cleaning surfaces, anti-corrosion surfaces, anti-icing surfaces, microfluidic devices, cooling or heating control, coating, and printing. Nowadays, printing is not only used in the classical fashion to place ink on paper but also to manufacture printed electronics like thin-film-transistor arrays and solar cells.

The wetting behavior of a droplet on a solid surface respectively a machine component is determined by the properties of the fluid (liquid and vapor phase) as well as by the morphology of the surface itself. To gain more insights on how they can be used to control and understand wetting, the fluid properties and surface morphology on the microscale are in the scope of current research efforts. In the Collaborative Research Centre 926 [CRC 926 2018], that is installed at the Technische Universität Kaiserslautern, the relation between surface creation, morphology and properties (SCMP) is investigated on the microscale. One of these properties is the surface wettability. Modern manufacturing techniques like micro-milling [Bohley et al. 2018], micro-grinding [Arrabiyeh et al. 2017], or additive manufacturing on the microscale [Hering et al. 2018] allow to produce surfaces with a defined microstructure. However, to define the requirements on how the structure of a surface should be manufactured in order to yield a defined wettability, the rela-

tion between the microstructure and the wettability has to be understood on the microscale first. The same is true for the other aspects of the surface morphology, i.e. the physical and chemical properties.

To predict the wettability of a given morphology or to optimize a morphology with respect to a certain wetting behavior in a time and resource efficient manner, numerical models that are accurate on the microscale are of utmost importance. In general, numerical models for the microscale can be derived from two different directions [CRC 926 2018]. The first approach, that is typical for the field of engineering, uses phenomenological models that were originally developed for the macroscale and adapts them such that they include microscale phenomena. This approach leads to moderate computational effort, but brings the necessity to introduce many assumptions which can weaken the accuracy. The second approach, that is typical for the field of physics, starts from a molecular description on the nanoscale and tries to reach the microscale by increasing the size of the computational domain. This approach leads to predictions with a high accuracy if the appropriate potential is chosen, but also to a very high computational effort. The motivation of the present work is to unite both approaches, to combine the advantages and circumvent the disadvantages.

1.2 Scope and Objective of this Work

The present work reports on the development of a continuum phase field (PF) model that can describe wetting scenarios on the nanoscale with a strong physical foundation and in agreement with molecular dynamics (MD) simulations. As the computational effort for the PF model is small compared to the computational effort of classical molecular models, it allows to investigate wetting scenarios on the microscale. It therefore bridges the gap between the molecular models on the nanoscale and the phenomenological continuum models on the macroscale, cf. Figure 1.1.

This is achieved by developing the PF model such that it directly inherits information from nanoscale MD simulations, i.e. an equation of state (EoS) and dissipative properties for a specific fluid, as well as an energetic description of the solid surface. This modeling approach is based on the balance laws and combines aspects from engineering mechanics, fluid mechanics and thermodynamics.

The implementation of the model allows to exchange the specific fluid for which the model is formulated in a robust and resource efficient manner. To demonstrate the approach by means of a specific example, the Lennard-Jones truncated and shifted (LJTS) fluid is chosen as a model fluid. The nanoscale properties of the

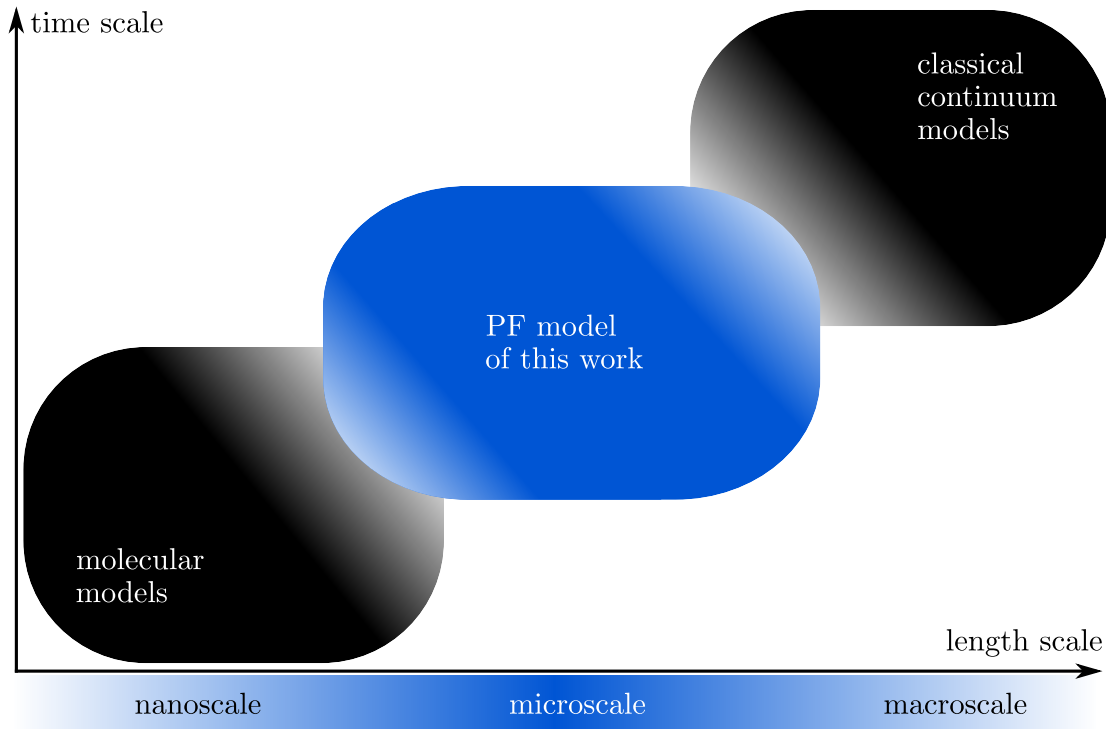


Figure 1.1: Sketch: The PF model of this work bridges the gap between molecular models on the nanoscale and phenomenological continuum models on the macroscale.

PF model for the LJTS fluid are validated by means of comparison to MD results. Once the physical validity on the nanoscale is ensured, a scale bridging can be applied such that the PF model can be used to compute wetting scenarios with the LJTS fluid for larger and more complex scenarios, cf. Figure 1.2.

Pioneering contributions to the foundation of PF models were made by Cahn and Hilliard [1958], Cahn and Allen [1977], and van der Waals [1979]. See [Moelans et al. 2008] for more information on the general history of PF models. PF Models that deal with fluids and wetting scenarios can be found in [Ben Said et al. 2014; Braack and Prohl 2013; van Brummelen et al. 2017; Bueno and Gomez 2016; Bueno et al. 2018; Diehl et al. 2016; Gomez et al. 2010; Kunti et al. 2018a; Lamorgese and Mauri 2009; Liu et al. 2013, 2015; Onuki 2007; Pecenko et al. 2010, 2011; Schweigler et al. 2017; Shokrpour Roudbari et al. 2018; Tian et al. 2015; Wang et al. 2015; Weyer et al. 2015; Wu et al. 2019; Xiao et al. 2018; Yang et al. 2006; Yurkiv et al. 2018], to name a few. However, the models do either obtain their information on the nanoscale behavior by empirical expressions or by employing an EoS that does not have a strong nanoscale foundation. More specifics are given

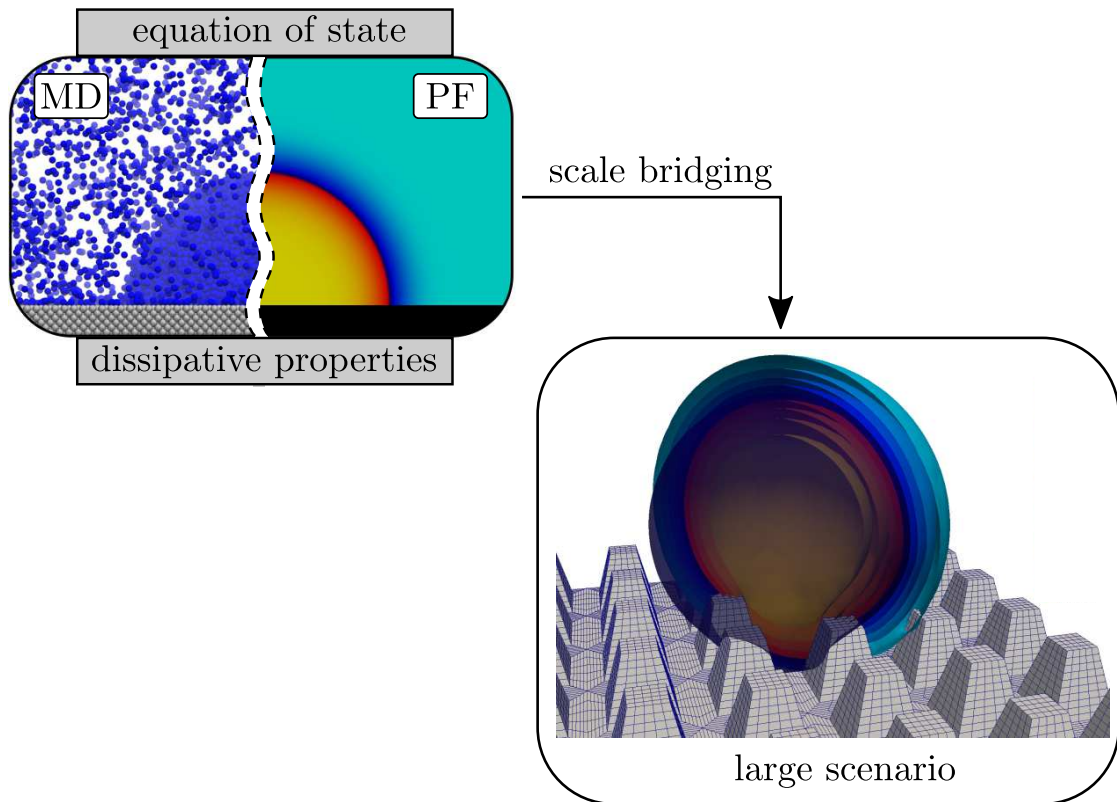


Figure 1.2: The PF model is connected to MD simulations by an equation of state and dissipative properties. Both are obtained from MD simulations. After a validation of the PF results on the nanoscale, a scale bridging can be applied in order to enable the investigation of larger and more complex scenarios.

in the corresponding chapters. The present work combines a cohesive derivation of a PF model for wetting with a direct connection to the nanoscale fluid behavior as obtained from MD simulations.

1.3 Structure of this Work

Chapter 2 introduces the reader to the fundamentals of wetting. It gives a brief overview covering surface tension, contact angle, as well as wetting states on rough surfaces.

Chapter 3 presents the theoretical foundation of this work. A concise recollection of the concepts necessary to follow the derivation of the model of this work is given. Thereafter, the derivation of the PF model of this work is presented in detail. Up

to this point the elaborations are not fluid specific.

Chapter 4 defines the specific fluids that are investigated in this work and integrates them into the general model of the previous chapter. After the introduction of a purely phenomenologically motivated test fluid, the integration of the LJTS fluid by means of including the corresponding EoS is presented.

Chapter 5 gives details on the implementation of the PF model in a finite element (FE) context. Besides a mixed FE formulation and a newly developed energy stable semi-implicit time integration scheme, the implementation applies the concept of hyper-dual numbers to ensure a straightforward and robust exchangeability of the specific fluid under consideration.

Chapter 6 shows the numerical results obtained with the PF model. After demonstrating that the phenomenologically motivated test fluid can reproduce basic wetting configurations, the implementation of the LJTS fluid is validated by a comparison of PF results to MD results for various scenarios. In addition, a post-processing method, that investigates the stability of the static equilibrium configuration and can be beneficial to other PF models, as well as the properties of the energy stable semi-implicit time integration scheme are shown.

Chapter 7 demonstrates how the scale bridging can be achieved. Details of the approach are followed by a numerical example for methane.

Chapter 8 concludes the present work and gives an outlook on future tasks and challenges that can be ventured into.

Some of the elaborations and results of this work have previously been published in international journals [Diewald et al. 2016; Diewald et al. 2017; Diewald et al. 2018a; Diewald et al. 2018b; Diewald et al. 2019; Diewald et al. 2020a; Heier et al. 2019; Schlüter et al. 2017] or are in preparation for publication [Diewald et al. 2020b]. The papers are cited at the respective positions. Student theses that supported the present work were done by [Becker 2015; Bilz 2018; Blauwhoff 2015; Gellrich 2019; Kneip 2019; Teto 2018]. They are cited where appropriate.

2 Fundamentals of Wetting

A brief introduction to the fundamentals of wetting is given in the following. For more details, readers are referred to the book of Law and Zhao [2016] which also lists many references for further reading.

2.1 Interfaces and Surface Tension

Every day of our lives we are confronted with interfaces. Our interaction with the world heavily relies on the interfaces between our bodies and other objects, matter, or people. Interfaces play a central role in engineering applications as well. The surface of a machine component is its interface to its surrounding and does strongly determine the machine component's technical properties. Besides such interfaces between different matter or materials there are also interfaces between different states of the same matter. One example are liquid-vapor interfaces.

Liquid-vapor interfaces exhibit a tendency to contract. This (so-called) surface tension causes droplets that are not influenced by external forces to form spherical shapes [Davies and Rideal 1963]. The research efforts to understand this phenomenon in terms of attractive and repulsive forces date back to Young [1805]. It is found by Poisson [1831] that surface tension can only be fully understood if in reality the interface between the liquid and the vapor bulk phase is not sharp but characterized by a steep, thus continuous, transition of the density [Rowlinson and Widom 1982].

Along these lines an explanation of the surface tension can be given. Each fluid particle is affected by repulsive and attractive forces caused by the interaction with the particles in its surroundings. The repulsive forces can by good approximation be understood as contact forces. The repulsive interaction of particles is therefore short ranged. It is only sensitive to the particle density in the immediate vicinity but not to a gradual change of the particle density. Thus, the repulsive interaction is isotropic. In contrast, the attractive particle interaction is long ranged. Within

regions that show a gradual change of the particle density, e.g. within the liquid-vapor interface, the number of interaction partners is different in each direction. Thus, the attractive interaction can be strongly anisotropic within the liquid-vapor interface. The component of the pressure in a given direction is calculated by imaginarily cutting the fluid by a plane perpendicular to this direction. The time average of the sum of repulsive and attractive forces per area that the two halves of the fluid exert on each other gives the pressure in that direction. Considering a (static) equilibrium configuration of a liquid and a vapor bulk phase with a planar interface between them, the following is found. In the bulk phases, where both the repulsive and attractive interactions are isotropic, the pressure is isotropic as well and has the same value in the liquid and the vapor phase. Within the interface, the pressure component tangential to the interface decreases while the pressure component normal to the interface stays constant. This is explained as follows. The pressure component normal to the interface is obtained by moving an imaginary cut plane that is parallel to the interface from the liquid to the vapor phase. Within the interface the liquid density decreases until it reaches the vapor density. Consequently, the repulsive forces decrease as well. Since there is no movement of the interface, the attractive forces have to decrease identically. The pressure component tangential to the interface is obtained by placing the imaginary cut plane perpendicular to the interface. As they are isotropic, the repulsive forces show the same decrease as for the pressure component normal to the interface. However, the anisotropic, long ranged attractive forces find more interaction partners than for the pressure component normal to the interface and therefore decrease slower. The fast decrease of the repulsive forces in combination with the slower decrease of the attractive forces results in a net decrease of the pressure within and tangential to the interface. The integral over that pressure drop in the direction normal to the interface is referred to as the surface tension. From the above it is clear that surface tension is a force per length. [Berry 1971; Marchand et al. 2011]

A more straightforward, though maybe a bit less satisfactory, approach to understand the origin of surface tension can be given as follows. Basic experiments show that a fluid inside a receptacle can form separated liquid and vapor bulk phases instead of a homogeneous density distribution for certain combinations of the number of particles inside the receptacle, the receptacle size, and temperature. Evidently, the liquid and vapor bulk states are energetically more favorable than the homogeneous density distribution for such ensembles. Within the interface the density changes from the liquid bulk density to the vapor bulk density and does therefore pass through energetically less favorable states. The minimization of the free energy consequently leads to a minimization of the interface area, which can also be understood as the existence of a surface tension acting to contract

the interface. The excess free energy, i.e. the energy that is stored in the interface is given by the product of the surface tension and the interface area. Note that the expression “interface area” is misleading given the diffuse character of the interface. However, due to the steep transition of the density, the liquid-vapor interface is often treated as a surface and the usage of “interfacial volume” is not very common.

If the interface is curved, the existence of surface tension consequently causes a difference between the hydrostatic pressure in the liquid and in the vapor phase. For a spherical droplet this pressure difference Δp^h follows from a simple balance of forces,

$$\Delta p^h = \frac{2\gamma_{lv}}{r}, \quad (2.1)$$

with γ_{lv} and r denoting the liquid-vapor surface tension and radius of the droplet, cf. Figure 2.1 (a). This relation is referred to as (Young-)Laplace equation [Kalikmanov 2013].

2.2 Contact Angle

In the case of a droplet that is in contact with a solid surface, three interfaces can be distinguished:

1. The liquid-vapor interface with surface tension γ_{lv} .
2. The solid-liquid interface with surface tension γ_{sl} .
3. The solid-vapor interface with surface tension γ_{sv} .

At the contact line, where the three interfaces meet, a contact angle Θ develops between the liquid-vapor and the solid-liquid interface, cf. Figure 2.1 (b). Again, the terminology with the usage of the word “line” is misleading. The term solid-fluid interface is used to denote the consolidation of the solid-liquid and the solid-vapor interface. The relation between the surface tensions and the contact angle is given by

$$\cos \Theta = \frac{\gamma_{sv} - \gamma_{sl}}{\gamma_{lv}}. \quad (2.2)$$

Though he did not state the explicit equation in his work, this relation goes back to Young [1805] and is called Young’s equation. The phenomenon of line tension at the contact line of the three interfaces is not discussed here. Interested readers are referred to e.g. [Amirfazli et al. 1998; Amirfazli and Neumann 2004; Marmur 1997].

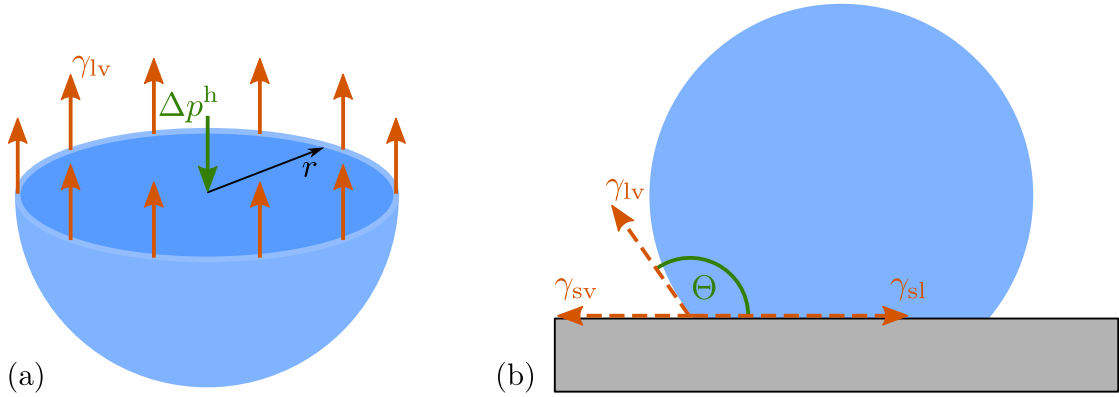


Figure 2.1: (a): Spherical droplet cut in half. The green arrow depicts the resultant pressure difference Δp^h on the cut plane. The balance of forces yields a positive value for Δp^h according to (2.1), i.e. the hydrostatic pressure in the liquid phase is larger than in the vapor phase. (b): Droplet on solid surface with contact angle Θ .

2.3 Wetting States on Rough Surfaces

For the wetting of rough surfaces, two main wetting states are observed. They distinguish themselves by the type of contact between the liquid and the solid surface. In the Wenzel state [Wenzel 1936], the liquid fully wets the rough surface, i.e. the droplet sinks into the structure of the surface. In the Cassie-Baxter state [Cassie and Baxter 1944], the droplet does not sink into the structure of the surface. Instead the droplet sits on top of the structure such that vapor pockets trapped by the liquid and the solid surface remain. Figure 2.2 shows a comparison of the Wenzel wetting state (a) and the Cassie-Baxter wetting state (b).

In addition to defining the wetting states, Wenzel as well as Cassie and Baxter also derived expressions for the dependency of the contact angle on the roughness of the surfaces. These expressions employ the true area of the solid-liquid interface (enlarged by the roughness) or the area fraction of the solid surface underneath the droplet that is actually in contact with the liquid. However, since the contact angle is determined by the contact line of the three interfaces and not by the interface area, these expressions are called into question in the literature. The cases in which the predictions for the contact angle agree with experiments are often regarded as fortuities [Law and Zhao 2016]. A vivid summary of the debate can be found in [Law and Zhao 2016].

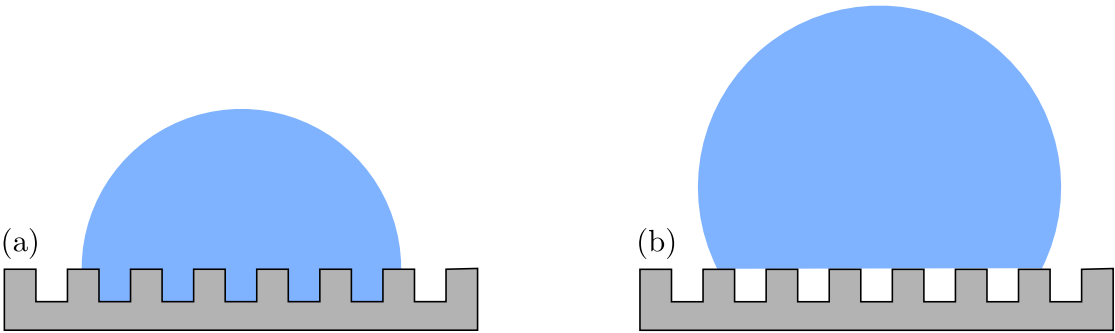


Figure 2.2: (a): Wenzel wetting state. (b): Cassie-Baxter wetting state.

3 Phase Field Modeling of Wet- ting

This chapter introduces the underlying phase field (PF) model of this work. After an introduction to the PF approach, the concept of stress and the balance laws are briefly recollected. Thereafter, a detailed derivation of the PF model, which is build up on the balance laws and utilizes the Coleman-Noll procedure, is given. The general model which can be used for dynamic wetting scenarios is then simplified for the case of static wetting.

3.1 The Phase Field Approach

PF models are used in numerous research fields. Among others they are used for the investigation of solidification [Beckermann et al. 1999; Nestler et al. 2005], solid-state phase transformation [Schmitt et al. 2017; Schmidt et al. 2017] and crack propagation [Kuhn and Müller 2010; Schlüter et al. 2017; Xu et al. 2010]. A broader overview can be found in [Moelans et al. 2008] and the references therein. PF models have two main characteristics:

1. They use at least one order parameter which distinguishes between different phases.
2. The interface between the phases is not sharp but diffuse. The value of the order parameter changes continuously from one phase to the other.

An advantage of the diffuse interface PF approach over sharp interface approaches is that they allow to investigate complex interface morphologies without the need of special interface tracking methods.

The key component for a PF model is the formulation of the potential F for the

domain \mathcal{B} under consideration

$$F = \int_{\mathcal{B}} f_1(\varphi) + f_2(\nabla\varphi) \, dV. \quad (3.1)$$

It consists of two parts. The first part $f_1(\varphi)$ depends on the local value of the order parameter $\varphi(\vec{x}, t)$ and the second part $f_2(\nabla\varphi)$ on the local gradient of the order parameter $\nabla\varphi(\vec{x}, t)$. Here \vec{x} and t designate the position in space and time. The exact forms of f_1 and f_2 used in this work are discussed in chapter 4. Many PF models choose a double-well potential for $f_1(\varphi)$, cf. Figure 3.1 (left), and $f_2(\nabla\varphi) = \frac{1}{2}\kappa|\nabla\varphi|^2$. In this, $\kappa > 0$ is a positive constant and $|\cdot|$ the Euclidean norm. The static solution is given by the first order optimality condition

$$\delta_\varphi F = 0. \quad (3.2)$$

Here, $\delta_\varphi F$ is the first variation of F with respect to φ . Consequently, using only $f_1(\varphi)$ would lead to sharp interfaces between infinitely often alternating bulk phases φ' and φ'' . As $f_2(\nabla\varphi)$ strives to eliminate steep gradients of the order parameter, the combination of $f_1(\varphi)$ and $f_2(\nabla\varphi)$ can be used to adjust the width of the interface. A plot of the order parameter along an axis x perpendicular to a typical PF interface is sketched in Figure 3.1 (right).

In order to approach the static equilibrium (3.2), an evolution equation is used. Commonly, an Allen-Cahn evolution equation [Cahn and Allen 1977] (also known as Ginzburg-Landau evolution equation)

$$\frac{\partial\varphi}{\partial t} = -M \frac{\delta_\varphi F}{\delta\varphi} \quad (3.3)$$

or Cahn-Hilliard evolution equation (see e.g. [Gurtin 1996; Kim 2012])

$$\frac{\partial\varphi}{\partial t} = M \operatorname{div} \left[\nabla \left(\frac{\delta_\varphi F}{\delta\varphi} \right) \right] \quad (3.4)$$

is chosen. The parameter $M > 0$ is a positive constant and div the divergence.

This general set-up of a PF model can be coupled to other models depending on the type of application. In the field of PF models for fluids the PF model is coupled to the mass balance and momentum balance whenever not only the static equilibrium solution but the dynamic evolution of the fluid is of interest. This leads to the classification of PF models for fluids shown in Figure 3.2. The models computing the static equilibrium solution are named after their evolution equation: ‘‘Allen-Cahn’’ or ‘‘Cahn-Hilliard’’. If these two types of models are coupled to the mass balance and momentum balance but the evolution equation is still utilized, they

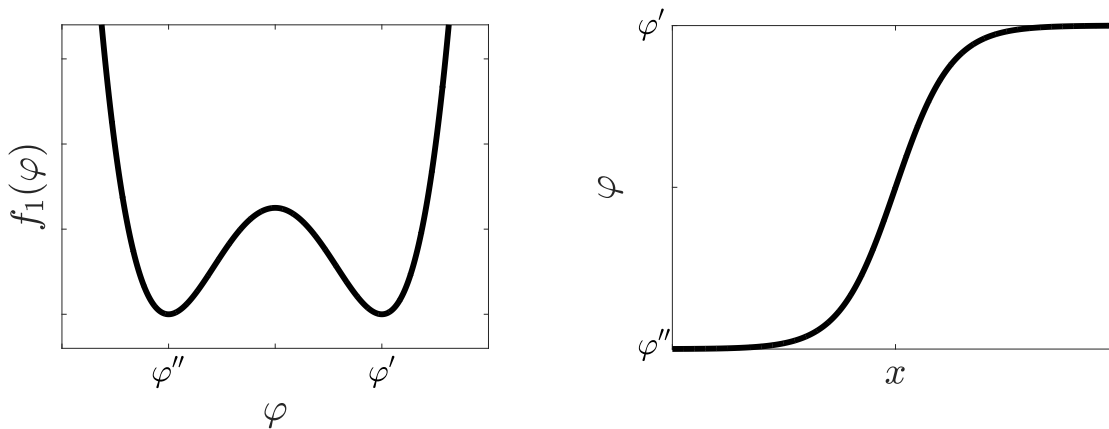


Figure 3.1: Sketch of a double-well potential (left) and change of the order parameter across the diffuse interface (right). The scale and dimensions depend on the type of application.

are referred to as “Navier-Stokes-Allen-Cahn” and “Navier-Stokes-Cahn-Hilliard” models. If the order parameter of the PF model is directly used as density in the mass balance and momentum balance without using an evolution equation, the resulting PF model is named “Navier-Stokes-Korteweg” model. This naming dates back to Korteweg, who described the capillary stress tensor on which the coupling is based in 1901 (see e.g. [Anderson et al. 1998]). The PF model of this work can be classified as a “Navier-Stokes-Korteweg” model. Section 3.4 presents a rational derivation of the general “Navier-Stokes-Korteweg” model. The static “Allen-Cahn” model is then derived by a simplification from the dynamic “Navier-Stokes-Korteweg” model, cf. section 3.5. For more details on the other models mentioned that are not discussed in this work, see e.g. [Gomez and van der Zee 2017].

The diffuse interface of a PF model is often seen as a regularization of a sharp interface where the sharp interface is regarded as the proper description of the physical world. For instance, a crack in a machine component is characterized by a sharp interface between material and no material. A PF model for crack propagation regularizes this interface [Kuhn 2013; Schlüter 2018]. However, it has to describe the properties of the sharp interface as accurate as possible. Therefore, many PF models are concerned with the so-called sharp interface limit beyond which the results do not depend on the width of the diffuse interface, see e.g. [Yue et al. 2010; Sibley et al. 2013]. In this work the order parameter is used to distinguish between the liquid and the vapor phase of a fluid. Since this interface is in the physical world not sharp but diffuse, this work takes the view that the PF model used here does not regularize a sharp interface but describes the regarding

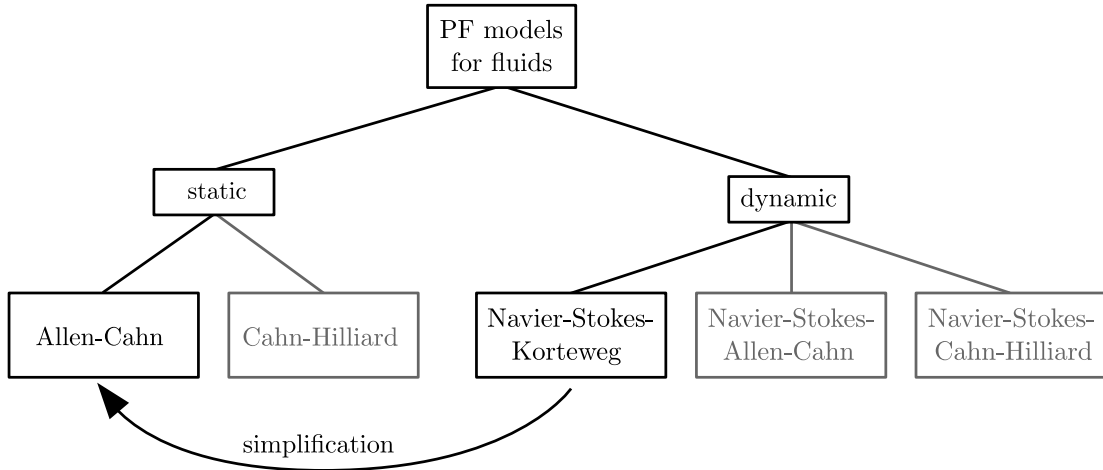


Figure 3.2: Classification of PF models for fluids. The models of relevance for this work are “Allen-Cahn” and “Navier-Stokes-Korteweg”. The static “Allen-Cahn” model can be derived from the dynamic “Navier-Stokes-Korteweg” model by a simplification, cf. section 3.5.

fluid-vapor interfaces more accurately according to their physical characteristics than a sharp interface model would do.

3.2 The Concept of Stress

This section gives a brief introduction to the concept of stress. For further reading the reader is referred to the textbooks of Becker and Gross [2002], Gurtin et al. [2010], and Holzapfel [2010].

A body with forces acting on its boundary surface is considered. Cutting the body by a plane surface, cf. Figure 3.3, it is evident that the two parts of the body interact with each other by internal forces. Focusing on a infinitesimal surface element dA on the cut plane, the resultant force $d\vec{f}$ of the interaction is given by

$$d\vec{f} = \vec{t} dA \quad (3.5)$$

with \vec{t} as the Cauchy stress vector. According to Cauchy’s (stress) theorem the stress vector \vec{t} can be computed from a (unique and symmetric) second order tensor $\boldsymbol{\sigma}$ by

$$\vec{t} = \boldsymbol{\sigma}^T \vec{n} \quad (3.6)$$

where $\boldsymbol{\sigma}$ is called Cauchy stress tensor. From the symmetry of $\boldsymbol{\sigma}$, cf. section 3.3.2 for details, it follows that

$$\vec{t} = \boldsymbol{\sigma} \vec{n}. \quad (3.7)$$

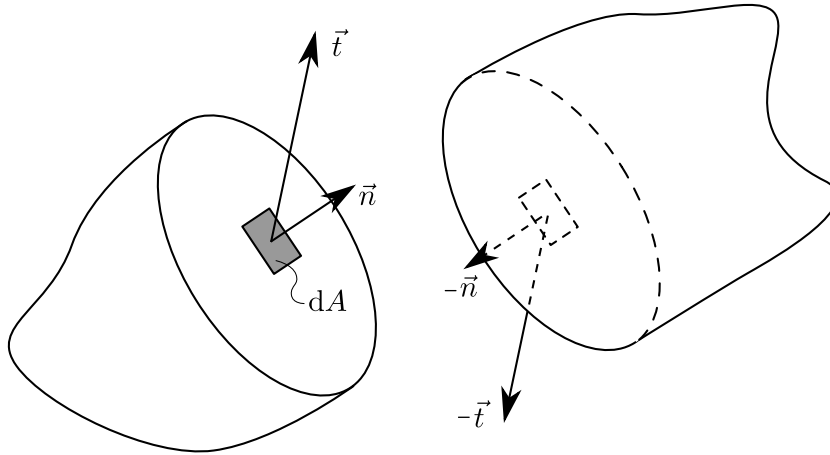


Figure 3.3: Body with arbitrary forces acting on its boundary surface cut by a plane surface. The two parts of the body interact with each other by internal forces.

As (3.6) or (3.7) allow to compute the stress vector \vec{t} for any cut plane and dA (with outer normal unit vector \vec{n}), σ describes the stress state of the body.

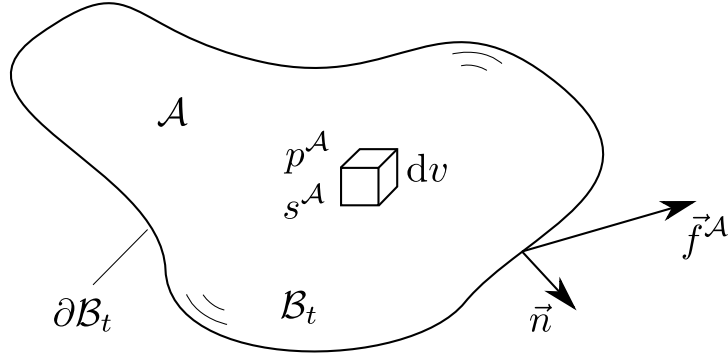
3.3 Balance Laws

As the derivation of the PF model of this work is based on the balance laws, this chapter gives a recollection of the mass balance, momentum balance, energy balance, and entropy balance. A more detailed discussion can be found in [Gurtin et al. 2010; Holzapfel 2010] on which this section is based.

The general form of a balance law is as follows. Regarding a material volume \mathcal{B}_t that consists of the same particles for all times t , the change over time of a physical quantity $\mathcal{A}(\vec{x}, t)$ within \mathcal{B}_t is given by

$$\frac{d}{dt} \left[\int_{\mathcal{B}_t} \mathcal{A}(\vec{x}, t) dv \right] = \int_{\mathcal{B}_t} [p^{\mathcal{A}}(\vec{x}, t) + s^{\mathcal{A}}(\vec{x}, t)] dv - \int_{\partial \mathcal{B}_t} \vec{f}^{\mathcal{A}}(\vec{x}, t) \cdot \vec{n} da. \quad (3.8)$$

In this, $p^{\mathcal{A}}(\vec{x}, t)$ and $s^{\mathcal{A}}(\vec{x}, t)$ are the production and supply of \mathcal{A} within \mathcal{B}_t . The flux across the boundary $\partial \mathcal{B}_t$ of the material volume \mathcal{B}_t is given by $\vec{f}^{\mathcal{A}}(\vec{x}, t)$, cf. Figure 3.4. In the further course of this section, the arguments (\vec{x}, t) are omitted. The material time derivative is denoted by $\frac{d(\cdot)}{dt} = (\dot{\cdot}) = \frac{\partial(\cdot)}{\partial t} + \nabla(\cdot) \cdot \vec{v}$, where \vec{v} is the velocity vector and \cdot the dot product. The outer normal unit vector to $\partial \mathcal{B}_t$ is given by \vec{n} .

Figure 3.4: Material volume \mathcal{B}_t with physical quantity \mathcal{A} .

Using Reynold's transport theorem

$$\begin{aligned} \frac{d}{dt} \left[\int_{\mathcal{B}_t} \mathcal{A} dv \right] &= \int_{\mathcal{B}_t} \left[\dot{\mathcal{A}} + \mathcal{A} \operatorname{div} \vec{v} \right] dv \\ &= \int_{\mathcal{B}_t} \left[\frac{\partial \mathcal{A}}{\partial t} + \operatorname{div} (\mathcal{A} \vec{v}) \right] dv, \end{aligned} \quad (3.9)$$

as well as the (Gauss) divergence theorem

$$\int_{\partial\mathcal{B}_t} \vec{f}^A \cdot \vec{n} da = \int_{\mathcal{B}_t} \operatorname{div} \vec{f}^A dv, \quad (3.10)$$

leads to the local form of the general balance law

$$\dot{\mathcal{A}} + \mathcal{A} \operatorname{div} \vec{v} = -\operatorname{div} \vec{f}^A + p^A + s^A. \quad (3.11)$$

3.3.1 Mass Balance

The physical quantity under consideration in the mass balance is the mass density ρ , therefore $\mathcal{A} \hat{=} \rho$. As a material volume that consists of the same number of particles for all times is considered, no production, supply, or flux exists, $p^A = s^A \hat{=} 0$ and $\vec{f}^A \hat{=} \vec{0}$. With this the global and local mass balance read

$$\frac{d}{dt} \left[\int_{\mathcal{B}_t} \rho dv \right] = 0 \quad (3.12)$$

and

$$\dot{\rho} + \rho \operatorname{div} \vec{v} = 0. \quad (3.13)$$

As a consequence of the mass balance it follows that

$$\frac{d}{dt} \left[\int_{\mathcal{B}_t} \rho(\cdot) dv \right] = \int_{\mathcal{B}_t} \left[\dot{\rho}(\cdot) + \rho(\dot{\cdot}) + \rho(\cdot) \operatorname{div} \vec{v} \right] dv = \int_{\mathcal{B}_t} \rho(\dot{\cdot}) dv. \quad (3.14)$$

This result will be used for expressions of the form $\frac{d}{dt} [\int_{\mathcal{B}_t} \rho(\cdot) dv]$ in the following.

3.3.2 Linear and Angular Momentum Balance

The physical quantity under consideration in the linear momentum balance is the volume density of linear momentum $\mathcal{A} \triangleq \rho \vec{v}$. Supply and flux are given by volume forces $s^A \triangleq \vec{b}$ and the Cauchy stress vector $-\vec{f}^A \vec{n} \triangleq \vec{t}$. Furthermore, $p^A \triangleq 0$. Note the vector character of \mathcal{A} , s^A , and $-\vec{f}^A \vec{n}$. With this the global linear momentum balance reads

$$\frac{d}{dt} \left[\int_{\mathcal{B}_t} \rho \vec{v} dv \right] = \int_{\mathcal{B}_t} \vec{b} dv + \int_{\partial \mathcal{B}_t} \vec{t} da. \quad (3.15)$$

Using (3.14), Cauchy's theorem (3.6), and the divergence theorem leads to the local form of the linear momentum balance

$$\rho \dot{\vec{v}} = \operatorname{div} \boldsymbol{\sigma}^T + \vec{b}. \quad (3.16)$$

The angular momentum balance with $\mathcal{A} \triangleq \vec{x} \times \rho \vec{v}$, $p^A \triangleq 0$, $s^A \triangleq \vec{x} \times \vec{b}$, and $-\vec{f}^A \vec{n} \triangleq \vec{x} \times \vec{t}$

$$\frac{d}{dt} \left[\int_{\mathcal{B}_t} \vec{x} \times \rho \vec{v} dv \right] = \int_{\mathcal{B}_t} \vec{x} \times \vec{b} dv + \int_{\partial \mathcal{B}_t} \vec{x} \times \vec{t} da \quad (3.17)$$

yields (by applying (3.6), (3.14), and (3.16)) the aforementioned symmetry of the Cauchy stress tensor

$$\boldsymbol{\sigma}^T = \boldsymbol{\sigma}. \quad (3.18)$$

Here, the cross product is denoted by \times . With this the local form of the linear momentum balance (3.16) simplifies to

$$\rho \dot{\vec{v}} = \operatorname{div} \boldsymbol{\sigma} + \vec{b}. \quad (3.19)$$

For ease of readability, the linear momentum balance is referred to as (just) momentum balance in the following.

3.3.3 Energy Balance

The energy balance (or first law of thermodynamics) is obtained by $\mathcal{A} \triangleq \rho(\varepsilon + \frac{1}{2}|\vec{v}|^2)$, where ε is the internal-energy per mass and $\frac{1}{2}|\vec{v}|^2$ the kinetic energy per mass. The energy supply and flux are given by $s^{\mathcal{A}} \triangleq \vec{b} \cdot \vec{v} + q$, where q is a heat supply, and $-\vec{f}^{\mathcal{A}} \cdot \vec{n} \triangleq \vec{t} \cdot \vec{v} - \vec{q} \cdot \vec{n}$, where \vec{q} is a heat flux. There is no energy production $p^{\mathcal{A}} \triangleq 0$. With this it follows that

$$\frac{d}{dt} \left[\int_{\mathcal{B}_t} \rho \left(\varepsilon + \frac{1}{2}|\vec{v}|^2 \right) dv \right] = \int_{\mathcal{B}_t} [\vec{b} \cdot \vec{v} + q] dv + \int_{\partial \mathcal{B}_t} [\vec{t} \cdot \vec{v} - \vec{q} \cdot \vec{n}] da. \quad (3.20)$$

The complete set of mass, momentum, and energy balance (in combination with an appropriate constitutive equation) is often called Navier-Stokes equations [Zienkiewicz et al. 2009]. However, this naming is not unique as the term Navier-Stokes equations can also refer to the momentum balance, only [Böswirth et al. 2014].

3.3.4 Entropy Balance

The physical quantity under consideration in the entropy balance is $\mathcal{A} \triangleq \rho s$, where s is the entropy per mass. The entropy is a measure of disorder. A fundamental hypothesis states that the entropy supply s^s and entropy flux \vec{f}^s are connected to the heat supply q and heat flux \vec{q} by the absolute temperature T according to

$$s^{\mathcal{A}} \triangleq s^s = \frac{q}{T} \quad (3.21)$$

and

$$\vec{f}^{\mathcal{A}} \triangleq \vec{f}^s = \frac{\vec{q}}{T}. \quad (3.22)$$

None of the balance laws above shows a production term $p^{\mathcal{A}}$. In order to acknowledge the fact that the direction of certain processes (e.g. heat conduction) is not arbitrary (heat always flows from warmer to colder regions), the second law of thermodynamics states that the production of entropy p^s is always non-negative

$$p^{\mathcal{A}} \triangleq p^s \geq 0. \quad (3.23)$$

The global entropy balance can be written as

$$\frac{d}{dt} \left[\int_{\mathcal{B}_t} \rho s dv \right] = \int_{\mathcal{B}_t} \left[p^s + \frac{q}{T} \right] dv - \int_{\partial \mathcal{B}_t} \frac{\vec{q}}{T} \cdot \vec{n} da. \quad (3.24)$$

Applying (3.23) leads to the global entropy imbalance, which is commonly referred to as Clausius-Duhem inequality

$$\frac{d}{dt} \left[\int_{\mathcal{B}_t} \rho s \, dv \right] \geq \int_{\mathcal{B}_t} \frac{q}{T} \, dv - \int_{\partial \mathcal{B}_t} \frac{\vec{q}}{T} \cdot \vec{n} \, da. \quad (3.25)$$

Using (3.14) and the divergence theorem yields the local form of the entropy imbalance

$$\rho \dot{s} \geq -\operatorname{div} \frac{\vec{q}}{T} + \frac{q}{T}. \quad (3.26)$$

The next section reveals that the entropy imbalance does also give restrictions on thermodynamic consistent constitutive equations and thereby on the material response.

3.4 Model Derivation

As mentioned in section 3.1 the PF evolution equation (Allen-Cahn, or Cahn-Hilliard) can be coupled with the mass balance and the momentum balance in order to derive a PF model that can describe the dynamic evolution of fluids with two (or possibly more) phases. By taking this path, the order parameter of the PF model would have the character of a dimensionless phase variable that co-exists with density and velocity, see e.g. [Gomez and van der Zee 2017]. In contrast, the PF model of this work interprets the order parameter of the PF model as the mass density. It does not introduce a dimensionless phase variable, but incorporates the properties of the PF model by an appropriate constitutive equation. This type of model can be classified as a Navier-Stokes-Korteweg model. The general form of the capillary stress tensor, required in the constitutive equation of Navier-Stokes-Korteweg models, has been known since 1901 [Anderson et al. 1998]. However, the thermodynamic consistent derivation of the entire model within a rational framework yields deeper insights into the model. This section, which is based on [Diewald et al. 2020b], presents the derivation of the general Navier-Stokes-Korteweg model in a rational framework utilizing the Coleman-Noll procedure.

3.4.1 Mass, Momentum, Energy, and Entropy Balance

The derivation considers a domain \mathcal{B} which is fixed in space and has the boundary $\partial \mathcal{B}$. Part of the boundary of \mathcal{B} may be given by a solid surface $\partial \mathcal{B}_s$ and does therefore represent a solid-fluid interface as introduced in section 2.1. The material volume \mathcal{B}_t with the boundary $\partial \mathcal{B}_t$ is any subset of \mathcal{B} and consists of the same particles for all times t , cf. Figure 3.5.

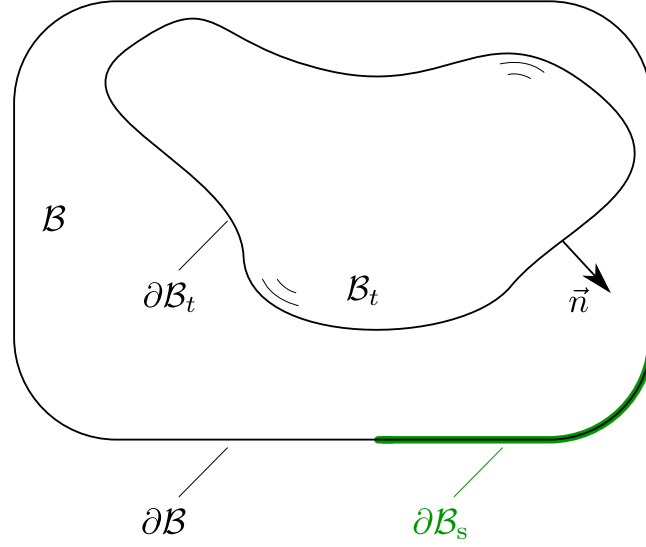


Figure 3.5: The domain \mathcal{B} is fixed in space and part of its boundary may be given by a solid surface $\partial\mathcal{B}_s$. The material volume \mathcal{B}_t is any subset of the domain \mathcal{B} .

The PF model of this work solves the mass balance

$$\dot{\rho} + \rho \operatorname{div} \vec{v} = 0 \quad (3.27)$$

and the momentum balance

$$\rho \dot{\vec{v}} = \operatorname{div} \boldsymbol{\sigma} + \vec{b}_0 - \rho g \vec{e}_g. \quad (3.28)$$

However, an appropriate and thermodynamic consistent constitutive relation between ρ , \vec{v} and $\boldsymbol{\sigma}$ has to be derived. Note that in the momentum balance (3.28) the volume forces \vec{b} are split into non-conservative volume forces \vec{b}_0 and gravitational volume forces $\rho g \vec{e}_g$, where g and \vec{e}_g are the gravitational acceleration and orientation

$$\vec{b} = \vec{b}_0 - \rho g \vec{e}_g. \quad (3.29)$$

With (3.29) the energy balance for \mathcal{B}_t reads

$$\begin{aligned} \frac{d}{dt} \left[\int_{\mathcal{B}_t} \rho \left(\varepsilon + \frac{1}{2} |\vec{v}|^2 + g x_g \right) dv + \int_{\partial\mathcal{B}_t \cap \partial\mathcal{B}_s} \rho \phi da \right] \\ = \int_{\mathcal{B}_t} \left[\vec{b}_0 \cdot \vec{v} + q \right] dv + \int_{\partial\mathcal{B}_t} \left[\boldsymbol{\sigma} \vec{n} \cdot \vec{v} - \vec{q} \cdot \vec{n} \right] da. \end{aligned} \quad (3.30)$$

This form of the energy balance is more intuitive than (3.20) as the potential energy is written on the left side with x_g denoting the (gravitational) height and $\nabla x_g = \vec{e}_g$.

In addition to the classical form of the energy balance (3.20), the energy balance used here includes a surface energy per mass ϕ . This allows to account for the energy contributions coming from the surface tensions of the solid-fluid interface as introduced in section 2.1. Due to (3.18) it holds that

$$\int_{\partial\mathcal{B}_t} \boldsymbol{\sigma} \vec{n} \cdot \vec{v} \, da = \int_{\mathcal{B}_t} \operatorname{div}(\boldsymbol{\sigma} \vec{v}) \, dv = \int_{\mathcal{B}_t} [\operatorname{div} \boldsymbol{\sigma} \cdot \vec{v} + \boldsymbol{\sigma} : \nabla^s \vec{v}] \, dv \quad (3.31)$$

with $\nabla^s(\cdot) = \frac{1}{2}(\nabla(\cdot) + (\nabla(\cdot))^T)$ and $:$ denoting a double contraction. Using (3.31), (3.28), (3.14), and the divergence theorem in (3.30) leads to

$$\int_{\mathcal{B}_t} \rho \dot{\varepsilon} \, dv + \frac{d}{dt} \left[\int_{\partial\mathcal{B}_t \cap \partial\mathcal{B}_s} \rho \phi \, da \right] = \int_{\mathcal{B}_t} [\boldsymbol{\sigma} : \nabla^s \vec{v} - \operatorname{div} \vec{q} + q] \, dv. \quad (3.32)$$

Inserting the local form of the entropy imbalance (3.26) and assuming that the temperature is constant ($T = \text{const.}$) within \mathcal{B}_t yields

$$\int_{\mathcal{B}_t} \rho (\dot{\varepsilon} - T \dot{s}) \, dv + \frac{d}{dt} \left[\int_{\partial\mathcal{B}_t \cap \partial\mathcal{B}_s} \rho \phi \, da \right] \leq \int_{\mathcal{B}_t} \boldsymbol{\sigma} : \nabla^s \vec{v} \, dv \quad (3.33)$$

with

$$\psi = \varepsilon - Ts \quad (3.34)$$

as the Helmholtz free energy per mass. Thus, the free energy dissipation inequality reads

$$\int_{\mathcal{B}_t} \rho \dot{\psi} \, dv + \frac{d}{dt} \left[\int_{\partial\mathcal{B}_t \cap \partial\mathcal{B}_s} \rho \phi \, da \right] \leq \int_{\mathcal{B}_t} \boldsymbol{\sigma} : \nabla^s \vec{v} \, dv. \quad (3.35)$$

3.4.2 Coleman-Noll Procedure

The Coleman-Noll procedure [Coleman and Noll 1963; Gurtin et al. 2010] is a method that allows to derive a thermodynamic consistent constitutive equation from the free energy dissipation inequality (3.35). For this, assumptions on the dependencies of ψ , ϕ , and $\boldsymbol{\sigma}$ have to be made. In the following, it is assumed that

$$\psi = \hat{\psi}(\rho, \nabla \rho), \quad (3.36)$$

$$\phi = \hat{\phi}(\rho), \quad (3.37)$$

$$\boldsymbol{\sigma} = \hat{\boldsymbol{\sigma}}(\nabla^s \vec{v}, \rho, \nabla \rho, \mu), \quad (3.38)$$

with

$$\mu = \frac{\partial(\rho \hat{\psi})}{\partial \rho} - \operatorname{div} \frac{\partial(\rho \hat{\psi})}{\partial \nabla \rho} \quad (3.39)$$

as the chemical potential. Above, the hat ($\hat{\cdot}$) denotes that an assumption for the dependencies was made. The dependencies of the Helmholtz free energy per mass $\psi = \hat{\psi}(\rho, \nabla\rho)$ are chosen in accordance with section 3.1. This means that the PF potential density, cf. (3.1), is identified with the Helmholtz free energy

$$f_1(\rho) + f_2(\nabla\rho) = \rho\hat{\psi}(\rho, \nabla\rho). \quad (3.40)$$

As a consequence, the order parameter of the PF model that is derived here is the density $\varphi = \rho$ and not a dimensionless phase variable. The surface energy per mass $\phi = \hat{\phi}(\rho)$ is assumed to depend on the density only. If the model was intended to include not only surface tensions but also line tensions (see section 2.2), the surface energy per mass would also have to depend on the gradient of the density. The exact forms of $\hat{\psi}(\rho, \nabla\rho)$ and $\hat{\phi}(\rho)$ used in this work are discussed in chapter 4. The assumptions for the dependencies of $\boldsymbol{\sigma}$ don't have to be made before the last step of the Coleman-Noll procedure, cf. (3.49). However, for reasons of uniformity they are already stated here. While these assumptions for $\boldsymbol{\sigma}$ might not be obvious at this point, they will prove to be pragmatic.

The free energy dissipation inequality (3.35) can now be rewritten as

$$\begin{aligned} & \int_{\mathcal{B}_t} \rho \left[\frac{\partial\hat{\psi}}{\partial\rho} \dot{\rho} + \frac{\partial\hat{\psi}}{\partial\nabla\rho} \cdot \nabla\dot{\rho} - \frac{\partial\hat{\psi}}{\partial\nabla\rho} \cdot (\nabla\vec{v})^T \nabla\rho \right] dv \\ & + \frac{d}{dt} \left[\int_{\partial\mathcal{B}_t \cap \partial\mathcal{B}_s} \rho\hat{\phi} da \right] \leq \int_{\mathcal{B}_t} \hat{\boldsymbol{\sigma}} : \nabla^s \vec{v} dv \end{aligned} \quad (3.41)$$

for which the identity

$$\begin{aligned} \frac{d(\nabla\rho)}{dt} &= \frac{\partial(\nabla\rho)}{\partial t} + [\nabla(\nabla\rho)] \vec{v} \\ &= \nabla \left(\frac{\partial\rho}{\partial t} + \nabla\rho \cdot \vec{v} \right) - (\nabla\vec{v})^T \nabla\rho \\ &= \nabla\dot{\rho} - (\nabla\vec{v})^T \nabla\rho \end{aligned} \quad (3.42)$$

[Shokrpour Roudbari et al. 2018] has been used. Integrating by parts as well as using

$$\frac{\partial\hat{\psi}}{\partial\nabla\rho} \cdot (\nabla\vec{v})^T \nabla\rho = \left(\frac{\partial\hat{\psi}}{\partial\nabla\rho} \otimes \nabla\rho \right) : (\nabla\vec{v})^T, \quad (3.43)$$

where \otimes is the dyadic product, yields

$$\begin{aligned} & \int_{\mathcal{B}_t} \left[\left(\rho \frac{\partial \hat{\psi}}{\partial \rho} - \operatorname{div} \frac{\partial(\rho \hat{\psi})}{\partial \nabla \rho} \right) \dot{\rho} - \rho \left(\frac{\partial \hat{\psi}}{\partial \nabla \rho} \otimes \nabla \rho \right) : (\nabla \vec{v})^T \right] dv \\ & + \int_{\partial \mathcal{B}_t} \dot{\rho} \frac{\partial(\rho \hat{\psi})}{\partial \nabla \rho} \cdot \vec{n} da + \frac{d}{dt} \left[\int_{\partial \mathcal{B}_t \cap \partial \mathcal{B}_s} \rho \hat{\phi} da \right] \leq \int_{\mathcal{B}_t} \hat{\sigma} : \nabla^s \vec{v} dv. \end{aligned} \quad (3.44)$$

Inserting the mass balance (3.13), assuming that $\frac{\partial \hat{\psi}}{\partial \nabla \rho} \otimes \nabla \rho = \left(\frac{\partial \hat{\psi}}{\partial \nabla \rho} \otimes \nabla \rho \right)^T$, and using the identity

$$\rho \frac{\partial \hat{\psi}}{\partial \rho} - \operatorname{div} \frac{\partial(\rho \hat{\psi})}{\partial \nabla \rho} = \mu - \hat{\psi}, \quad (3.45)$$

which uses (3.39), leads to

$$\begin{aligned} & \int_{\mathcal{B}_t} \left[-\rho (\mu - \hat{\psi}) \mathbf{1} - \rho \left(\frac{\partial \hat{\psi}}{\partial \nabla \rho} \otimes \nabla \rho \right) \right] : \nabla^s \vec{v} dv \\ & + \int_{\partial \mathcal{B}_t} \dot{\rho} \frac{\partial(\rho \hat{\psi})}{\partial \nabla \rho} \cdot \vec{n} da + \frac{d}{dt} \left[\int_{\partial \mathcal{B}_t \cap \partial \mathcal{B}_s} \rho \hat{\phi} da \right] \leq \int_{\mathcal{B}_t} \hat{\sigma} : \nabla^s \vec{v} dv, \end{aligned} \quad (3.46)$$

where $\mathbf{1}$ is the identity matrix.

The material time derivative of the surface energy can be written as

$$\frac{d}{dt} \left[\int_{\partial \mathcal{B}_t \cap \partial \mathcal{B}_s} \rho \hat{\phi} da \right] = \int_{\partial \mathcal{B}_t \cap \partial \mathcal{B}_s} \left[\frac{d(\rho \hat{\phi})}{dt} + \rho \hat{\phi} (\operatorname{div}_s \vec{v}_{\partial \mathcal{B}_s}^{\tan} - K \vec{v}_{\partial \mathcal{B}_s}^\perp) \right] da \quad (3.47)$$

[Fried and Gurtin 2007]. Here, div_s and K are the surface divergence and total (twice the mean) curvature. The tangential and normal velocity on $\partial \mathcal{B}_s$ are $\vec{v}_{\partial \mathcal{B}_s}^{\tan}$ and $\vec{v}_{\partial \mathcal{B}_s}^\perp$. Applying (3.47) and splitting the integral over $\partial \mathcal{B}_t$ in (3.46) into the part $\partial \mathcal{B}_t \cap \partial \mathcal{B}_s$ and the part $\partial \mathcal{B}_t \setminus \partial \mathcal{B}_s$ gives

$$\begin{aligned} & \int_{\mathcal{B}_t} \left[-\rho (\mu - \hat{\psi}) \mathbf{1} - \rho \left(\frac{\partial \hat{\psi}}{\partial \nabla \rho} \otimes \nabla \rho \right) \right] : \nabla^s \vec{v} dv \\ & + \int_{\partial \mathcal{B}_t \cap \partial \mathcal{B}_s} \left[\dot{\rho} \frac{\partial(\rho \hat{\psi})}{\partial \nabla \rho} \cdot \vec{n} + \frac{d(\rho \hat{\phi})}{dt} + \rho \hat{\phi} (\operatorname{div}_s \vec{v}_{\partial \mathcal{B}_s}^{\tan} - K \vec{v}_{\partial \mathcal{B}_s}^\perp) \right] da \\ & + \int_{\partial \mathcal{B}_t \setminus \partial \mathcal{B}_s} \dot{\rho} \frac{\partial(\rho \hat{\psi})}{\partial \nabla \rho} \cdot \vec{n} da \leq \int_{\mathcal{B}_t} \hat{\sigma} : \nabla^s \vec{v} dv. \end{aligned} \quad (3.48)$$

The constitutive equation for $\hat{\boldsymbol{\sigma}}$ has to fulfill the constraint that is given by (3.48) in order to be thermodynamically consistent. A suitable choice for $\hat{\boldsymbol{\sigma}}$ is given by

$$\hat{\boldsymbol{\sigma}} = \boldsymbol{\sigma}^v + \boldsymbol{\sigma}^\psi, \quad (3.49)$$

with

$$\boldsymbol{\sigma}^v = 2\eta^v(\rho) \left[\nabla^s \vec{v} - \frac{1}{3} \text{tr}(\nabla^s \vec{v}) \mathbf{1} \right] \quad (3.50)$$

[Zienkiewicz et al. 2009] as the viscous stress tensor, viscosity $\eta^v(\rho)$, trace tr , and

$$\boldsymbol{\sigma}^\psi = -\rho \left(\mu - \hat{\psi} \right) \mathbf{1} - \rho \left(\frac{\partial \hat{\psi}}{\partial \nabla \rho} \otimes \nabla \rho \right) \quad (3.51)$$

as the so-called Korteweg stress tensor. A more vivid view on the Korteweg stress tensor is presented later on in section 4.2. The exact form of $\eta^v(\rho)$ used in this work is discussed in section 4.3. Finally, choosing the boundary conditions such that (3.48) is not violated leads to the general Navier-Stokes-Korteweg model. It solves

$$\dot{\rho} + \rho \text{div} \vec{v} = 0 \quad \text{in } \mathcal{B}, \quad (3.52)$$

$$\rho \dot{\vec{v}} = \text{div}(\boldsymbol{\sigma}^v + \boldsymbol{\sigma}^\psi) + \vec{b}_0 - \rho g \vec{e}_g \quad \text{in } \mathcal{B}, \quad (3.53)$$

with

$$\boldsymbol{\sigma}^v = 2\eta^v(\rho) \left[\nabla^s \vec{v} - \frac{1}{3} \text{tr}(\nabla^s \vec{v}) \mathbf{1} \right], \quad (3.54)$$

$$\boldsymbol{\sigma}^\psi = -\rho \left(\mu - \hat{\psi}(\rho, \nabla \rho) \right) \mathbf{1} - \rho \left(\frac{\partial \hat{\psi}(\rho, \nabla \rho)}{\partial \nabla \rho} \otimes \nabla \rho \right), \quad \text{and} \quad (3.55)$$

$$\mu = \frac{\partial(\rho \hat{\psi}(\rho, \nabla \rho))}{\partial \rho} - \text{div} \frac{\partial(\rho \hat{\psi}(\rho, \nabla \rho))}{\partial \nabla \rho}, \quad (3.56)$$

under the boundary conditions

$$\vec{v} = \vec{0} \quad \text{on } \partial \mathcal{B} \cap \partial \mathcal{B}_s, \quad (3.57)$$

$$\frac{\partial(\rho \hat{\psi}(\rho, \nabla \rho))}{\partial \nabla \rho} \cdot \vec{n} + \frac{\partial(\rho \hat{\phi}(\rho))}{\partial \rho} = 0 \quad \text{on } \partial \mathcal{B} \cap \partial \mathcal{B}_s, \quad \text{and} \quad (3.58)$$

$$\frac{\partial(\rho \hat{\psi}(\rho, \nabla \rho))}{\partial \nabla \rho} \cdot \vec{n} = 0 \quad \text{on } \partial \mathcal{B} \setminus \partial \mathcal{B}_s. \quad (3.59)$$

It is beneficial to look at the following identity

$$\begin{aligned}
\operatorname{div} \boldsymbol{\sigma}^\psi &= \nabla \left(\rho \hat{\psi} - \mu \rho \right) - \operatorname{div} \left[\rho \left(\frac{\partial \hat{\psi}}{\partial \nabla \rho} \otimes \nabla \rho \right) \right] \\
&= \frac{\partial(\rho \hat{\psi})}{\partial \rho} \nabla \rho + (\nabla(\nabla \rho))^T \frac{\partial \rho \hat{\psi}}{\partial \nabla \rho} - \left(\frac{\partial(\rho \hat{\psi})}{\partial \rho} - \operatorname{div} \frac{\partial(\rho \hat{\psi})}{\partial \nabla \rho} \right) \nabla \rho - \nabla \mu \rho \\
&\quad - \operatorname{div} \left[\rho \left(\frac{\partial \hat{\psi}}{\partial \nabla \rho} \otimes \nabla \rho \right) \right] \\
&= -\nabla \mu \rho
\end{aligned} \tag{3.60}$$

[Dunn and Serrin 1985] for which (3.39) was used. It is evident that the gradient of the chemical potential μ acts as a driving force. If gravitation is neglected, an equilibrium state can only be given if the chemical potential μ is constant within \mathcal{B} . More details are presented in section 3.5.

3.4.3 Global Energy Dissipation Relation

The Navier-Stokes-Korteweg model derived above dissipates energy. If non-conservative volume forces are neglected ($\vec{b}_0 = \vec{0}$), the global energy E is

$$E[\vec{v}, \rho, \nabla \rho] = \int_{\mathcal{B}} \left[\rho \hat{\psi}(\rho, \nabla \rho) + \frac{1}{2} \rho |\vec{v}|^2 + \rho g x_g \right] dV + \int_{\partial \mathcal{B} \cap \partial \mathcal{B}_s} \rho \hat{\phi}(\rho) dA. \tag{3.61}$$

The energy change in time is negative

$$\begin{aligned}
\dot{E} &= \int_{\mathcal{B}} \left[\frac{\partial(\rho \hat{\psi})}{\partial t} + \frac{1}{2} \frac{\partial(\rho |\vec{v}|^2)}{\partial t} + g x_g \frac{\partial \rho}{\partial t} \right] dV + \int_{\partial \mathcal{B} \cap \partial \mathcal{B}_s} \frac{\partial(\rho \hat{\phi})}{\partial t} dA \\
&= \int_{\mathcal{B}} -2\eta^v(\rho) \left| \nabla^s \vec{v} - \frac{1}{3} \operatorname{tr}(\nabla^s \vec{v}) \mathbf{1} \right|^2 dV
\end{aligned} \tag{3.62}$$

if the velocity is set to $\vec{v} = \vec{0}$ on all of $\partial \mathcal{B}$. The magnitude of dissipation is determined by the viscosity η^v only which reflects the physical behavior. The constitutive equation derived above does not add or dissipate any artificial energy. More details on how (3.62) was derived are presented in appendix A.

3.5 Static Case

In many cases only the static equilibrium configuration of a wetting scenario is of interest. Using the full Navier-Stokes-Korteweg model for these cases would lead

to much higher computational costs than necessary. It is therefore favorable to formulate a model that does not describe the full dynamic evolution but computes the static equilibrium configuration in an efficient manner. This section derives the static Allen-Cahn model directly from the dynamic Navier-Stokes-Korteweg model, cf. Figure 3.2. Thereafter, it is shown that the static model can also be obtained by a variational formulation from the PF potential.

3.5.1 Derivation from the General Model

Regarding the static case ($\vec{v} = \vec{0}$) the Navier-Stokes-Korteweg model, as it is stated in the box on page 26, reduces to

$$\frac{\partial \rho}{\partial t} = 0, \quad (3.63)$$

$$\vec{0} = \operatorname{div} \boldsymbol{\sigma}^\psi - \rho g \vec{e}_g. \quad (3.64)$$

Non-conservative volume forces are neglected ($\vec{b}_0 = \vec{0}$). Using (3.60) and $\nabla x_g = \vec{e}_g$ in (3.64) yields

$$\begin{aligned} \vec{0} &= -\nabla \mu \rho - \rho g \nabla x_g \\ &= -\rho \nabla (\mu + g x_g). \end{aligned} \quad (3.65)$$

As the density is in general not zero ($\rho \neq 0$), it follows that

$$\mu + g x_g = \text{const.} = -\lambda, \quad (3.66)$$

or

$$\mu + g x_g + \lambda = 0, \quad (3.67)$$

where λ is a constant. If the influence of gravity is neglected, the static solution is characterized by a constant value of the chemical potential μ . Solving (3.67) directly is numerically not feasible when there is a large distance between the initial state and the static equilibrium. Therefore, an evolution equation is used to gradually relax the initial state towards the static equilibrium (3.67). As discussed in section 3.1 this can be done by using an Allen-Cahn, cf. (3.3), or Cahn-Hilliard, cf. (3.4), evolution equation.

Cahn-Hilliard type approaches lead to a stiff numerical behavior which is due to the fourth order spatial derivatives. Therefore, bilinear finite elements cannot be applied [Anders and Weinberg 2011b] and techniques like mixed finite element methods, coupled equations, interpolation functions that have a high degree of continuity, or a discontinuous Galerkin method are required [Wells et al. 2006].

See also [Rajagopal et al. 2010; Anders and Weinberg 2011a]. Allen-Cahn type approaches do not have the same drawbacks and allow for a simpler and resource efficient implementation, see e.g. [Yang et al. 2006]. While the kinetic path towards the static equilibrium is in general different when using a Cahn-Hilliard or Allen-Cahn evolution equation, they will yield the same stationary solution [Ben Said et al. 2014]. Since this section deals with the derivation of a simple model that computes the static equilibrium configuration only, an Allen-Cahn evolution equation is chosen. [Diewald et al. 2018b]

Applying the evolution equation to (3.67) and using (3.39) leads to the static Allen-Cahn model which solves

$$\frac{\partial(\rho\hat{\psi}(\rho, \nabla\rho))}{\partial\rho} - \operatorname{div}\frac{\partial(\rho\hat{\psi}(\rho, \nabla\rho))}{\partial\nabla\rho} + gx_g + \lambda = -\frac{1}{M}\frac{\partial\rho}{\partial t} \quad \text{in } \mathcal{B} \quad , \quad (3.68)$$

$$\int_{\mathcal{B}} \rho \, dV = m_{\mathcal{B}} \quad \text{in } \mathcal{B} \quad , \quad (3.69)$$

under the boundary conditions

$$\frac{\partial(\rho\hat{\psi}(\rho, \nabla\rho))}{\partial\nabla\rho} \cdot \vec{n} + \frac{\partial(\rho\hat{\phi}(\rho))}{\partial\rho} = 0 \quad \text{on } \partial\mathcal{B} \cap \partial\mathcal{B}_s \quad , \text{ and} \quad (3.70)$$

$$\frac{\partial(\rho\hat{\psi}(\rho, \nabla\rho))}{\partial\nabla\rho} \cdot \vec{n} = 0 \quad \text{on } \partial\mathcal{B} \setminus \partial\mathcal{B}_s \quad . \quad (3.71)$$

Note that in order to allow the evolution towards the static equilibrium, (3.63) is only fulfilled globally with $m_{\mathcal{B}}$ as the total mass in \mathcal{B} , cf. (3.69). The boundary conditions of the static equilibrium are the same as for the dynamic case (3.57), (3.58), and (3.59). In this static Allen-Cahn model, the time t should not be understood as the physical time. Instead it is an artificial time that is introduced by the evolution equation.

Once the current state is close to the static equilibrium and therefore

$$\int_{\mathcal{B}} \frac{1}{2} \left(\frac{\dot{\rho}}{M} \right)^2 \, dV \leq e_{\text{tol}} \quad , \quad (3.72)$$

with e_{tol} being a (small) tolerance value, the evolution equation is no longer used and the quasi-static limit condition

$$\frac{\partial(\rho\hat{\psi})}{\partial\rho} - \operatorname{div}\frac{\partial(\rho\hat{\psi})}{\partial\nabla\rho} + gx_g + \lambda = 0 \quad (3.73)$$

is solved instead of (3.68).

3.5.2 Equivalence to the Variational Formulation

The static Allen-Cahn model as it is stated in the box on page 29 is equivalent to the following variational derivation. The total PF potential of the domain \mathcal{B} is given by

$$F[\rho, \nabla\rho, \lambda] = \int_{\mathcal{B}} [\rho\hat{\psi}(\rho, \nabla\rho) + \rho gx_g] dV + \lambda \left(\int_{\mathcal{B}} \rho dV - m_{\mathcal{B}} \right) + \int_{\partial\mathcal{B} \cap \partial\mathcal{B}_s} \rho\phi(\rho) dA. \quad (3.74)$$

In this λ can now be seen as a Lagrange multiplier ensuring the conservation of mass within \mathcal{B} . Using the Allen-Cahn evolution equation (3.3) for the density ρ and invoking integration by parts yields

$$\int_{\mathcal{B}} \left[\frac{\partial(\rho\hat{\psi})}{\partial\rho} - \operatorname{div} \frac{\partial(\rho\hat{\psi})}{\partial\nabla\rho} + gx_g + \lambda + \frac{1}{M} \frac{\partial\rho}{\partial t} \right] \delta\rho dV + \int_{\partial\mathcal{B}} \frac{\partial(\rho\hat{\psi})}{\partial\nabla\rho} \cdot \vec{n} \delta\rho dA + \int_{\partial\mathcal{B} \cap \partial\mathcal{B}_s} \frac{\partial(\rho\hat{\phi})}{\partial\rho} \delta\rho dA = 0. \quad (3.75)$$

In addition, the first variation of F with respect to λ is required to be zero

$$\left(\int_{\mathcal{B}} \rho dV - m_{\mathcal{B}} \right) \delta\lambda = 0. \quad (3.76)$$

The surface integral over $\partial\mathcal{B}$ in (3.75) can be split into

$$\int_{\partial\mathcal{B}} \frac{\partial(\rho\hat{\psi})}{\partial\nabla\rho} \cdot \vec{n} \delta\rho dA = \int_{\partial\mathcal{B} \setminus \partial\mathcal{B}_s} \frac{\partial(\rho\hat{\psi})}{\partial\nabla\rho} \cdot \vec{n} \delta\rho dA + \int_{\partial\mathcal{B} \cap \partial\mathcal{B}_s} \frac{\partial(\rho\hat{\psi})}{\partial\nabla\rho} \cdot \vec{n} \delta\rho dA. \quad (3.77)$$

By applying this split it follows from (3.75) and (3.76) that

$$\frac{\partial(\rho\hat{\psi})}{\partial\rho} - \operatorname{div} \frac{\partial(\rho\hat{\psi})}{\partial\nabla\rho} + gx_g + \lambda + \frac{1}{M} \frac{\partial\rho}{\partial t} = 0 \quad \text{in} \quad \mathcal{B}, \quad (3.78)$$

$$\int_{\mathcal{B}} \rho dV - m_{\mathcal{B}} = 0 \quad \text{in} \quad \mathcal{B}, \quad (3.79)$$

with

$$\frac{\partial(\rho\hat{\psi})}{\partial\nabla\rho} \cdot \vec{n} + \frac{\partial(\rho\hat{\phi})}{\partial\rho} = 0 \quad \text{on} \quad \partial\mathcal{B} \cap \partial\mathcal{B}_s, \quad \text{and} \quad (3.80)$$

$$\frac{\partial(\rho\hat{\psi})}{\partial\nabla\rho} \cdot \vec{n} = 0 \quad \text{on} \quad \partial\mathcal{B} \setminus \partial\mathcal{B}_s, \quad (3.81)$$

which is equivalent to the static Allen-Cahn model in the box on page 29.

The variational derivation starting from the total PF potential of the domain under consideration as it is presented here is more common for the derivation of PF models than the derivation by a simplification of the full dynamic model as it is presented in the previous section. Nonetheless, the derivation by a simplification of the full dynamic model reveals the direct relation between the dynamic and the static model.

4 Choices for the Helmholtz Free Energy and Viscosity

In chapter 3 it is stated that the Helmholtz free energy per mass $\hat{\psi}(\rho, \nabla\rho)$ is a function that depends on ρ and $\nabla\rho$. However, no explicit choice for the Helmholtz free energy is made. The same holds true for the surface energy per mass $\hat{\phi}(\rho)$, which is a function of ρ . The general model of chapter 3 has to be made specific by defining the Helmholtz free energy and surface energy in accordance with the fluid under consideration.

This chapter presents two different choices for the Helmholtz free energy. Firstly, an empirical Helmholtz free energy is presented which is motivated phenomenologically. Thereafter, a Helmholtz free energy that is based on a thermodynamic equation of state (EoS) for the Lennard-Jones truncated and shifted (LJTS) fluid is introduced. The according surface energies are formulated as well.

In addition, the viscosity η^v needs to be defined in accordance with the fluid under consideration. This is done at the end of this chapter.

4.1 Empirical Helmholtz Free Energy

An empirical Helmholtz free energy formulation for wetting scenarios has to show the following characteristics:

- There are (at least) two stable phases, namely the vapor and the liquid phase.
- The interface between the two phases has an energy that is defined by the surface tension between the two phases.
- The interface between the two phases has a defined width.

The empirical Helmholtz free energy per mass ψ^e used in this work is chosen such

that

$$\rho \hat{\psi}(\rho, \nabla \rho) = \rho \psi^e(\rho, \nabla \rho) = \alpha^e \rho a^e(\rho) + \frac{1}{2} \frac{\beta^e}{(\rho' - \rho'')^2} |\nabla \rho|^2. \quad (4.1)$$

In this, $\rho a^e(\rho)$ is a double-well function as depicted in Figure 4.1 (left). The two minima of the double-well function lead to two stable bulk phases. In this empirical approach the bulk density of the vapor phase ρ'' and the bulk density of the liquid phase ρ' are not fixed but can be set to the desired value depending on the fluid under consideration. Therefore, the density is normalized by

$$\varphi(\rho) = \frac{\rho - \rho''}{\rho' - \rho''} \quad (4.2)$$

so that bulk phases are characterized by $\varphi(\rho'') = \varphi'' = 0$ in the gas phase and $\varphi(\rho') = \varphi' = 1$ in the liquid phase,

$$\rho a^e(\varphi(\rho)) = \varphi^2 (1 - \varphi)^2. \quad (4.3)$$

With this, the free energy of the bulk phases is zero and φ can be seen as a dimensionless order parameter distinguishing between the two phases.

While the double-well function ensures the existence of two stable phases, the parameters α^e and β^e can be used to satisfy the two other requirements regarding the energy and width of the interface between the stable phases. The underlying idea was shown in [Cahn and Hilliard 1958].

A planar interface that is perpendicular to an axis x and is located at $x = 0$ is regarded. Gravitational effects are neglected ($g = 0$). The excess free energy Ω^e , which is the energy that is stored in that interface, can be computed by

$$\Omega^e = A \int_{-\infty}^{\infty} \rho \psi^e dx. \quad (4.4)$$

In this, A is the surface area of the interface (perpendicular to x). In order to fulfill the requirement regarding the energy of the interface, Ω^e has to be equal to the surface tension between the liquid and the vapor phase γ_{lv} multiplied with A ,

$$\Omega^e = A \gamma_{lv}. \quad (4.5)$$

The final requirement regarding the width of the interface can be expressed as

$$\left. \frac{d\varphi}{dx} \right|_{x=0} = \frac{1}{l^e}, \quad (4.6)$$

where l^e is referred to as the interface width, cf. Figure 4.1 (right).

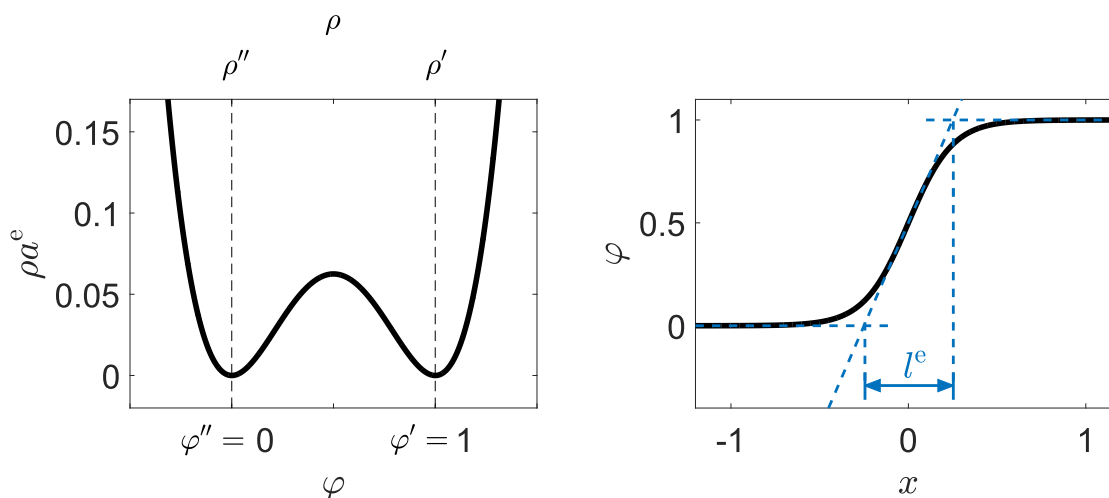


Figure 4.1: Left: The double-well function ρa^e yields two stable bulk phases at ρ'' and ρ' . Since the values of ρ'' and ρ' depend on the fluid under consideration, the density is normalized such that the bulk phases are given by $\varphi'' = 0$ and $\varphi' = 1$. Right: Plot of φ along an axis x that is perpendicular to a vapor-liquid interface. The interface width is l^e .

For the regarded planar interface, the solution state as described by (3.68) reduces to

$$\frac{\partial(\rho\hat{\psi}(\rho, \nabla\rho))}{\partial\rho} - \frac{d}{dx} \left(\frac{\partial(\rho\hat{\psi}(\rho, \nabla\rho))}{\partial\nabla\rho} \right) + \lambda = 0, \quad (4.7)$$

with $\nabla\rho = [\frac{d\rho}{dx} \ 0 \ 0]^T$. Multiplying with $\frac{d\rho}{dx}$ yields

$$\frac{\partial(\rho\hat{\psi}(\rho, \nabla\rho))}{\partial\rho} \frac{d\rho}{dx} - \frac{d}{dx} \left(\frac{\partial(\rho\hat{\psi}(\rho, \nabla\rho))}{\partial\nabla\rho} \right) \frac{d\rho}{dx} + \lambda \frac{d\rho}{dx} = 0, \quad (4.8)$$

which can be rewritten as

$$\frac{d}{dx} \left[\rho\hat{\psi}(\rho, \nabla\rho) - \frac{\partial(\rho\hat{\psi}(\rho, \nabla\rho))}{\partial\nabla\rho} \frac{d\rho}{dx} + \lambda\rho \right] = 0. \quad (4.9)$$

For this the identity

$$\frac{\partial(\rho\hat{\psi}(\rho, \nabla\rho))}{\partial\nabla\rho} \frac{d^2\rho}{dx^2} - \frac{d}{dx} \left(\frac{\partial(\rho\hat{\psi}(\rho, \nabla\rho))}{\partial\nabla\rho} \frac{d\rho}{dx} \right) = - \frac{d}{dx} \left(\frac{\partial(\rho\hat{\psi}(\rho, \nabla\rho))}{\partial\nabla\rho} \right) \frac{d\rho}{dx} \quad (4.10)$$

was used. From (4.9) it follows that

$$\rho\hat{\psi}(\rho, \nabla\rho) - \frac{\partial(\rho\hat{\psi}(\rho, \nabla\rho))}{\partial\nabla\rho} \frac{d\rho}{dx} + \lambda\rho = \text{const.} = c, \quad (4.11)$$

with c being a constant. This is an essential result for the planar interface without gravity. It is also used in sections 4.2 and 7.1.

Writing (4.11) for the empirical Helmholtz free energy of this section (4.1) at the position of one of the bulk phases (e.g. the vapor bulk phase) gives

$$\alpha^e \rho'' a^e(\varphi'') + \lambda \rho'' = c \quad (4.12)$$

since $\frac{d\rho}{dx} = 0$ in the bulk phases. For the double-well function it holds that

$$\rho'' a^e(\varphi'') = 0 \quad \text{and} \quad \left. \frac{d(\rho a^e)}{d\varphi} \right|_{\varphi=\varphi''} = 0, \quad (4.13)$$

cf. Figure 4.1 (right). Therefore, it follows from (3.66) and (3.39) that

$$\lambda = -\mu = 0 \quad \text{and thus} \quad c = 0. \quad (4.14)$$

With this, (4.11) can be written for the empirical Helmholtz free energy (4.1) at any position as

$$\alpha^e \rho a^e(\varphi) = \frac{1}{2} \beta^e \left(\frac{d\varphi}{dx} \right)^2. \quad (4.15)$$

Using this result in the requirement regarding the energy of the interface that is stated in (4.5) leads to

$$\int_{-\infty}^{\infty} \left[\alpha^e \rho a^e(\varphi) + \frac{1}{2} \beta^e \left(\frac{d\varphi}{dx} \right)^2 \right] dx = \int_{-\infty}^{\infty} 2\alpha^e \rho a^e(\varphi) dx = \gamma_{lv}. \quad (4.16)$$

With

$$dx = \sqrt{\frac{\beta^e}{2\alpha^e \rho a^e(\varphi)}} d\varphi, \quad (4.17)$$

cf. (4.15), the integral over x can be rewritten as an integral over φ

$$\int_{-\infty}^{\infty} 2\alpha^e \rho a^e(\varphi) dx = \int_0^1 \sqrt{2\alpha^e \beta^e \rho a^e(\varphi)} d\varphi = \gamma_{lv}. \quad (4.18)$$

Evaluating the integral yields

$$\frac{\sqrt{2\alpha^e \beta^e}}{6} = \gamma_{lv}. \quad (4.19)$$

Using (4.17) in the requirement regarding the width of the interface that is stated in (4.6) leads to

$$\left. \frac{d\varphi}{dx} \right|_{x=0} = \sqrt{\frac{2\alpha^e \rho a^e(\varphi = \frac{1}{2})}{\beta^e}} = \sqrt{\frac{\alpha^e}{8\beta^e}} = \frac{1}{l^e}. \quad (4.20)$$

Now, α^e and β^e can be determined by solving (4.19) and (4.20),

$$\alpha^e = 12 \frac{\gamma_{lv}}{l^e} \quad \text{and} \quad \beta^e = \frac{3}{2} \gamma_{lv} l^e. \quad (4.21)$$

The empirical Helmholtz free energy density reads

$$\rho \psi^e(\varphi, \nabla \varphi) = 12 \frac{\gamma_{lv}}{l^e} \varphi^2 (1 - \varphi)^2 + \frac{3}{4} \gamma_{lv} l^e |\nabla \varphi|^2. \quad (4.22)$$

Surface Energy

The surface energy ϕ^e is chosen such that it represents the surface tension between the solid surface and the liquid γ_{sl} if the liquid is in contact with the solid surface as well as the surface tension between the solid surface and the vapor γ_{sv} if the vapor is in contact with the solid surface,

$$\rho \hat{\phi}(\varphi) = \rho \phi^e(\varphi) = \gamma_{sl} h(\varphi) + \gamma_{sv} (1 - h(\varphi)), \quad (4.23)$$

cf. [Ben Said et al. 2014]. In this, $h(\varphi)$ interpolates between the solid-liquid and solid-vapor interface

$$h(\varphi) = \varphi^3 (6\varphi^2 - 15\varphi + 10), \quad (4.24)$$

with

$$h(\varphi = 0) = 0 \quad \text{and} \quad h(\varphi = 1) = 1. \quad (4.25)$$

This form of the interpolation function $h(\varphi)$ is chosen since its properties, e.g.

$$\left. \frac{dh(\varphi)}{d\varphi} \right|_{\varphi=\varphi'} = \left. \frac{dh(\varphi)}{d\varphi} \right|_{\varphi=\varphi''} = \left. \frac{d^2h(\varphi)}{d\varphi^2} \right|_{\varphi=\varphi'} = \left. \frac{d^2h(\varphi)}{d\varphi^2} \right|_{\varphi=\varphi''} = 0, \quad (4.26)$$

are numerically advantageous. A plot of $h(\varphi)$ can be seen in Figure 4.2.

Special attention should be given to the fact that the presented model does not explicitly define a contact angle, cf. section 2.2, in the form of a Neumann boundary condition. Instead, the energy contribution from the solid-liquid and solid-fluid surface tensions are directly included in the model. This approach is much closer to the underlying physics than directly prescribing the contact angle which is in fact a result of the energy contributions. For more information on the connection between the energetic approach and the geometric prescription of a contact angle the reader is referred to [Xu and Wang 2010].

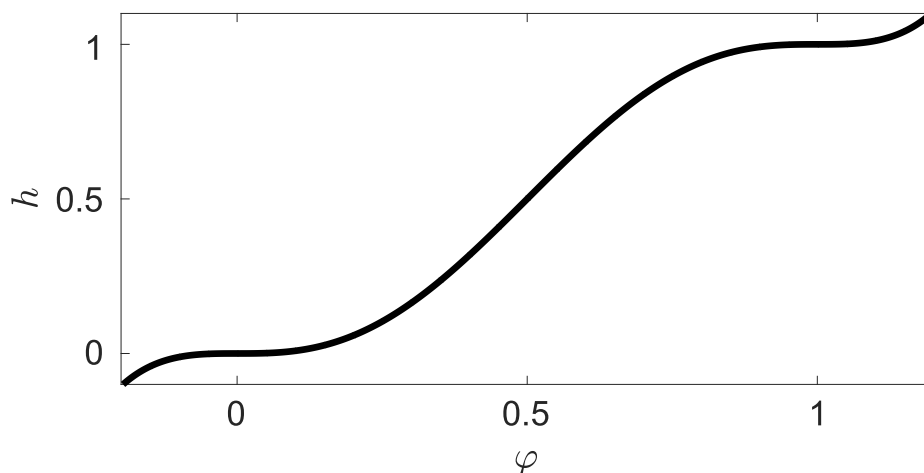


Figure 4.2: Plot of the interpolation function $h(\varphi)$. It is chosen because of its numerically advantageous properties.

4.2 Equation of State Based Helmholtz Free Energy

The interfacial properties of a liquid are determined on an atomistic scale. The formulation of the Helmholtz free energy for a PF model has to reproduce them. However, it is difficult to determine these properties experimentally. It is therefore favorable to link the formulation of the Helmholtz free energy for a PF model to atomistic molecular dynamics (MD) simulations with which the interfacial properties of a fluid can be determined. This section demonstrates how a thermodynamic equation of state (EoS) that originates from atomistic simulations for the Lennard-Jones truncated shifted (LJTS) fluid can be incorporated into a PF model. This approach is also presented in [Diewald et al. 2018a], which is the basis for this section.

The general concept of linking a PF model to the atomistic scale by feeding it with data from atomistic simulations has been applied in various fields of research. In [Bragard et al. 2002] a PF model for solidification inherits its interfacial properties of the solid-liquid interface from MD simulations. Also investigating solidification with a PF model the authors of [Danilov et al. 2009] extract the input parameters for their model from MD simulations. They also sensitize the fact that special attention has to be given to the differences between the MD and PF simulations regarding the underlying assumptions and approximations. The PF simulations in [Wu and Karma 2007] gain their PF parameters from MD simulations. MD simulations cannot only be used to determine input parameters for PF

simulations but can also help to find meaningful initialization states for the order parameter of the PF, see e.g. [Nestler et al. 2009]. For this, it is necessary to map the discrete data of the atomistic simulations to the continuous order parameter. Such a mapping is presented in [Bishop and Craig Carter 2002]. For PF simulations of ferroelectric materials the free energy of the PF model is fitted to atomistic simulations in [Völker et al. 2011, 2012]. In [Vaithyanathan et al. 2002, 2004] a multiscale approach for PF simulations of precipitation in an aluminum alloy is presented. For this approach, the energy contributions of the bulk, interface, and strain are provided from atomistic simulations.

The above-mentioned models obtain their information on the physics from atomistic simulations but they incorporate this information into the PF models by fits. However, if an EoS that adequately represents the behavior of the considered substance exists, it is advantageous to directly incorporate this EoS into the PF model. Many models for fluids use the van der Waals EoS, see e.g. [Braack and Prohl 2013; Bueno and Gomez 2016; Bueno et al. 2018; Diehl et al. 2016; Gomez et al. 2010; Lamorgese and Mauri 2009; Liu et al. 2013, 2015; Onuki 2007; Pecenko et al. 2010, 2011; Tian et al. 2015].

However, to properly describe the interfacial properties of a specific fluid a more evolved EoS needs to be employed. This is, to the best of the author's knowledge, done for the first time in [Diewald et al. 2018a].

The specific fluid that shall be described here is the Lennard-Jones truncated and shifted (LJTS) fluid. The LJTS model is probably the most simple model that can describe the interfacial properties as well as the overall thermodynamic behavior of a fluid realistically. For this reason it is often used for systematic thermodynamic studies of fluids and their interfaces by atomistic simulations, cf. [Becker et al. 2014; Heinen et al. 2016; Horsch et al. 2008, 2009, 2010, 2012; Lotfi et al. 2014; Stephan et al. 2018; Vrabec et al. 2006].

The LJTS model is based on the Lennard-Jones (LJ) [Jones 1924] potential

$$u^{\text{LJ}}(r^{\text{LJ}}) = 4\varepsilon^{\text{LJ}} \left[\left(\frac{\sigma^{\text{LJ}}}{r^{\text{LJ}}} \right)^{12} - \left(\frac{\sigma^{\text{LJ}}}{r^{\text{LJ}}} \right)^6 \right], \quad (4.27)$$

which describes the interaction of two particles that have a distance r^{LJ} to each other. The fluid specific constants ε^{LJ} and σ^{LJ} are the energy and size parameter of the LJ potential. The value of u^{LJ} at the potential well is defined by $-\varepsilon^{\text{LJ}}$ and the value of r^{LJ} at which u^{LJ} is zero is defined by σ^{LJ} . Values for ε^{LJ} and σ^{LJ} for specific fluids can, for instance, be found in [Vrabec et al. 2006]. A plot of u^{LJ} can be seen in Figure 4.3.

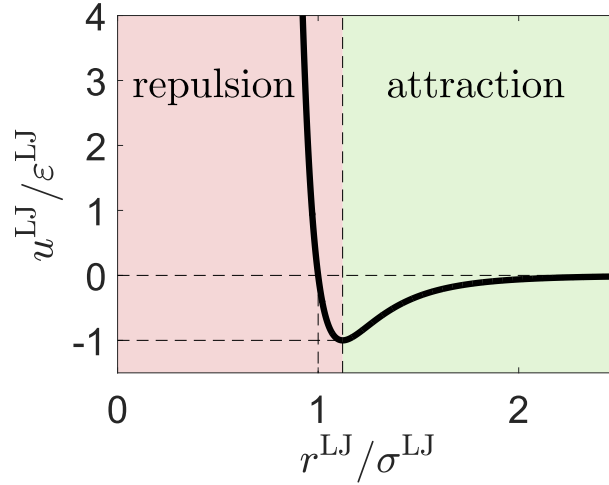


Figure 4.3: Plot of the LJ potential. The distance between two particles is denoted by r^{LJ} . The energy and size parameter are ϵ^{LJ} and σ^{LJ} . The LJ potential leads to an attraction between particles if r^{LJ} is larger than the position of the potential well and to a repulsion if r^{LJ} is smaller than the position of the potential well.

The LJ potential leads to an attraction between particles if r^{LJ} is larger than the position of the potential well and to a repulsion if r^{LJ} is smaller than the position of the potential well. The exponent of the attractive term $-(\sigma^{\text{LJ}}/r^{\text{LJ}})^6$ follows from electrostatics. The exponent of the repulsive term $(\sigma^{\text{LJ}}/r^{\text{LJ}})^{12}$ has to be larger than 6 to ensure that the attractive term is dominant for large values of r^{LJ} . However, its exact choice is purely empirical and not unique. Choosing 12 is convenient as it allows to compute the repulsive term by squaring the attractive term. [Lauth and Kowalczyk 2015]

The energy parameter ϵ^{LJ} and size parameter σ^{LJ} of the LJ potential and the mass per particle M^{LJ} can be used to nondimensionalize physical quantities, cf. Table 4.1. The nondimensionalized quantities are marked with an asterisk $(\cdot)^*$ and k_{B} is the Boltzmann constant. The according LJ units are used for all physical quantities whenever the EoS based Helmholtz free energy is used.

The LJTS potential u^{LJTS} is obtained from the LJ potential by truncating it at the cut-off radius r_c^{LJ} and shifting it such that $u^{\text{LJTS}}(r_c^{\text{LJ}}) = 0$,

$$u^{\text{LJTS}}(r^{\text{LJ}}) = \begin{cases} u^{\text{LJ}}(r^{\text{LJ}}) - u^{\text{LJ}}(r_c^{\text{LJ}}) & \text{for } r^{\text{LJ}} < r_c^{\text{LJ}} \\ 0 & \text{for } r^{\text{LJ}} \geq r_c^{\text{LJ}} \end{cases} . \quad (4.28)$$

The truncation reduces the numerical costs for MD simulations as particles that

Table 4.1: Nondimensionalization of physical quantities. The nondimensionalized quantities are marked with an asterisk (\cdot)*.

length	$l^* = \frac{l}{\sigma^{\text{LJ}}}$	temperature	$T^* = \frac{T}{\varepsilon^{\text{LJ}}/k_{\text{B}}}$
time	$t^* = \frac{t}{\sigma^{\text{LJ}}\sqrt{M^{\text{LJ}}/\varepsilon^{\text{LJ}}}}$	stress	$\boldsymbol{\sigma}^* = \frac{\boldsymbol{\sigma}}{\varepsilon^{\text{LJ}}/(\sigma^{\text{LJ}})^3}$
mass	$m^* = \frac{m}{M^{\text{LJ}}}$	velocity	$\vec{v}^* = \frac{\vec{v}}{\sqrt{\varepsilon^{\text{LJ}}/M^{\text{LJ}}}}$
mass density	$\rho^* = \frac{\rho}{M^{\text{LJ}}/(\sigma^{\text{LJ}})^3}$	viscosity	$\eta^{\text{v}*} = \frac{\eta^{\text{v}}}{\sqrt{\varepsilon^{\text{LJ}}M^{\text{LJ}}/(\sigma^{\text{LJ}})^2}}$
free energy per mass	$\psi^* = \frac{\psi}{\varepsilon^{\text{LJ}}/M^{\text{LJ}}}$	surface tension	$\gamma^* = \frac{\gamma}{\varepsilon^{\text{LJ}}/(\sigma^{\text{LJ}})^2}$

have a distance larger than r_c^{LJ} do not interact with each other. Throughout this work $r_c^{\text{LJ}} = 2.5\sigma^{\text{LJ}}$ is used.

Recently an EoS for the LJTS fluid was developed [Heier et al. 2018]. This PeTS (perturbed truncated and shifted) EoS matches the results of MD simulations of the LJTS fluid. The agreement between the PeTS EoS and MD simulations is not only found for stable states but also for metastable and unstable states. This is not the case for the only other two EoS for the LJTS fluid [Johnson et al. 1993; Thol et al. 2015]. It is therefore attractive to use the PeTS equation of state in a PF model for wetting scenarios of the LJTS fluid.

The EoS based Helmholtz free energy per mass ψ^{PeTS} used in this work is chosen such that

$$\rho\hat{\psi}(\rho, \nabla\rho) = \rho\psi^{\text{PeTS}}(\rho, \nabla\rho) = \rho a^{\text{PeTS}}(\rho) + \frac{1}{2}\kappa|\nabla\rho|^2. \quad (4.29)$$

In this $a^{\text{PeTS}}(\rho)$ is the local part of the EoS based Helmholtz free energy as it is described by the PeTS EoS. For more details on the specific form of $a^{\text{PeTS}}(\rho)$ the reader is referred to [Heier et al. 2018]. The high level of complexity of the PeTS EoS motivates the usage of hyper-dual numbers to compute the first and second derivatives that are needed for the FE implementation. See section 5.3 for details. In general $a^{\text{PeTS}}(\rho)$ does not only depend on the density ρ but also on the temperature T and therefore $a^{\text{PeTS}}(\rho, T)$. However, since the present PF model assumes the temperature to be constant, cf. section 3.4.1, the temperature T is omitted in the notation for ease of readability. A plot of $\rho a^{\text{PeTS}}(\rho)$ for $T = 0.7\frac{\varepsilon^{\text{LJ}}}{k_{\text{B}}}$ is shown in Figure 4.4 (left).

Similar to the empirical Helmholtz free energy, cf. section 4.1, the local part of the Helmholtz free energy $\rho a^{\text{PeTS}}(\rho)$ leads to the existence of two stable phases with

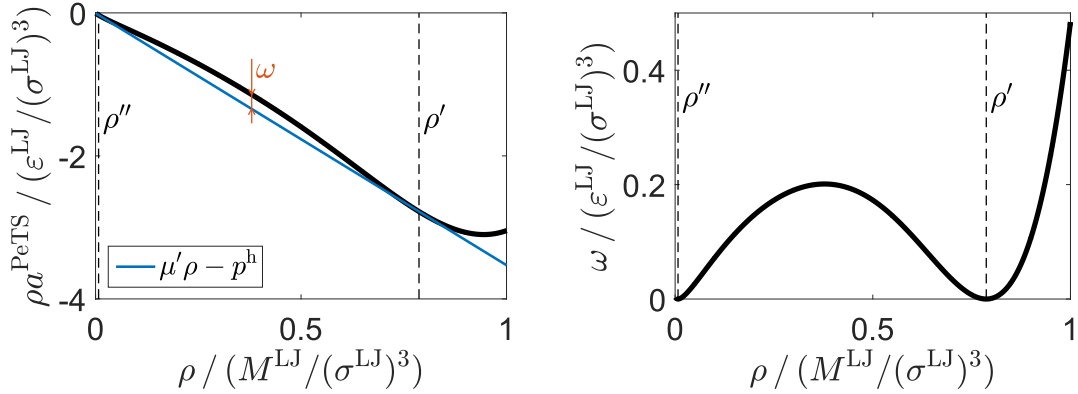


Figure 4.4: Left: Plot of $\rho a^{\text{PeTS}}(\rho)$ for $T = 0.7 \frac{\epsilon^{\text{LJ}}}{k_{\text{B}}}$. The densities of the bulk phases ρ'' and ρ' are depicted with dashed lines. The blue line represents the energy that results from simply mixing the energies of the homogeneous bulk phases. Right: Homogeneous excess free energy density. This energy results from subtracting the (blue) mixing energy from $\rho a^{\text{PeTS}}(\rho)$. [Heier et al. 2018; Diewald et al. 2018a]

densities ρ'' and ρ' which are marked by dashed lines in Figure 4.4. Since this local part of the Helmholtz free energy is directly taken from the PeTS EoS there is no additional parameter in front of it. Only one parameter κ in front of the gradient part of the Helmholtz free energy remains to be defined.

The parameter κ shall be chosen such that the energy of the liquid-vapor interface is defined by the surface tension between the two phases. Consequently, since κ is the only parameter, this also defines the width of the liquid-vapor interface. The interface width cannot be chosen separately and reflects the physical width of the liquid-vapor interface for the LJTS fluid at the nanoscale. Using the PeTS EoS together with the correct value for κ does therefore lead to PF simulations that are consistent with MD simulations regarding the bulk phases as well as the interface between them. This is demonstrated in section 6.2. The computational effort is smaller for the PF simulations than for the MD simulations. Therefore, the PF model based on the Helmholtz free energy from the PeTS EoS does already allow to compute scenarios in larger domains than the MD simulations. However, the nanoscale width of the liquid-vapor interface ties the PF simulations to small scales. A true scale bridging can be achieved by introducing an additional parameter in the Helmholtz free energy in order to broaden the liquid-vapor interface, cf. chapter 7. As the PF model strongly reflects the underlying physics from the MD simulations it can be used to transfer the insights from the MD simulations to much larger scales.

The computation of the parameter κ is presented in the following. The underlying idea was shown in [Cahn and Hilliard 1958]. Analogous to section 4.1, a planar interface that is perpendicular to an axis x and is located at $x = 0$ is regarded. Gravitational effects are neglected ($g = 0$). The excess free energy Ω^{PeTS} , which is the energy that is stored in that interface, is given by

$$\Omega^{\text{PeTS}} = A \int_{-\infty}^{\infty} \left[\omega(\rho) + \frac{1}{2} \kappa |\nabla \rho|^2 \right] dx. \quad (4.30)$$

In contrast to the empirical Helmholtz free energy, the EoS based Helmholtz free energy shows a non-zero free energy for the bulk phases $\rho' a^{\text{PeTS}}(\rho') \neq 0$ and $\rho'' a^{\text{PeTS}}(\rho'') \neq 0$, cf. Figure 4.4 (left). Therefore, the excess free energy cannot directly be computed using $\rho a^{\text{PeTS}}(\rho)$. Instead the energy that would result from simply mixing the energies of the homogeneous bulk phases has to be subtracted. This is done by using the homogeneous excess free energy density ω ,

$$\omega(\rho) = \rho a^{\text{PeTS}}(\rho) - \mu' \rho + p^{\text{h}}, \quad (4.31)$$

in (4.30). In this μ' is the chemical potential in the homogeneous liquid phase,

$$\mu' = \left. \frac{\partial(\rho a^{\text{PeTS}})}{\partial \rho} \right|_{\rho=\rho'}, \quad (4.32)$$

see also (3.39). Note that the chemical potential in the homogeneous vapor phase ρ'' could also be used since the chemical potential is constant for an equilibrium configuration. The hydrostatic pressure is given by p^{h} . A plot of $\omega(\rho)$ is shown in Figure 4.4 (right). Naturally, the value of ω in the bulk phases is zero,

$$\omega(\rho') = \omega(\rho'') = 0. \quad (4.33)$$

Analogous to section 4.1, the excess free energy Ω^{PeTS} has to be equal to the surface tension between the liquid and the vapor phase γ_{lv} multiplied with A ,

$$\Omega^{\text{PeTS}} = A \gamma_{\text{lv}}. \quad (4.34)$$

Reusing (4.11) and writing it for the EoS based Helmholtz free energy of this section (4.29) at the position of one of the bulk phases (e.g. the liquid bulk phase) gives

$$\rho' a^{\text{PeTS}}(\rho') + \lambda \rho' = c \quad (4.35)$$

since $\frac{d\rho}{dx} = 0$ in the bulk phases. From (4.31) and (4.33) it follows that

$$\rho' a^{\text{PeTS}}(\rho') = \mu' \rho' - p^{\text{h}}. \quad (4.36)$$

In addition, (3.66) and (4.32) yield

$$\lambda = -\mu'. \quad (4.37)$$

Inserting (4.36) and (4.37) in (4.35) gives

$$c = -p^h. \quad (4.38)$$

With this, (4.11) can be written for the EoS based Helmholtz free energy (4.29) at any position as

$$\rho a^{\text{PeTS}}(\rho) - \mu' \rho + p^h = \frac{1}{2} \kappa \left(\frac{d\rho}{dx} \right)^2 \quad \text{or} \quad \omega(\rho) = \frac{1}{2} \kappa \left(\frac{d\rho}{dx} \right)^2. \quad (4.39)$$

Using this result in the requirement regarding the energy of the interface that is stated in (4.34) leads to

$$\int_{-\infty}^{\infty} \left[\omega(\rho) + \frac{1}{2} \kappa |\nabla \rho|^2 \right] dx = \int_{-\infty}^{\infty} 2\omega(\rho) dx = \gamma_{lv}. \quad (4.40)$$

With

$$dx = \sqrt{\frac{\kappa}{2\omega(\rho)}} d\rho, \quad (4.41)$$

cf. (4.39), the integral over x can be rewritten as an integral over ρ

$$\int_{-\infty}^{\infty} 2\omega(\rho) dx = \int_{\rho''}^{\rho'} \sqrt{2\kappa\omega(\rho)} d\rho = \gamma_{lv}. \quad (4.42)$$

Therefore, κ can be computed with

$$\kappa = \frac{1}{2} \left[\frac{\gamma_{lv}}{\int_{\rho''}^{\rho'} \sqrt{\omega(\rho)} d\rho} \right]^2. \quad (4.43)$$

Using the data for γ_{lv} presented in [Vrabec et al. 2006] the value of κ for the PeTS EoS can be computed. It is shown in [Heier et al. 2018] that a temperature independent value of $\kappa = 2.7334 \frac{\varepsilon^{\text{LJ}} (\sigma^{\text{LJ}})^5}{(M^{\text{LJ}})^2}$ is appropriate. This value is used in this work whenever the EoS based Helmholtz free energy is used.

Surface Energy

The surface energy ϕ^{PeTS} is chosen analogous to the surface energy for the empirical Helmholtz free energy, cf. section 4.1. It represents the surface tension between the solid surface and the liquid γ_{sl} if the liquid is in contact with the solid surface, as well as the surface tension between the solid surface and the vapor γ_{sv} if the vapor is in contact with the solid surface,

$$\rho\hat{\phi}(\rho) = \rho\phi^{\text{PeTS}}(\rho) = \gamma_{\text{sl}}h(\rho) + \gamma_{\text{sv}}(1 - h(\rho)) , \quad (4.44)$$

cf. [Ben Said et al. 2014]. Again, $h(\rho)$ interpolates between the solid-liquid and solid-vapor interface

$$h(\rho) = \left(\frac{\rho - \rho''}{\rho' - \rho''} \right)^3 \left[6 \left(\frac{\rho - \rho''}{\rho' - \rho''} \right)^2 - 15 \left(\frac{\rho - \rho''}{\rho' - \rho''} \right) + 10 \right] , \quad (4.45)$$

which yields

$$h(\rho = \rho'') = 0 \quad \text{and} \quad h(\rho = \rho') = 1 . \quad (4.46)$$

Note that with (4.2) the formulations for the surface energy for the empirical Helmholtz free energy and the EoS based Helmholtz free energy are identical. The remarks that were made in section 4.1 do therefore hold here as well.

Alternative View on the Korteweg Stress Tensor

The elaborations above allow an alternative (or phenomenological) view on the Korteweg stress tensor that was derived in section 3.4, cf. (3.51). This alternative view, which is presented in the following, yields deeper insights into the underlying physics than the purely mathematical derivation of section 3.4 does.

The density ρ is identified as the order parameter of the present PF model, cf. section 3.4.2. Therefore, the Navier-Stokes-Korteweg model can be seen as a model that couples a PF model that does only describe the evolution of different phases characterized by the density distribution with a model for fluid dynamics i.e. the mass and momentum balance.

The coupling from the fluid dynamics to the PF model for the density distribution is inherent in the mass balance

$$\frac{\partial \rho}{\partial t} + \nabla \rho \cdot \vec{v} + \rho \text{div} \vec{v} = 0 , \quad (4.47)$$

cf. (3.13). It is evident that interfaces, which are represented by a non-zero value of $\nabla \rho$, are convected with the flow.

The coupling from the PF model for the density distribution to the fluid dynamics is less obvious. It is achieved by a constitutive relation between the stress tensor and the density distribution.

It follows from (4.39) that the hydrostatic pressure in a domain that is at equilibrium and contains one planar interface between the liquid and the vapor phase is constant and given by

$$p^h = -\rho a^{\text{PeTS}}(\rho) + \mu' \rho + \frac{1}{2} \kappa |\nabla \rho|^2. \quad (4.48)$$

It is suggestive to use this expression to define a (non-constant) hydrostatic pressure tensor \mathbf{p}^h that represents the first part of the constitutive relation between the stress tensor and the density distribution,

$$\mathbf{p}^h = p^h \mathbf{1} = \left(-\rho a^{\text{PeTS}}(\rho) + \mu' \rho + \frac{1}{2} \kappa |\nabla \rho|^2 \right) \mathbf{1}. \quad (4.49)$$

For an interface that is at equilibrium, \mathbf{p}^h is constant in the entire domain. If the density distribution evolves away from the equilibrium by e.g. broadening the interface, the hydrostatic pressure drops at the interface as the $\nabla \rho$ contribution becomes smaller. This pressure drop causes a flow towards the interface which narrows the interface and restores the equilibrium state.

While \mathbf{p}^h stabilizes the interface, it does not describe the influence that the surface tension has on the fluid dynamics. This influence of the surface tension is described by the surface tension pressure tensor $\mathbf{p}^{\gamma_{lv}}$, that represents the second part of the constitutive relation between the stress tensor and the density distribution. A single two-dimensional droplet as it is depicted in Figure 4.5 is regarded in the following. Section 2.1 describes that the surface tension of the liquid-vapor interface can be understood as the integral over a pressure drop that is found in the direction of the diffuse interface between the phases. In other words, moving along an axis ξ that is perpendicular to the liquid-vapor interface, a pressure drop can be seen in the direction η , which is perpendicular to ξ . The integral over this pressure drop in ξ -direction yields the surface tension γ_{lv} with a change of sign. The change of sign is easy to comprehend. The surface tension gives a positive energy contribution in the interface. However, the effect of the surface tension is a contraction of the interface originating from a negative pressure change in the interface.

With (4.34) it is evident that the pressure drop in the direction of the interface is equivalent to the excess free energy density (with a change of sign). This allows

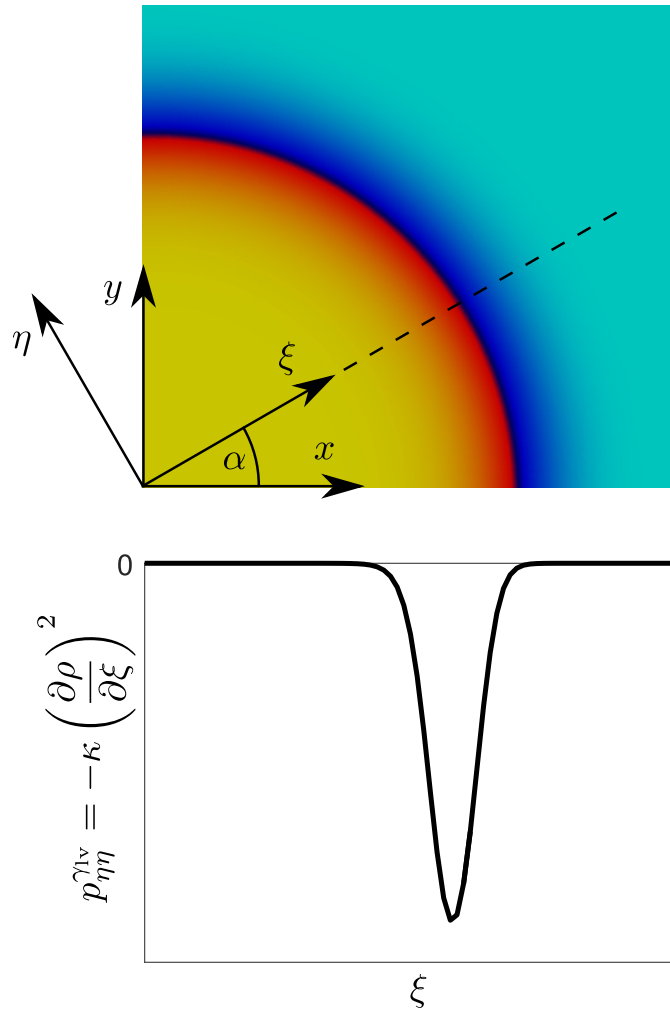


Figure 4.5: Two-dimensional droplet. The integral over the pressure drop that is found in the direction of the interface defines the surface tension between the liquid and the vapor phase γ_{lv} .

to write the surface tension pressure tensor $\mathbf{p}^{\gamma_{lv}}$ in the $\xi\eta$ -coordinate system

$$\mathbf{p}_{(\xi\eta)}^{\gamma_{lv}} = \begin{bmatrix} 0 & 0 \\ 0 & -\omega(\rho) - \frac{1}{2}\kappa|\nabla\rho|^2 \end{bmatrix} = \begin{bmatrix} 0 & 0 \\ 0 & -\kappa|\nabla\rho|^2 \end{bmatrix} = \begin{bmatrix} 0 & 0 \\ 0 & -\kappa\left(\frac{\partial\rho}{\partial\xi}\right)^2 \end{bmatrix} \quad (4.50)$$

for which (4.39) was used. The surface tension pressure tensor $\mathbf{p}_{(\xi\eta)}^{\gamma_{lv}}$ can be transformed to the xy -coordinate system by a rotation of the coordinate system, see e.g. [Becker and Gross 2002]. The rotation angle α depends on the orientation of

the interface,

$$\sin \alpha = \frac{\partial \rho}{\partial y} \frac{1}{|\nabla \rho|} \quad \text{and} \quad \cos \alpha = \frac{\partial \rho}{\partial x} \frac{1}{|\nabla \rho|}. \quad (4.51)$$

Applying the rotation yields the surface tension pressure tensor in the xy -coordinate system

$$\mathbf{p}^{\gamma_{lv}} = \kappa \begin{bmatrix} -\left(\frac{\partial \rho}{\partial y}\right)^2 & \frac{\partial \rho}{\partial x} \frac{\partial \rho}{\partial y} \\ \frac{\partial \rho}{\partial x} \frac{\partial \rho}{\partial y} & -\left(\frac{\partial \rho}{\partial x}\right)^2 \end{bmatrix}. \quad (4.52)$$

The combination of the hydrostatic pressure tensor \mathbf{p}^h and the surface tension pressure tensor $\mathbf{p}^{\gamma_{lv}}$ is equivalent to the Korteweg stress tensor (3.51) that was derived in section 3.4,

$$\begin{aligned} \boldsymbol{\sigma}^\psi &= -\mathbf{p}^h - \mathbf{p}^{\gamma_{lv}} \\ &= \left(\rho a^{\text{PeTS}}(\rho) - \mu' \rho - \frac{1}{2} \kappa |\nabla \rho|^2 \right) \mathbf{1} + \kappa \begin{bmatrix} \left(\frac{\partial \rho}{\partial y}\right)^2 & -\frac{\partial \rho}{\partial x} \frac{\partial \rho}{\partial y} \\ -\frac{\partial \rho}{\partial x} \frac{\partial \rho}{\partial y} & \left(\frac{\partial \rho}{\partial x}\right)^2 \end{bmatrix} \\ &= \left(\rho a^{\text{PeTS}}(\rho) - \mu' \rho + \frac{1}{2} \kappa |\nabla \rho|^2 \right) \mathbf{1} - \kappa \begin{bmatrix} \left(\frac{\partial \rho}{\partial x}\right)^2 & \frac{\partial \rho}{\partial x} \frac{\partial \rho}{\partial y} \\ \frac{\partial \rho}{\partial x} \frac{\partial \rho}{\partial y} & \left(\frac{\partial \rho}{\partial y}\right)^2 \end{bmatrix}. \end{aligned} \quad (4.53)$$

The elaborations above demonstrate that the formulation of the Korteweg stress tensor can not only be understood as a constitutive relation that fulfills the free energy dissipation inequality as it is derived by the Coleman-Noll procedure. Instead, it can also be understood as a constitutive equation that:

- Defines and stabilizes the interface between the liquid and the vapor phase in the same way the first order optimality condition of the total PF potential does, cf. sections 3.1 and 3.5.2.
- Includes the effects of the surface tension between the liquid and the vapor phase.

4.3 Viscosity

Choices for the Helmholtz free energy and surface energy are made in the sections above. They can be used in the general Navier-Stokes-Korteweg model in the box on page 26 in order to make the model fluid specific. The viscosity η^v remains to be defined.

The present model considers Newtonian fluids, see e.g. [Böswirth et al. 2014]. The viscosity η^v does therefore not depend on the velocity respectively the velocity gradient. In this work, the viscosity is assumed to only depend on the local value of the density ρ and the temperature T . This section presents a physically motivated choice for this dependency.

The PeTS EoS is based on MD simulations of the LJTS fluid. By using the PeTS EoS in the formulation of the Helmholtz free energy of the PF model, the PF model strongly reflects the physical behavior of the LJTS fluid. It is therefore desirable to also define the viscosity such that it is in accordance with MD data for the LJTS fluid. For this the MD data for the viscosity from Lautenschlaeger and Hasse [2019] is used.

To define the viscosity η^v the following correlation is used

$$\eta^v(\rho, T) = \exp \left(\sum_{i=0}^4 \sum_{j=0}^i a_{[j][i-j]} \frac{\rho^j}{T^{i-j}} \right). \quad (4.54)$$

The parameters $a_{[j][i]}$ are determined by the method of least squares from the data presented in [Lautenschlaeger and Hasse 2019]. The resulting values are shown in Table 4.2. The values are stated without dimensions for ease of readability. This correlation is also presented in [Diewald et al. 2020a].

Table 4.2: Coefficients $a_{[j][i]}$ for the viscosity correlation of the LJTS fluid (4.54). The coefficients are determined by the method of least squares from the viscosity data presented in [Lautenschlaeger and Hasse 2019] and stated without dimensions. [Diewald et al. 2020a]

coeff.	value	coeff.	value	coeff.	value	coeff.	value
a_{00}	-0.09629	a_{02}	6.51120	a_{03}	-3.80749	a_{04}	0.73834
a_{01}	-5.77337	a_{11}	6.16606	a_{12}	-3.03103	a_{13}	1.33136
a_{10}	0.79147	a_{20}	0.21344	a_{21}	-5.65017	a_{22}	-0.69558
				a_{30}	0.73455	a_{31}	5.25442
						a_{40}	-0.38581

Figure 4.6 and Figure 4.7 compare the results from the viscosity correlation and the corresponding MD data. As can be seen in Figure 4.6 the correlation agrees well with the MD data for a wide density and temperature range. Figure 4.7 shows the viscosity correlation for two temperatures, $T = 0.7 \frac{\varepsilon^{\text{LJ}}}{k_{\text{B}}}$ and $T = 0.9 \frac{\varepsilon^{\text{LJ}}}{k_{\text{B}}}$, together with the MD data points closest to these temperatures. The plots show the correlation in the meta- and unstable region. In [Lautenschlaeger and Hasse 2019] no viscosity data is reported for meta- and unstable states. Since the PF model needs a defined viscosity for these states, the correlation is used for meta- and unstable states as well.

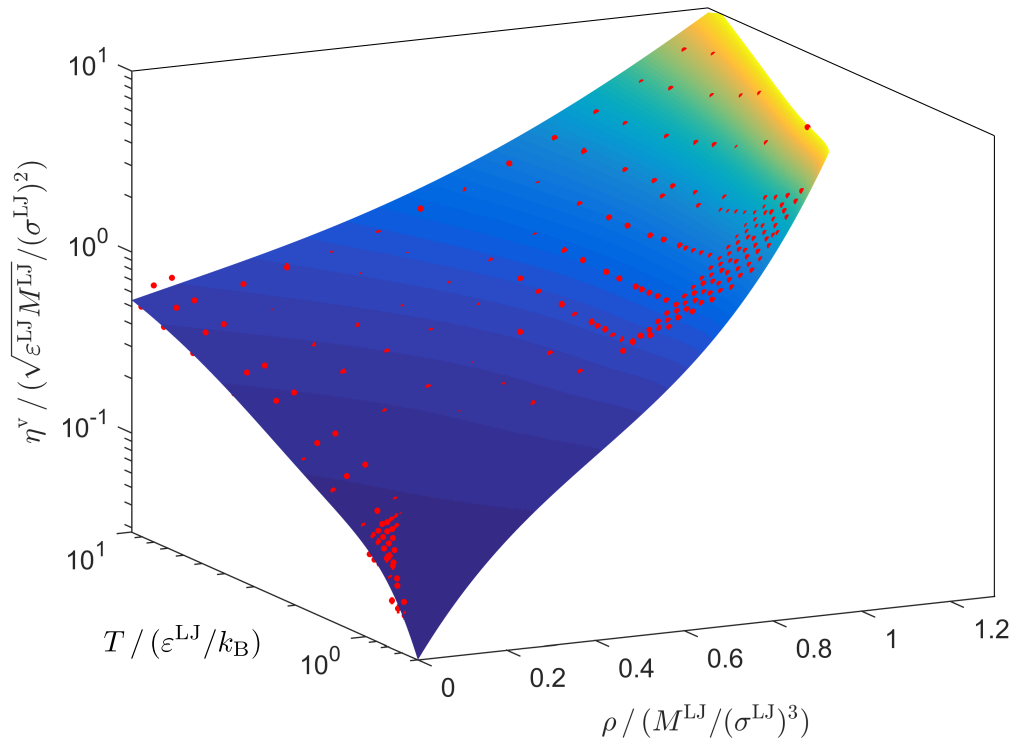


Figure 4.6: Viscosity of the LJTS fluid η^{v} as a function of density ρ and temperature T . The plot compares the viscosity data of MD simulations as reported in [Lautenschlaeger and Hasse 2019] with the viscosity correlation stated in (4.54). The symbols represent the MD data and the surface shows the results from the correlation. For meta- and unstable states, Lautenschlaeger and Hasse [2019] do not report any viscosity data. Nevertheless, the correlation is also used for these states. [Diewald et al. 2020a]

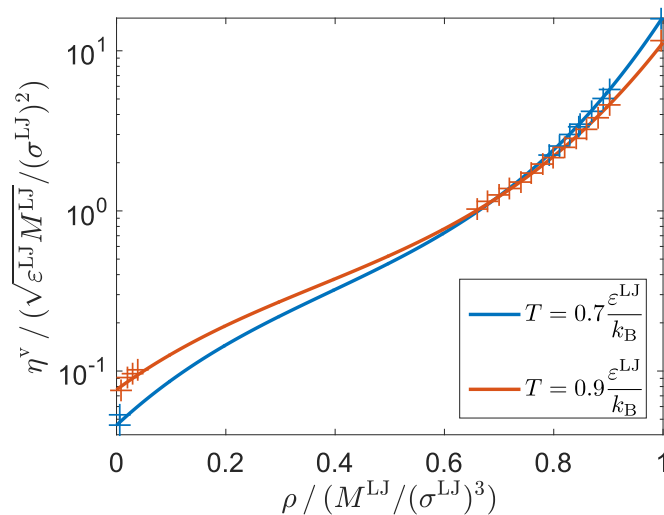


Figure 4.7: Viscosity of the LJTS fluid η^v along two isotherms. The plot compares the viscosity data of MD simulations as reported in [Lautenschlaeger and Hasse 2019] with the viscosity correlation stated in (4.54). The symbols represent the MD data and the lines show the results from the correlation. For meta- and unstable states, Lautenschlaeger and Hasse [2019] do not report any viscosity data. Nevertheless, the correlation is also used for these states. [Diewald et al. 2020a]

5 FE Implementation

For complex scenarios, it is not feasible to solve the dynamic Navier-Stokes-Korteweg model as stated in the box on page 26 or the static Allen-Cahn model as stated in the box on page 29 manually. Therefore, it becomes necessary to implement the models into a numerical solution scheme such that it can be solved with the help of a computer. This requires to discretize the problem with respect to time and space. Various options exist for both, the temporal and the spatial discretization.

This chapter presents two options for the temporal discretization. First a standard option using the backward Euler scheme is presented. Thereafter a newly developed [Diewald et al. 2020b] semi-implicit energy stable time integration scheme, that ensures the dissipation of energy, is introduced.

For the spatial discretization the finite element (FE) method is chosen. In the case of the dynamic Navier-Stokes-Korteweg model the spatial discretization utilizes the mixed FE method and discretizes the velocity with quadratic and the density as well as the chemical potential with linear shape functions (Q2P1). The static Allen-Cahn model relies on linear shape functions. For further reading on the FE method the reader is referred to the textbooks of Bathe [1996], Bonet and Wood [2009], Brezzi and Fortin [1991], Taylor and Hughes [1981], Thomasset [1981], Wriggers [2001], Zienkiewicz and Taylor [2006], and Zienkiewicz et al. [2009].

The implementation is based on the FE program FEAP version 8.4 [FEAP 84]. FEAP provides basic FE routines for e.g. the shape functions and handles the assembly. The implementation of the dynamic Navier-Stokes-Korteweg and the static Allen-Cahn model is realized with self-coded routines that are formulated on element level. To solve the resulting system of equations on the global level, parallel solvers on CPU- and GPU-architectures, that were implemented into FEAP at the Institute of Applied Mechanics of the Technische Universität Kaiserslautern, are used.

The last section of this chapter introduces the reader to the concept of hyper-

dual numbers. Hyper-dual numbers are used in this work to compute exact and step-size independent values of first and second derivatives of the Helmholtz free energy. They enable the computation of these derivative values without an explicit differentiation. This approach allows an easy and robust exchange of the Helmholtz free energy and the underlying EoS.

5.1 Temporal Discretization

The continuous course of time is split into discrete time steps and the models are evaluated at these time steps, only. The current time step is denoted by n and the time step size, i.e. the time that passes between two time steps, is given by Δt , cf. Figure 5.1.

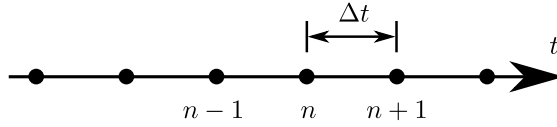


Figure 5.1: Temporal discretization.

In the following, the two time integration schemes that are used in this work are presented. The backward Euler scheme is used for both the dynamic Navier-Stokes-Korteweg and the static Allen-Cahn model (with evolution equation) and for both choices of the Helmholtz free energy that are presented in chapter 4. The semi-implicit energy stable scheme is only used for the dynamic Navier-Stokes-Korteweg model that utilizes the EoS based Helmholtz free energy.

5.1.1 Backward Euler Scheme

The backward Euler scheme is a fully implicit time integration scheme. All physical quantities are taken from the next time step \mathcal{A}^{n+1} and the time derivative is approximated by

$$\frac{\partial \mathcal{A}}{\partial t} \approx \frac{\mathcal{A}^{n+1} - \mathcal{A}^n}{\Delta t}. \quad (5.1)$$

In this, the superscript shows the time step to which the physical quantity belongs to.

For the dynamic Navier-Stokes-Korteweg model, the physical quantities, or degrees of freedom, are the velocity \vec{v} , the density ρ , and the chemical potential μ . The chemical potential could also be expressed in terms of the density. Choosing it as an individual degree of freedom brings numerical advantages, cf. section 5.2.1. For the static Allen-Cahn model, the degrees of freedom are the density ρ and

the Lagrange multiplier λ . Note that in the context of the numerical solution strategy the term “degree of freedom” refers to the variable that represents the corresponding physical quantity. The term is therefore not used in the way that is common in the field of thermodynamics where it refers to physical quantities that can be chosen independently, e.g. density and temperature.

The backward Euler version of the dynamic Navier-Stokes-Korteweg model of this work, cf. box on page 26, reads

1. Set initial values $n = 0$, ρ^0 , \vec{v}^0 , μ^0 .

2. Solve

$$\frac{\rho^{n+1} - \rho^n}{\Delta t} + \operatorname{div}(\rho^{n+1} \vec{v}^{n+1}) = 0, \quad (5.2)$$

$$\begin{aligned} \rho^{n+1} \frac{\vec{v}^{n+1} - \vec{v}^n}{\Delta t} + \rho^{n+1} \nabla \vec{v}^{n+1} \vec{v}^{n+1} &= \operatorname{div} [\boldsymbol{\sigma}(\rho^{n+1}, \nabla \rho^{n+1}, \vec{v}^{n+1}, \mu^{n+1})] \\ &\quad - \rho^{n+1} g \vec{e}_g, \end{aligned} \quad (5.3)$$

$$\begin{aligned} \mu^{n+1} &= \frac{\partial(\rho \hat{\psi}(\rho, \nabla \rho))}{\partial \rho} \Big|_{\rho^{n+1}} \\ &\quad - \operatorname{div} \frac{\partial(\rho \hat{\psi}(\rho, \nabla \rho))}{\partial \nabla \rho} \Big|_{\rho^{n+1}}, \end{aligned} \quad (5.4)$$

in \mathcal{B} and under the boundary conditions

$$\vec{v}^{n+1} = \vec{0} \quad \text{on} \quad \partial \mathcal{B} \cap \partial \mathcal{B}_s, \quad (5.5)$$

$$\frac{\partial(\rho \hat{\psi}(\rho, \nabla \rho))}{\partial \nabla \rho} \Big|_{\nabla \rho^{n+1}} \cdot \vec{n} + \frac{\partial(\rho \hat{\phi}(\rho))}{\partial \rho} \Big|_{\rho^{n+1}} = 0 \quad \text{on} \quad \partial \mathcal{B} \cap \partial \mathcal{B}_s, \quad (5.6)$$

$$\frac{\partial(\rho \hat{\psi}(\rho, \nabla \rho))}{\partial \nabla \rho} \Big|_{\nabla \rho^{n+1}} \cdot \vec{n} = 0 \quad \text{on} \quad \partial \mathcal{B} \setminus \partial \mathcal{B}_s. \quad (5.7)$$

3. $n = n + 1$ go to 2.

Non-conservative volume forces are neglected ($\vec{b}_0 = \vec{0}$).

The backward Euler version of the static Allen-Cahn model of this work, cf. box on page 29, reads

1. Set initial values $n = 0, \rho^0$.

2. Solve

$$\frac{\partial(\rho\hat{\psi}(\rho, \nabla\rho))}{\partial\rho}\Bigg|_{\rho^{n+1}} - \operatorname{div}\frac{\partial(\rho\hat{\psi}(\rho, \nabla\rho))}{\partial\nabla\rho}\Bigg|_{\nabla\rho^{n+1}} + gx_g + \lambda = -\frac{1}{M}\frac{\rho^{n+1} - \rho^n}{\Delta t}, \quad (5.8)$$

$$\int_{\mathcal{B}} \rho^{n+1} dV = m_{\mathcal{B}}, \quad (5.9)$$

in \mathcal{B} and under the boundary conditions

$$\frac{\partial(\rho\hat{\psi}(\rho, \nabla\rho))}{\partial\nabla\rho}\Bigg|_{\nabla\rho^{n+1}} \cdot \vec{n} + \frac{\partial(\rho\hat{\phi}(\rho))}{\partial\rho}\Bigg|_{\rho^{n+1}} = 0 \quad \text{on } \partial\mathcal{B} \cap \partial\mathcal{B}_s, \quad (5.10)$$

$$\frac{\partial(\rho\hat{\psi}(\rho, \nabla\rho))}{\partial\nabla\rho}\Bigg|_{\nabla\rho^{n+1}} \cdot \vec{n} = 0 \quad \text{on } \partial\mathcal{B} \setminus \partial\mathcal{B}_s. \quad (5.11)$$

3. $n = n + 1$ go to 2.

To make these general models specific, the explicit forms of $\hat{\psi}(\rho, \nabla\rho)$ and $\hat{\phi}(\rho)$ for the empirical Helmholtz free energy or the EoS based Helmholtz free energy can be used.

With the backward Euler time integration scheme the dynamic Navier-Stokes-Korteweg model and the static Allen-Cahn model represent a non-linear system of equations for ρ^{n+1} , \vec{v}^{n+1} , and μ^{n+1} or ρ^{n+1} , respectively. These non-linear systems of equations can be abstracted to

$$G(\mathcal{A}^{n+1}) = 0. \quad (5.12)$$

With G being a non-linear function and

$$\mathcal{A}^{n+1} \triangleq \begin{cases} \rho^{n+1}, \vec{v}^{n+1}, \mu^{n+1} & \text{for the dynamic Navier-Stokes-Korteweg model} \\ \rho^{n+1} & \text{for the static Allen-Cahn model} \end{cases}. \quad (5.13)$$

They can be solved (step 2 in the boxes above) by the Newton-Raphson method:

1. Set initial values $k = 0, \mathcal{A}_0^{n+1}$.

2. Solve $\frac{\partial G(\mathcal{A}^{n+1})}{\partial \mathcal{A}^{n+1}} \Big|_{\mathcal{A}_k^{n+1}} \Delta \mathcal{A}_{k+1}^{n+1} = -G(\mathcal{A}_k^{n+1})$.
3. $\mathcal{A}_{k+1}^{n+1} = \mathcal{A}_k^{n+1} + \Delta \mathcal{A}_{k+1}^{n+1}$.
4. Check $|G(\mathcal{A}_{k+1}^{n+1})| \begin{cases} > \text{tolerance} : & k = k + 1 \text{ go to 2} \\ \leq \text{tolerance} : & \text{stop} \end{cases}$.

See e.g. [Wriggers 2001]. Above, k is the counter for the Newton-Raphson iteration and $\Delta(\cdot)$ denotes an increment. A sketch for the first steps of a one-dimensional Newton-Raphson method is shown in Figure 5.2.

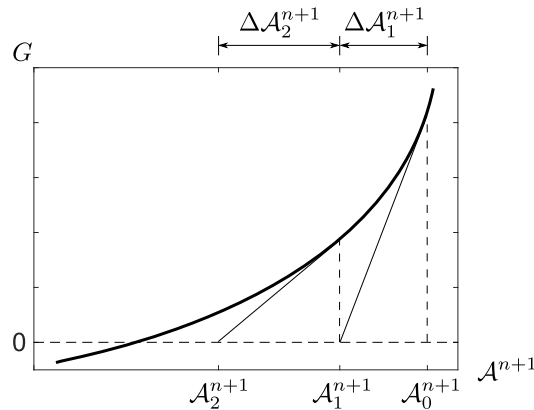


Figure 5.2: Sketch of first steps of a one-dimensional Newton-Raphson method.

5.1.2 Semi-Implicit Energy Stable Scheme

Besides the disadvantage of leading to a non-linear system of equations, the backward Euler scheme does not guarantee the dissipation of energy, that is shown for the continuous model in section 3.4.3, in a time discrete manner [Gomez and van der Zee 2017]. The development of practical schemes is still an open field of research, see e.g. [Shen et al. 2017; Strasser et al. 2019]. The newly developed semi-implicit energy stable time integration scheme that is presented in the following yields a linear system of equations and is guaranteed to dissipate energy. The scheme is presented in [Diewald et al. 2020b], on which this section is based. It is shown here for the dynamic Navier-Stokes-Korteweg model with the EoS based Helmholtz free energy. However, the scheme can easily be adapted for the empirical Helmholtz free energy.

The semi-implicit energy stable time integration scheme for the dynamic Navier-Stokes-Korteweg model of this work, cf. box on page 26, with the EoS based Helmholtz free energy, cf. section 4.2, reads

1. Set initial values $n = 0$, ρ^0 , ρ^{-1} , \vec{v}^0 , μ^0 .

2. Solve

$$\frac{\rho^{n+1} - \rho^n}{\Delta t} + \operatorname{div}(\rho^n \vec{v}^{n+1}) = 0, \quad (5.14)$$

$$\begin{aligned} & \frac{1}{2} \left(\frac{\rho^n \vec{v}^{n+1} - \rho^{n-1} \vec{v}^n}{\Delta t} \right) \\ & + \frac{1}{2} \rho^{n-1} \left(\frac{\vec{v}^{n+1} - \vec{v}^n}{\Delta t} \right) \\ & + \frac{1}{2} \rho^n \nabla \vec{v}^{n+1} \vec{v}^n \\ & + \frac{1}{2} \operatorname{div}(\rho^n \vec{v}^n \otimes \vec{v}^{n+1}) \quad = \operatorname{div} \left[2\eta^v(\rho^n) \left(\nabla^s \vec{v}^{n+1} - \frac{1}{3} \operatorname{tr}(\nabla^s \vec{v}^{n+1}) \mathbf{1} \right) \right] \\ & \quad - \rho^n \nabla \mu^{n+1} - \rho^n g \vec{e}_g, \end{aligned} \quad (5.15)$$

$$\begin{aligned} \mu^{n+1} & = \beta^s (\rho^{n+1} - \rho^n) + \frac{\partial(\rho \alpha^{\text{PeTS}})}{\partial \rho} \Big|_{\rho^n} \\ & \quad - \operatorname{div}(\kappa \nabla \rho^{n+1}), \end{aligned} \quad (5.16)$$

in \mathcal{B} and under the boundary conditions

$$\vec{v}^{n+1} = \vec{0} \quad \text{on} \quad \partial \mathcal{B} \cap \partial \mathcal{B}_s, \quad (5.17)$$

$$\begin{aligned} & \kappa \nabla \rho^{n+1} \cdot \vec{n} \\ & + (\gamma_{\text{sl}} - \gamma_{\text{sv}}) \left[\alpha^s (\rho^{n+1} - \rho^n) + \frac{\partial h(\rho)}{\partial \rho} \Big|_{\rho^n} \right] = 0 \quad \text{on} \quad \partial \mathcal{B} \cap \partial \mathcal{B}_s, \end{aligned} \quad (5.18)$$

$$\nabla \rho^{n+1} \cdot \vec{n} = 0 \quad \text{on} \quad \partial \mathcal{B} \setminus \partial \mathcal{B}_s. \quad (5.19)$$

3. $n = n + 1$ go to 2.

Again, non-conservative volume forces are neglected ($\vec{b}_0 = \vec{0}$). In (5.15) the identity

$$\rho \dot{\vec{v}} = \rho \frac{\partial \vec{v}}{\partial t} + \rho \nabla \vec{v} \vec{v} = \frac{1}{2} \frac{\partial(\rho \vec{v})}{\partial t} + \frac{1}{2} \rho \frac{\partial \vec{v}}{\partial t} + \frac{1}{2} \rho \nabla \vec{v} \vec{v} + \frac{1}{2} \operatorname{div}(\rho \vec{v} \otimes \vec{v}), \quad (5.20)$$

which holds due to (3.13), is used to rewrite the left-hand side. The identity (3.60) is used to rewrite the right-hand side.

A convex-concave splitting is used for the local part of the Helmholtz free energy and the surface energy, cf. (5.16) and (5.18). The constants β^s and α^s are the respective stabilization parameters. For more details regarding the convex-concave splitting, see [Eyre 1998; Shokrpour Roudbari et al. 2018].

As can be seen, this time integration scheme does not only regard the current time step n and the next time step $n + 1$ but also the previous time step $n - 1$. This requires the usage of history variables for the implementation into FEAP.

The semi-implicit time integration scheme as stated in the box above represents a linear system of equations for ρ^{n+1} , \vec{v}^{n+1} , and μ^{n+1} . This linear system of equations can be abstracted to

$$H^n \mathcal{A}^{n+1} = h^n \quad \text{with} \quad \mathcal{A}^{n+1} \hat{=} \rho^{n+1}, \vec{v}^{n+1}, \mu^{n+1}. \quad (5.21)$$

In this, H^n and h^n are constants that can be computed using information from the current time step n and the last time step $n - 1$, only. The solution (step 2 in the boxes above) can directly be obtained, $\mathcal{A}^{n+1} = (H^n)^{-1} h^n$.

Proof Energy Stability

The semi-implicit time integration scheme presented above dissipates energy if certain requirements for the constants β^s and α^s are fulfilled. The proof is presented in the following.

The discrete equivalence to the continuous energy change in time as stated by (3.62) is

$$\begin{aligned} E^{n+1} - E^n &= E[\vec{v}^{n+1}, \rho^{n+1}, \nabla \rho^{n+1}] - E[\vec{v}^n, \rho^n, \nabla \rho^n] \\ &= \int_{\mathcal{B}} \left[\rho^{n+1} a^{\text{PeTS}}(\rho^{n+1}) - \rho^n a^{\text{PeTS}}(\rho^n) + \frac{1}{2} \kappa (|\nabla \rho^{n+1}|^2 - |\nabla \rho^n|^2) \right. \\ &\quad \left. + \frac{1}{2} (\rho^n |\vec{v}^{n+1}|^2 - \rho^{n-1} |\vec{v}^n|^2) + g x_g (\rho^{n+1} - \rho^n) \right] dV \\ &\quad + \int_{\partial \mathcal{B}_s} (\gamma_{\text{sl}} - \gamma_{\text{sv}}) (h(\rho^{n+1}) - h(\rho^n)) dA. \end{aligned} \quad (5.22)$$

For the local part of the Helmholtz free energy and the surface energy the following Taylor expansions can be used

$$\begin{aligned} \rho^{n+1} a^{\text{PeTS}}(\rho^{n+1}) - \rho^n a^{\text{PeTS}}(\rho^n) &= \frac{\partial (\rho a^{\text{PeTS}})}{\partial \rho} \Big|_{\rho^n} (\rho^{n+1} - \rho^n) \\ &+ \frac{1}{2} \frac{\partial^2 (\rho a^{\text{PeTS}})}{\partial \rho^2} \Big|_{\rho_\xi^n} (\rho^{n+1} - \rho^n)^2, \end{aligned} \quad (5.23)$$

$$\begin{aligned} h(\rho^{n+1}) - h(\rho^n) &= \frac{\partial h(\rho)}{\partial \rho} \Big|_{\rho^n} (\rho^{n+1} - \rho^n) \\ &+ \frac{1}{2} \frac{\partial^2 h(\rho)}{\partial \rho^2} \Big|_{\rho_\eta^n} (\rho^{n+1} - \rho^n)^2, \end{aligned} \quad (5.24)$$

[Shokrpour Roudbari et al. 2018] with $\rho_\xi^n, \rho_\eta^n \in [\rho^n, \rho^{n+1}]$ being a density value between ρ^n and ρ^{n+1} .

Furthermore, it holds that

$$\frac{1}{2} (|\nabla \rho^{n+1}|^2 - |\nabla \rho^n|^2) = \nabla \rho^{n+1} \cdot (\nabla \rho^{n+1} - \nabla \rho^n) - \frac{1}{2} |\nabla \rho^{n+1} - \nabla \rho^n|^2. \quad (5.25)$$

For the change of kinetic energy, the following identity can be used

$$\begin{aligned} \frac{1}{2} (\rho^n |\vec{v}^{n+1}|^2 - \rho^{n-1} |\vec{v}^n|^2) &= \frac{1}{2} (\rho^n \vec{v}^{n+1} - \rho^{n-1} \vec{v}^n) \cdot \vec{v}^{n+1} \\ &+ \frac{1}{2} \rho^{n-1} (\vec{v}^{n+1} - \vec{v}^n) \cdot \vec{v}^{n+1} \\ &- \frac{1}{2} \rho^{n-1} |\vec{v}^{n+1} - \vec{v}^n|^2. \end{aligned} \quad (5.26)$$

By setting the velocity to $\vec{v} = \vec{0}$ on all of $\partial\mathcal{B}$, it follows from (5.14)-(5.19) that

$$\begin{aligned} &\int_{\mathcal{B}} \left[\frac{1}{2} (\rho^n \vec{v}^{n+1} - \rho^{n-1} \vec{v}^n) \cdot \vec{v}^{n+1} \right. \\ &+ \frac{1}{2} \rho^{n-1} (\vec{v}^{n+1} - \vec{v}^n) \cdot \vec{v}^{n+1} \\ &\left. + (\rho^{n+1} - \rho^n) x_g g \right] dV \\ &= \int_{\mathcal{B}} \left[-\Delta t 2\eta^v(\rho^n) \left| \nabla^s \vec{v}^{n+1} - \frac{1}{3} \text{tr}(\nabla^s \vec{v}^{n+1}) \mathbf{1} \right|^2 \right. \\ &\left. - \beta^s (\rho^{n+1} - \rho^n)^2 - \frac{\partial (\rho a^{\text{PeTS}})}{\partial \rho} \Big|_{\rho^n} (\rho^{n+1} - \rho^n) \right] dV \end{aligned}$$

$$\begin{aligned}
& - \kappa |\nabla \rho^{n+1}|^2 + \kappa \nabla \rho^{n+1} \cdot \nabla \rho^n \Big] dV \\
& - \int_{\partial \mathcal{B}_s} (\gamma_{sl} - \gamma_{sv}) \left[\alpha^s (\rho^{n+1} - \rho^n) + \frac{\partial h(\rho)}{\partial \rho} \Big|_{\rho^n} \right] \\
& \quad (\rho^{n+1} - \rho^n) dA, \tag{5.27}
\end{aligned}$$

see appendix B for details.

Collecting the results above and inserting them into (5.22) yields

$$\begin{aligned}
E^{n+1} - E^n &= \int_{\mathcal{B}} \left[-\frac{1}{2} \kappa |\nabla \rho^{n+1} - \nabla \rho^n|^2 - \frac{1}{2} \rho^{n-1} |\vec{v}^{n+1} - \vec{v}^n|^2 \right. \\
& \quad - \Delta t 2 \eta^v(\rho^n) \left| \nabla^s \vec{v}^{n+1} - \frac{1}{3} \text{tr}(\nabla^s \vec{v}^{n+1}) \mathbf{1} \right|^2 \\
& \quad \left. - \left(\beta^s - \frac{1}{2} \frac{\partial^2 (\rho a^{\text{PeTS}})}{\partial \rho^2} \Big|_{\rho_\xi^n} \right) (\rho^{n+1} - \rho^n)^2 \right] dV \\
& \quad + \int_{\partial \mathcal{B}_s} - \left(\alpha^s - \frac{1}{2} \frac{\partial^2 h(\rho)}{\partial \rho^2} \Big|_{\rho_\eta^n} \right) (\gamma_{sl} - \gamma_{sv}) (\rho^{n+1} - \rho^n)^2 dA. \tag{5.28}
\end{aligned}$$

The discrete energy change in time is negative if

$$\rho^{n-1} \geq 0, \tag{5.29}$$

$$\beta^s \geq \frac{1}{2} \frac{\partial^2 (\rho a^{\text{PeTS}})}{\partial \rho^2} \Big|_{\rho_\xi^n}, \tag{5.30}$$

$$\alpha^s \begin{cases} \geq \frac{1}{2} \frac{\partial^2 h(\rho)}{\partial \rho^2} \Big|_{\rho_\eta^n} & \text{if } \gamma_{sl} > \gamma_{sv} \\ \leq \frac{1}{2} \frac{\partial^2 h(\rho)}{\partial \rho^2} \Big|_{\rho_\eta^n} & \text{if } \gamma_{sl} < \gamma_{sv} \end{cases}. \tag{5.31}$$

The requirement (5.29) can always be fulfilled. The requirements (5.30) and (5.31) cannot be fulfilled for all values of $\rho \in \mathbb{R}^{>0}$. However, the density ρ is expected to lie in between or close to ρ'' and ρ' for all time steps of the simulation. It is therefore possible to find suitable choices for β^s and α^s such that (5.30) and (5.31) are not violated.

Suitable Choices for the Stabilization Parameters

The following demonstrates how suitable choices for the stabilization parameters β^s and α^s can be found. In this example, the temperature is assumed to be $T = 0.7 \frac{\epsilon^{\text{LJ}}}{k_B}$. However, suitable values for β^s and α^s can also be found for different temperatures. Plots of the second derivatives of the local part of the Helmholtz free energy per volume ρa^{PeTS} and the interpolation function $h(\rho)$ for $T = 0.7 \frac{\epsilon^{\text{LJ}}}{k_B}$ are shown in Figure 5.3.

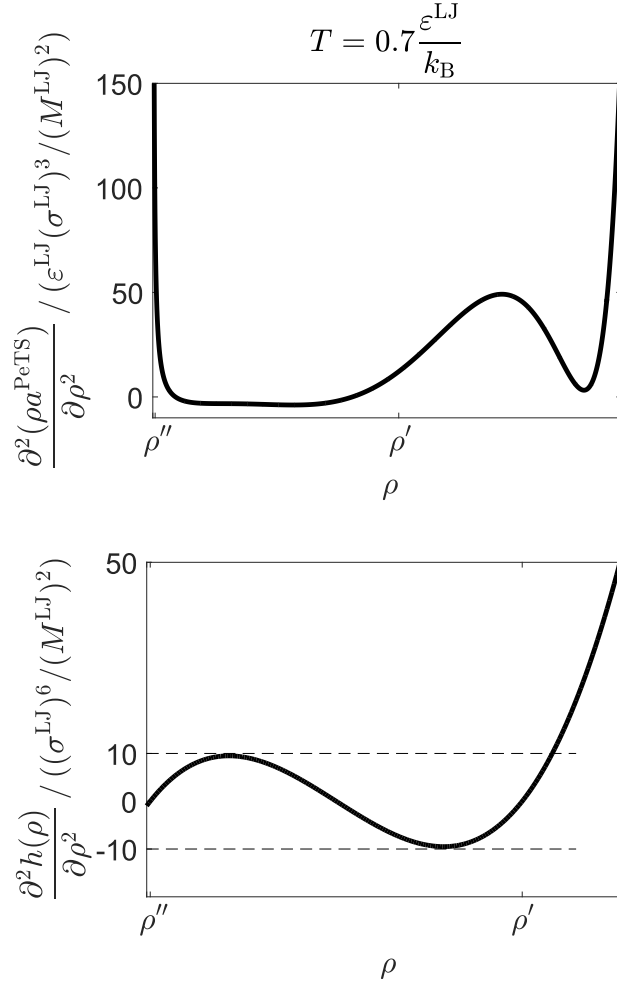


Figure 5.3: Plots of the second derivatives of the local part of the Helmholtz free energy per volume ρa^{PeTS} (top) and the interpolation function $h(\rho)$ (bottom) at $T = 0.7 \frac{\epsilon^{\text{LJ}}}{k_B}$. [Diewald et al. 2020b]

The value of the second derivative of the local part of the Helmholtz free energy per volume for the density range between the vapor bulk density ρ'' and the liquid

bulk density ρ' is highest at the vapor bulk density $\frac{\partial^2(\rho a^{\text{PeTS}})}{\partial \rho^2}|_{\rho''} \approx 83 \frac{\epsilon^{\text{LJ}}(\sigma^{\text{LJ}})^3}{(M^{\text{LJ}})^2}$, cf. Figure 5.3 (top). It is suggestive to use $\beta^s = 50 \frac{\epsilon^{\text{LJ}}(\sigma^{\text{LJ}})^3}{(M^{\text{LJ}})^2}$ as this choice satisfies (5.30) for density values between ρ'' and ρ' as well as for densities that are outside but close to this range.

The value of the second derivative of the interpolation function for the density range between the vapor bulk density ρ'' and the liquid bulk density ρ' is never smaller than $-10 \frac{(\sigma^{\text{LJ}})^6}{(M^{\text{LJ}})^2}$ or higher than $10 \frac{(\sigma^{\text{LJ}})^6}{(M^{\text{LJ}})^2}$, cf. Figure 5.3 (bottom). It is suggestive to use $\alpha^s = -5 \frac{(\sigma^{\text{LJ}})^6}{(M^{\text{LJ}})^2}$ if $\gamma_{\text{sl}} < \gamma_{\text{sv}}$ and $\alpha^s = 5 \frac{(\sigma^{\text{LJ}})^6}{(M^{\text{LJ}})^2}$ if $\gamma_{\text{sl}} > \gamma_{\text{sv}}$. In the case of $\gamma_{\text{sl}} < \gamma_{\text{sv}}$, the requirement (5.31) can never be violated. In the case of $\gamma_{\text{sl}} > \gamma_{\text{sv}}$ the requirement (5.31) is not violated if the density is not much higher than ρ' .

5.2 Weak Form and Spatial Discretization

The FE method is used for the spatial discretization. Thus, this section presents the information that is needed to use the dynamic Navier-Stokes-Korteweg and the static Allen-Cahn model in an FE framework. However, the FE method is not discussed here in full detail. For further reading see e.g. [Wriggers 2001; Zienkiewicz and Taylor 2006] which give the basis for this section.

For ease of visualization the following elaborations are written down for the two-dimensional case. An extension to the third dimension is straightforward. The domain \mathcal{B} is discretized into n_e finite elements \mathcal{B}_e which represent an approximation of the domain \mathcal{B} and its boundary $\partial\mathcal{B}$,

$$\mathcal{B} \approx \bigcup_{e=1}^{n_e} \mathcal{B}_e \quad \text{and} \quad \partial\mathcal{B} \approx \bigcup_{e=1}^{n_b} \partial\mathcal{B}_e, \quad (5.32)$$

with $\partial\mathcal{B}_e$ representing the n_b edges on the boundary. A sketch of the discretization is given in Figure 5.4.

Physical quantities are stored at the nodes of the finite elements, only. To compute the value of a physical quantity $\mathcal{A}_e(\vec{x})$ within a finite element the node values \mathcal{A}_I are interpolated with the help of shape functions $N_I(\vec{x})$,

$$\mathcal{A}(\vec{x}) \approx \mathcal{A}_e(\vec{x}) = \sum_{I=1}^{n_n} N_I(\vec{x}) \mathcal{A}_I. \quad (5.33)$$

In this, n_n is the number of nodes per element. Thus, spatial derivatives are

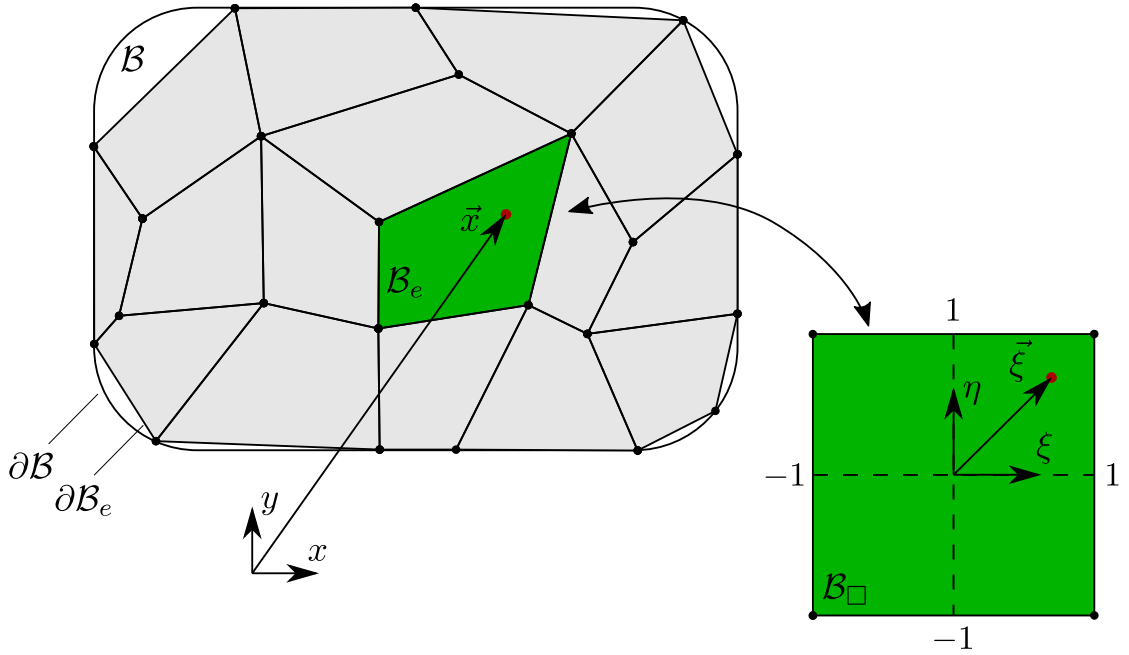


Figure 5.4: The domain \mathcal{B} is discretized with finite elements \mathcal{B}_e . The reference element \mathcal{B}_\square represents a finite element in natural coordinates with $\xi \in [-1, 1]$ and $\eta \in [-1, 1]$.

approximated by

$$\frac{\partial \mathcal{A}_e(\vec{x})}{\partial x} = \sum_{I=1}^{n_n} \frac{\partial N_I(\vec{x})}{\partial x} \mathcal{A}_I \quad \text{and} \quad \frac{\partial \mathcal{A}_e(\vec{x})}{\partial y} = \sum_{I=1}^{n_n} \frac{\partial N_I(\vec{x})}{\partial y} \mathcal{A}_I. \quad (5.34)$$

Following the isoparametric concept, the same shape functions are used for the approximation of the physical quantities and the representation of the element geometry,

$$\vec{x} = \sum_{I=1}^{n_n} N_I(\vec{\xi}) \vec{x}_I. \quad (5.35)$$

To simplify the numerical implementation, the shape functions are defined with respect to the natural coordinates ξ and η of a reference element \mathcal{B}_\square , cf. Figure 5.4. This reference element is obtained by a transformation of the finite element \mathcal{B}_e in physical coordinates to its representation in natural coordinates with $\xi \in [-1, 1]$ and $\eta \in [-1, 1]$. The spatial position within the reference element is denoted by $\vec{\xi}$. The spatial position within an element in physical coordinates can be expressed in terms of $\vec{\xi}$ and therefore $\vec{x} = \vec{x}(\vec{\xi})$.

With the above, the spatial derivatives with respect to the physical coordinates, cf. (5.34), can be expressed in terms of the natural coordinates. This is done by considering the following relations,

$$\frac{\partial \mathcal{A}_e}{\partial \xi} = \frac{\partial \mathcal{A}_e}{\partial x} \frac{\partial x}{\partial \xi} + \frac{\partial \mathcal{A}_e}{\partial y} \frac{\partial y}{\partial \xi}, \quad (5.36)$$

$$\frac{\partial \mathcal{A}_e}{\partial \eta} = \frac{\partial \mathcal{A}_e}{\partial x} \frac{\partial x}{\partial \eta} + \frac{\partial \mathcal{A}_e}{\partial y} \frac{\partial y}{\partial \eta}, \quad (5.37)$$

or

$$\begin{bmatrix} \frac{\partial \mathcal{A}_e}{\partial \xi} \\ \frac{\partial \mathcal{A}_e}{\partial \eta} \end{bmatrix} = \underbrace{\begin{bmatrix} \frac{\partial x}{\partial \xi} & \frac{\partial y}{\partial \xi} \\ \frac{\partial x}{\partial \eta} & \frac{\partial y}{\partial \eta} \end{bmatrix}}_{\mathbf{J}} \begin{bmatrix} \frac{\partial \mathcal{A}_e}{\partial x} \\ \frac{\partial \mathcal{A}_e}{\partial y} \end{bmatrix} \quad \text{and thus} \quad \begin{bmatrix} \frac{\partial \mathcal{A}_e}{\partial x} \\ \frac{\partial \mathcal{A}_e}{\partial y} \end{bmatrix} = \mathbf{J}^{-1} \begin{bmatrix} \frac{\partial \mathcal{A}_e}{\partial \xi} \\ \frac{\partial \mathcal{A}_e}{\partial \eta} \end{bmatrix}. \quad (5.38)$$

The Jacobian matrix \mathbf{J} can be computed by using the approximation of the element geometry (5.35),

$$\mathbf{J} = \sum_{I=1}^{n_n} \begin{bmatrix} \frac{\partial N_I(\vec{\xi})}{\partial \xi} x_I & \frac{\partial N_I(\vec{\xi})}{\partial \xi} y_I \\ \frac{\partial N_I(\vec{\xi})}{\partial \eta} x_I & \frac{\partial N_I(\vec{\xi})}{\partial \eta} y_I \end{bmatrix}. \quad (5.39)$$

The equations of the dynamic Navier-Stokes-Korteweg model and the static Allen-Cahn model shall only be fulfilled in their weak form, cf. next sections. It is therefore necessary to evaluate integrals of the form

$$\int_{\mathcal{B}_e} G(\vec{x}) \, dV \quad (5.40)$$

over the finite elements. Here, G is a function of \vec{x} . The integrals shall be evaluated numerically by Gaussian quadrature. The quadrature points and weights are typically given for the integration interval $[-1, 1]$. It is therefore beneficial to transform the integrals over \mathcal{B}_e to integrals over \mathcal{B}_\square first and to apply the quadrature rule second. The transformation can easily be achieved with $\det \mathbf{J}$ as the determinant of the Jacobian matrix,

$$\int_{\mathcal{B}_e} G(\vec{x}) \, dV = \int_{\mathcal{B}_\square} G(\vec{\xi}) \det \mathbf{J} \, d\Box = \int_{-1}^1 \int_{-1}^1 G(\vec{\xi}) \det \mathbf{J} \, d\xi \, d\eta. \quad (5.41)$$

Approximating the integral by means of Gaussian quadrature yields

$$\int_{-1}^1 \int_{-1}^1 G(\vec{\xi}) \det \mathbf{J} \, d\xi \, d\eta \approx \sum_{p=1}^{n_p} G(\vec{\xi}_p) \det \mathbf{J}(\vec{\xi}_p) w_p \quad (5.42)$$

with n_p , $\vec{\xi}_p$, and w_p denoting the total number, position, and weights of the quadrature points. For specific values see e.g. [Wriggers 2001].

With the elaborations above it is evident that the FE method introduces several approximations:

1. The domain \mathcal{B} is approximated by finite elements.
2. Physical quantities within these finite elements are approximated by means of interpolation.
3. Integrals over the finite elements are approximated by numerical quadrature.

In the following sections the FE method is applied to the dynamic Navier-Stokes-Korteweg model and the static Allen-Cahn model. Firstly, the weak forms of the underlying equations are derived. Subsequently, the discretization discussed above is applied.

5.2.1 Dynamic Navier-Stokes-Korteweg Model

The weak form of the dynamic Navier-Stokes-Korteweg model is obtained by multiplying the mass balance, the momentum balance, and the equation for the chemical potential with the test functions $\delta\rho$, $\delta\vec{v}$, $\delta\mu$, respectively, and integrating each equation over the domain \mathcal{B} ,

$$\int_{\mathcal{B}} \left[\frac{\partial \rho}{\partial t} + \operatorname{div}(\rho \vec{v}) \right] \delta\rho \, dV = 0, \quad (5.43)$$

$$\int_{\mathcal{B}} \left[\rho \frac{\partial \vec{v}}{\partial t} + \rho \nabla \vec{v} \vec{v} - \operatorname{div} \boldsymbol{\sigma} + \rho g \vec{e}_g \right] \cdot \delta\vec{v} \, dV = 0, \quad (5.44)$$

$$\int_{\mathcal{B}} \left[\mu - \frac{\partial(\rho \hat{\psi})}{\partial \rho} + \operatorname{div} \frac{\partial(\rho \hat{\psi})}{\partial \nabla \rho} \right] \delta\mu \, dV = 0. \quad (5.45)$$

The equations above represent the form of the dynamic Navier-Stokes-Korteweg model as it is used for the backward Euler time integration scheme. The procedure can analogously be applied for the form of the model as it is used for the semi-implicit energy time integration scheme. The superscript $n + 1$ is omitted.

The expression for the chemical potential could also be used in the momentum balance, where μ is needed in the constitutive equation. However, this would lead to a weak form that includes second order spatial derivatives making the FE implementation less straightforward and adding restrictions on the possible choices for the shape functions.

Invoking integration by parts, inserting the boundary conditions and applying Cauchy's theorem yields

$$\int_{\mathcal{B}} \left[\frac{\partial \rho}{\partial t} + \operatorname{div}(\rho \vec{v}) \right] \delta \rho \, dV = 0, \quad (5.46)$$

$$\begin{aligned} & \int_{\mathcal{B}} \left[\left(\rho \frac{\partial \vec{v}}{\partial t} + \rho \nabla \vec{v} \vec{v} + \rho g \vec{e}_g \right) \cdot \delta \vec{v} + \boldsymbol{\sigma} : \nabla \delta \vec{v} \right] dV \\ & - \int_{\partial \mathcal{B} \setminus \partial \mathcal{B}_s} \vec{t} \cdot \delta \vec{v} \, dA = 0, \end{aligned} \quad (5.47)$$

$$\begin{aligned} & \int_{\mathcal{B}} \left[\left(\mu - \frac{\partial(\rho \hat{\psi})}{\partial \rho} \right) \delta \mu - \frac{\partial(\rho \hat{\psi})}{\partial \nabla \rho} \cdot \nabla \delta \mu \right] dV \\ & - \int_{\partial \mathcal{B} \cap \partial \mathcal{B}_s} \frac{\partial(\rho \hat{\phi})}{\partial \rho} \delta \mu \, dA = 0. \end{aligned} \quad (5.48)$$

Note that the test functions are zero at the part of the boundary that is given by a Dirichlet boundary condition for the respective degree of freedom.

For the physical quantities and the test functions the aforementioned discretizations on element level are used,

$$\begin{aligned} \rho_e &= \sum_{I=1}^{n_n} N_I^\rho \rho_I, & \vec{v}_e &= \sum_{I=1}^{n_n} N_I^{\vec{v}} \vec{v}_I, & \mu_e &= \sum_{I=1}^{n_n} N_I^\mu \mu_I, \\ \nabla \rho_e &= \sum_{I=1}^{n_n} \mathbf{B}_I^\rho \rho_I, & \nabla \vec{v}_e &= \sum_{I=1}^{n_n} \mathbf{B}_I^{\vec{v}} \vec{v}_I, & \nabla \mu_e &= \sum_{I=1}^{n_n} \mathbf{B}_I^\mu \mu_I, \\ \delta \rho_e &= \sum_{I=1}^{n_n} N_I^\rho \delta \rho_I, & \delta \vec{v}_e &= \sum_{I=1}^{n_n} N_I^{\vec{v}} \delta \vec{v}_I, & \delta \mu_e &= \sum_{I=1}^{n_n} N_I^\mu \delta \mu_I, \\ \nabla \delta \rho_e &= \sum_{I=1}^{n_n} \mathbf{B}_I^\rho \delta \rho_I, & \nabla \delta \vec{v}_e &= \sum_{I=1}^{n_n} \mathbf{B}_I^{\vec{v}} \delta \vec{v}_I, & \nabla \delta \mu_e &= \sum_{I=1}^{n_n} \mathbf{B}_I^\mu \delta \mu_I, \end{aligned} \quad (5.49)$$

with

$$\mathbf{B}^\rho = \begin{bmatrix} \frac{\partial N_I^\rho}{\partial x} \\ \frac{\partial N_I^\rho}{\partial y} \end{bmatrix}, \quad \mathbf{B}^{\vec{v}} = \begin{bmatrix} \frac{\partial N_I^{\vec{v}}}{\partial x} & 0 \\ 0 & \frac{\partial N_I^{\vec{v}}}{\partial y} \\ \frac{\partial N_I^{\vec{v}}}{\partial y} & \frac{\partial N_I^{\vec{v}}}{\partial x} \end{bmatrix}, \quad \text{and} \quad \mathbf{B}^\mu = \begin{bmatrix} \frac{\partial N_I^\mu}{\partial x} \\ \frac{\partial N_I^\mu}{\partial y} \end{bmatrix}. \quad (5.50)$$

The form of $\mathbf{B}^{\vec{v}}$ leads to a representation of $\nabla \vec{v}_e$, $\nabla \delta \vec{v}_e$, and $\boldsymbol{\sigma}$ in Voigt notation,

$$\nabla \vec{v}_e = \begin{bmatrix} (\nabla \vec{v}_e)_{xx} \\ (\nabla \vec{v}_e)_{yy} \\ (\nabla \vec{v}_e)_{xy} + (\nabla \vec{v}_e)_{yx} \end{bmatrix}, \quad \nabla \delta \vec{v}_e = \begin{bmatrix} (\nabla \delta \vec{v}_e)_{xx} \\ (\nabla \delta \vec{v}_e)_{yy} \\ (\nabla \delta \vec{v}_e)_{xy} + (\nabla \delta \vec{v}_e)_{yx} \end{bmatrix}, \quad (5.51)$$

and

$$\boldsymbol{\sigma} = [\sigma_{xx} \quad \sigma_{yy} \quad \sigma_{xy}]^T. \quad (5.52)$$

Due to the symmetry of $\boldsymbol{\sigma}$, the loss of the information on the asymmetry of $\nabla \delta \vec{v}_e$ has no effect, cf. (5.47). The discretized versions of (5.46), (5.47) and (5.48) can now be stated. They read

$$\bigcup_{e=1}^{n_e} \sum_{I=1}^{n_n} \delta \rho_I R_I^\rho = 0, \quad (5.53)$$

$$\bigcup_{e=1}^{n_e} \sum_{I=1}^{n_n} \delta \vec{v}_I^T \vec{R}_I^{\vec{v}} = 0, \quad (5.54)$$

$$\bigcup_{e=1}^{n_e} \sum_{I=1}^{n_n} \delta \mu_I R_I^\mu = 0, \quad (5.55)$$

with

$$R_I^\rho = \int_{\mathcal{B}_e} N_I^\rho \left[\frac{\partial \rho}{\partial t} + \text{div}(\rho \vec{v}) \right] dV, \quad (5.56)$$

$$\vec{R}_I^{\vec{v}} = \int_{\mathcal{B}_e} \left[N_I^{\vec{v}} \left(\rho \frac{\partial \vec{v}}{\partial t} + \rho \nabla \vec{v} \vec{v} + \rho g \vec{e}_g \right) + (\mathbf{B}_I^{\vec{v}})^T \boldsymbol{\sigma} \right] dV - \int_{\partial \mathcal{B}_e \setminus \partial \mathcal{B}_s} N_I^{\vec{v}} \vec{t} dA, \quad (5.57)$$

$$R_I^\mu = \int_{\mathcal{B}_e} \left[N_I^\mu \left(\mu - \frac{\partial(\rho \hat{\psi})}{\partial \rho} \right) - (\mathbf{B}_I^\mu)^T \frac{\partial(\rho \hat{\psi})}{\partial \nabla \rho} \right] dV - \int_{\partial \mathcal{B}_e \cap \partial \mathcal{B}_s} N_I^\mu \frac{\partial(\rho \hat{\phi})}{\partial \rho} dA. \quad (5.58)$$

Assembling the nodal residuals R_I^ρ , $\vec{R}_I^{\vec{v}}$, and R_I^μ yields the global residual vector

$$\vec{R} = \bigcup_{e=1}^{n_e} \vec{R}_I \quad \text{with} \quad \vec{R}_I = [R_I^\rho \quad (\vec{R}_I^{\vec{v}})^T \quad R_I^\mu]^T \quad (5.59)$$

as the nodal residual vector. This expression should be read as: “For each global node, build the sum of the contributions from all nodal residual vectors, i.e. the nodal contributions from all elements that are connected to this node. Subsequently arrange the resulting vectors below each other.”

In order to find the nodal values of ρ , \vec{v} , and μ that solve (5.53), (5.54), and (5.55) for the next time step $n + 1$, the residuals are linearized and the Newton-Raphson method, cf. section 5.1, is applied. This yields the following system of equations on element level,

$$\sum_{J=1}^{n_n} \left(\begin{bmatrix} S_{IJ}^{\rho\rho} & \vec{S}_{IJ}^{\rho\vec{v}} & 0 \\ \vec{S}_{IJ}^{\vec{v}\rho} & \mathbf{S}_{IJ}^{\vec{v}\vec{v}} & \vec{S}_{IJ}^{\vec{v}\mu} \\ S_{IJ}^{\mu\rho} & \vec{0} & S_{IJ}^{\mu\mu} \end{bmatrix} \begin{bmatrix} \Delta\rho_J \\ \Delta\vec{v}_J \\ \Delta\mu_J \end{bmatrix} \right) = \begin{bmatrix} -R_I^\rho \\ -\vec{R}_I^{\vec{v}} \\ -R_I^\mu \end{bmatrix}. \quad (5.60)$$

The submatrices S_{IJ}^{ab} with $a, b \in \{\rho, \vec{v}, \mu\}$ are given by the derivative of the nodal residual for the degree of freedom a and node I with respect to the value of the degree of freedom b at node J ,

$$\begin{aligned} S_{IJ}^{ab} &= \frac{\partial R_I^a}{\partial b_J} \\ &= \frac{\partial R_I^a}{\partial b} \frac{\partial b}{\partial b_J} + \frac{\partial R_I^a}{\partial \nabla b} \frac{\partial \nabla b}{\partial b_J} + \frac{\partial R_I^a}{\partial \left(\frac{\partial b}{\partial t}\right)} \frac{\partial \left(\frac{\partial b}{\partial t}\right)}{\partial \left(\frac{\partial b}{\partial t}\right)_J} \frac{\partial \left(\frac{\partial b}{\partial t}\right)_J}{\partial b_J} \\ &= \frac{\partial R_I^a}{\partial b} N_J^b + \frac{\partial R_I^a}{\partial \nabla b} \mathbf{B}_J^b + \frac{\partial R_I^a}{\partial \left(\frac{\partial b}{\partial t}\right)} N_J^b c^{\text{tint}}. \end{aligned} \quad (5.61)$$

In this, c^{tint} is a scalar quantity that depends on the choice of the time integration scheme as well as the time step size Δt . For the backward Euler time integration scheme, it is given by

$$c^{\text{tint}} = \frac{\partial \left(\frac{\partial b}{\partial t}\right)_J}{\partial b_J} = \frac{1}{\Delta t}, \quad (5.62)$$

cf. (5.1).

The submatrices S_{IJ}^{ab} can be split into stiffness submatrices K_{IJ}^{ab} and damping submatrices D_{IJ}^{ab} ,

$$S_{IJ}^{ab} = K_{IJ}^{ab} + D_{IJ}^{ab} c^{\text{tint}}, \quad (5.63)$$

with

$$K_{IJ}^{ab} = \frac{\partial R_I^a}{\partial b} N_J^b + \frac{\partial R_I^a}{\partial \nabla b} \mathbf{B}_J^b \quad \text{and} \quad D_{IJ}^{ab} = \frac{\partial R_I^a}{\partial \left(\frac{\partial b}{\partial t}\right)} N_J^b. \quad (5.64)$$

Note that for $\vec{S}_{IJ}^{\rho\vec{v}}$ and $\mathbf{S}_{IJ}^{\vec{v}\vec{v}}$ the terms “stiffness” and “damping” matrix deviate from the way they are commonly used in continuum mechanics. Since the velocity itself (and not the displacement) is chosen as a degree of freedom, the stiffness and damping matrix represent derivatives with respect to velocity and acceleration (and not displacement and velocity), respectively.

Evaluating (5.60) for each nodal residual vector and assembling the corresponding systems of equations yields the global system of equations

$$\mathbf{S} \Delta \vec{u} = (\mathbf{K} + \mathbf{D} c^{\text{tint}}) \Delta \vec{u} = -\vec{R}. \quad (5.65)$$

In this, \mathbf{S} is the asymmetric system matrix. The matrices \mathbf{K} and \mathbf{D} represent the global stiffness and damping matrices. The global degree of freedom vector is denoted by \vec{u} . Solving the global system of equations corresponds to step 2. of the Newton-Raphson method on page 57.

Up to now, no choices for the explicit form of the shape functions N_I^ρ , $N_I^{\vec{v}}$, and N_I^μ that are used to interpolate between the node values ρ_I , \vec{v}_I , and μ_I have been made. In the present work, a Q2P1 formulation is utilized, i.e. quadratic shape functions are used for the velocity and linear shape functions are used for the density and the chemical potential. In the two-dimensional case, this leads to 9 nodes for the velocity and 4 nodes for the density and the chemical potential on each element. In the three-dimensional case there are 27 nodes for the velocity and 8 nodes for the density and the chemical potential on each element. Figure 5.5 shows a sketch of the discretization for the two-dimensional case. Additional line elements in the two-dimensional case or surface elements in the three-dimensional case are used for the contributions on $\partial \mathcal{B}_e \cap \partial \mathcal{B}_s$, cf. (5.58) and Figure 5.5.

For flow problems with only one phase a Q2P1 formulation with quadratic shape functions for the velocity and linear shape functions for the pressure satisfies the inf-sup condition, also known as Babüska-Brezzi condition, [Brezzi and Fortin 1991]. It is not clear if the Q2P1 formulation for flow problems with more than one phase as it is used in this work (quadratic velocity, linear density and chemical potential) does also satisfy the inf-sup condition. However, the numerical examples in section 6.3 demonstrate that it proves to be applicable.

5.2.2 Static Allen-Cahn Model

The weak form of the static Allen-Cahn model is obtained by multiplying (3.68) and (3.69) with the test functions $\delta\rho$, $\delta\lambda$, respectively, and integrating the former

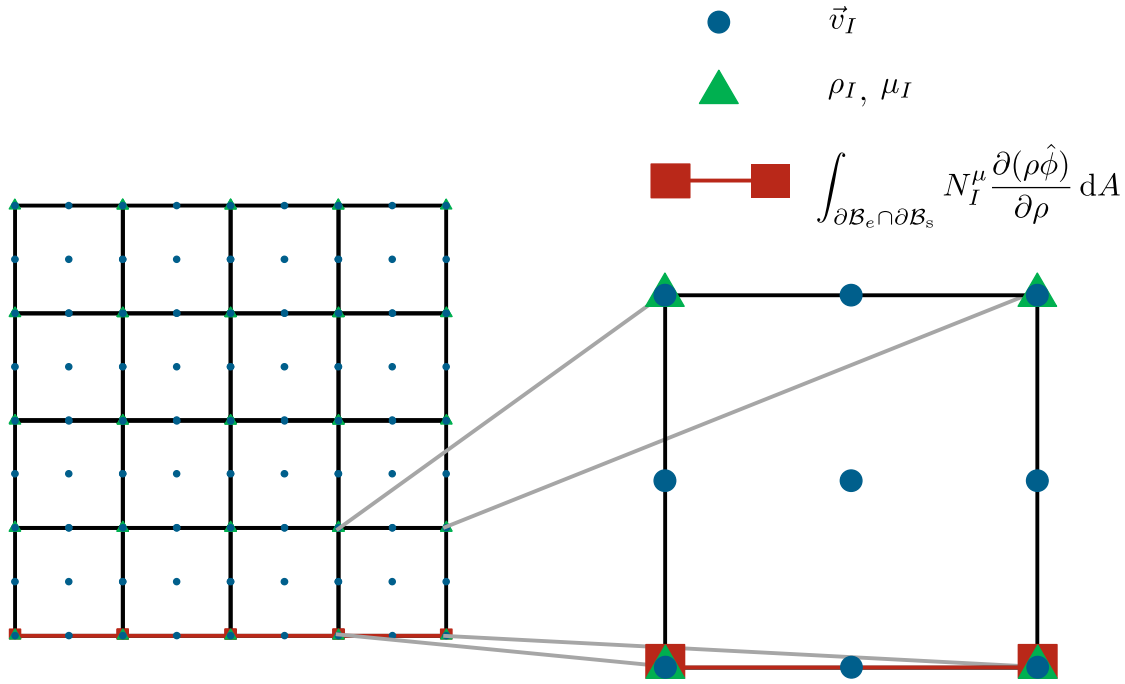


Figure 5.5: Sketch of the discretization for the dynamic Navier-Stokes-Korteweg model for two-dimensional scenarios (Q2P1). The contributions on $\partial\mathcal{B}_e \cap \partial\mathcal{B}_s$ are addressed by additional line elements.

over the domain \mathcal{B}

$$\int_{\mathcal{B}} \left[\frac{\partial(\rho\hat{\psi})}{\partial\rho} - \operatorname{div} \frac{\partial(\rho\hat{\psi})}{\partial\nabla\rho} + gx_g + \lambda + \frac{1}{M} \frac{\partial\rho}{\partial t} \right] \delta\rho dV = 0 \quad (5.66)$$

$$\left(\int_{\mathcal{B}} \rho dV - m_{\mathcal{B}} \right) \delta\lambda = 0. \quad (5.67)$$

Invoking integration by parts and inserting the boundary conditions yields

$$\int_{\mathcal{B}} \left[\left(\frac{\partial(\rho\hat{\psi})}{\partial\rho} + gx_g + \lambda + \frac{1}{M} \frac{\partial\rho}{\partial t} \right) \delta\rho + \frac{\partial(\rho\hat{\psi})}{\partial\nabla\rho} \cdot \nabla\delta\rho \right] dV + \int_{\partial\mathcal{B} \cap \partial\mathcal{B}_s} \frac{\partial(\rho\hat{\phi})}{\partial\rho} \delta\rho dA = 0 \quad (5.68)$$

$$\left(\int_{\mathcal{B}} \rho dV - m_{\mathcal{B}} \right) \delta\lambda = 0. \quad (5.69)$$

The degree of freedom λ is a global degree of freedom, i.e. only one value for the entire domain \mathcal{B} exists. The discretized versions of (5.68) and (5.69) read

$$\bigcup_{e=1}^{n_e} \sum_{I=1}^{n_n} \delta \rho_I R_I^\rho = 0, \quad (5.70)$$

$$\delta \lambda R^\lambda = 0 \quad (5.71)$$

with

$$\begin{aligned} R_I^\rho &= \int_{\mathcal{B}_e} \left[N_I^\rho \left(\frac{\partial(\rho \hat{\psi})}{\partial \rho} + g x_g + \lambda + \frac{1}{M} \frac{\partial \rho}{\partial t} \right) + (\mathbf{B}_I^\rho)^\top \frac{\partial(\rho \hat{\psi})}{\partial \nabla \rho} \right] dV \\ &\quad + \int_{\partial \mathcal{B}_e \cap \partial \mathcal{B}_s} N_I^\rho \frac{\partial(\rho \hat{\phi})}{\partial \rho} dA, \end{aligned} \quad (5.72)$$

$$R^\lambda = \left(\bigcup_{e=1}^{n_e} \int_{\mathcal{B}_e} \rho dV - m_{\mathcal{B}} \right) \delta \lambda \quad (5.73)$$

as the nodal residual for ρ and the residual for λ .

Analogously to section 5.2.1, the linearization of the residuals leads to the global system of equations

$$\underbrace{\begin{bmatrix} \mathbf{S}^{\rho\rho} & \vec{S}^{\rho\lambda} \\ \vec{S}^{\lambda\rho} & 0 \end{bmatrix}}_{\mathbf{S}} \begin{bmatrix} \Delta \vec{\rho} \\ \Delta \lambda \end{bmatrix} = \begin{bmatrix} -\vec{R}^\rho \\ -R^\lambda \end{bmatrix}. \quad (5.74)$$

In this, \mathbf{S} is the symmetric system matrix, $\vec{\rho}$ is the global degree of freedom vector for ρ , and

$$\vec{R}^\rho = \bigcup_{e=1}^{n_e} R_I^\rho \quad (5.75)$$

denotes the global residual vector for ρ . The submatrices of the system matrix can be written on element level as

$$S_{IJ}^{\rho\rho} = K_{IJ}^{\rho\rho} + D_{IJ}^{\rho\rho} c^{\text{tint}}, \quad (5.76)$$

$$S_J^{\lambda\rho} = \left(S_I^{\rho\lambda} \right)^\top = K_J^{\lambda\rho} \quad (5.77)$$

with the stiffness and damping submatrices

$$K_{IJ}^{\rho\rho} = \int_{\mathcal{B}_e} \left[N_I^\rho \frac{\partial^2(\rho\hat{\psi})}{\partial\rho^2} N_J^\rho + (\mathbf{B}_I^\rho)^\top \frac{\partial^2(\rho\hat{\psi})}{\partial\nabla\rho^2} \mathbf{B}_J^\rho \right] dV + \int_{\partial\mathcal{B}_e \cap \partial\mathcal{B}_s} N_I^\rho \frac{\partial^2(\rho\hat{\phi})}{\partial\rho^2} N_J^\rho dA, \quad (5.78)$$

$$D_{IJ}^{\rho\rho} = \int_{\mathcal{B}_e} N_I^\rho \frac{1}{M} N_J^\rho dV, \quad (5.79)$$

$$K_J^{\lambda\rho} = \int_{\mathcal{B}_e} N_J^\rho dV. \quad (5.80)$$

Linear shape functions are chosen for the density. Analogously to the dynamic Navier-Stokes-Korteweg model, additional line elements in the two-dimensional case or surface elements in the three-dimensional case are used for the contributions on $\partial\mathcal{B}_e \cap \partial\mathcal{B}_s$.

The conservation of mass leads to one global equation, only, cf. (5.74). As can be seen in (5.73) and (5.80), this global equation is build up by contributions that have to be computed on element level. For the implementation, it is therefore necessary to be able to address the global equation on element level.

As a side note it shall be mentioned that in the expression for R^λ of the model with the empirical Helmholtz free energy the density $\rho = \rho(\varphi)$ is not just computed using (4.2), but the interpolation $\rho(\varphi) = (\rho' - \rho'')h(\varphi) + \rho''$ is used, instead.

5.3 Hyper-Dual Numbers

The evaluation of the residual vector and the system matrix requires the calculation of first and second derivatives of the Helmholtz free energy density $\rho\hat{\psi}$, see e.g. (5.72) and (5.78). In the case of the EoS based Helmholtz free energy, the function $\rho\hat{\psi}$ is a very evolved formula and has a high level of complexity. Its explicit differentiation is therefore time consuming and prone to errors. The concept of hyper-dual numbers, as presented in [Fike and Alonso 2011; Fike 2013], is used to automatically compute the exact values of the first and second derivatives without an explicit differentiation. The application of the concept of hyper-dual numbers to the EoS based Helmholtz free energy is shown in [Diewald et al. 2018a], which is the basis for this section.

Hyper-dual numbers enable the calculation of exact and step-size independent first and second derivatives. They represent an extension of the concept of complex step first derivative approximations. A hyper-dual number x_{hd} consists of one real value x_0 and three imaginary values, x_1 , x_2 , x_{12} ,

$$x_{\text{hd}} = x_0 + \epsilon_1 x_1 + \epsilon_2 x_2 + \epsilon_1 \epsilon_2 x_{12}. \quad (5.81)$$

The imaginary units ϵ_1 and ϵ_2 have the properties

$$\epsilon_1^2 = \epsilon_2^2 = (\epsilon_1 \epsilon_2)^2 = 0, \quad (5.82)$$

and

$$\epsilon_1 \neq \epsilon_2 \neq \epsilon_1 \epsilon_2 \neq 0. \quad (5.83)$$

The advantage of these properties becomes evident when developing the Taylor series of a function $G(x_{\text{hd}})$ at the position of the real value \bar{x}_0 . Evaluating the Taylor series at the position $\bar{x}_{\text{hd}} = \bar{x}_0 + \epsilon_1 h_1 + \epsilon_2 h_2 + \epsilon_1 \epsilon_2 0$, in which h_1 and h_2 are arbitrary constants, yields

$$\begin{aligned} G(\bar{x}_{\text{hd}}) &= G(\bar{x}_0 + \epsilon_1 h_1 + \epsilon_2 h_2) = G(\bar{x}_0) \\ &+ \left. \frac{dG}{dx_{\text{hd}}} \right|_{x_{\text{hd}}=\bar{x}_0} (\epsilon_1 h_1 + \epsilon_2 h_2) \\ &+ \left. \frac{d^2G}{dx_{\text{hd}}^2} \right|_{x_{\text{hd}}=\bar{x}_0} \epsilon_1 \epsilon_2 h_1 h_2. \end{aligned} \quad (5.84)$$

All terms of higher order vanish in the Taylor series due to (5.82). Therefore, (5.84) is the complete Taylor series. The exact values of the derivatives can be obtained from the imaginary parts of $G(\bar{x}_{\text{hd}})$ as

$$\left. \frac{\partial G}{\partial x_0} \right|_{x_0=\bar{x}_0} = \left. \frac{dG}{dx_{\text{hd}}} \right|_{x_{\text{hd}}=\bar{x}_0} = \frac{\text{Im}_{\epsilon_1} G(\bar{x}_{\text{hd}})}{h_1} = \frac{\text{Im}_{\epsilon_2} G(\bar{x}_{\text{hd}})}{h_2} \quad \text{and} \quad (5.85)$$

$$\left. \frac{\partial^2 G}{\partial x_0^2} \right|_{x_0=\bar{x}_0} = \left. \frac{d^2G}{dx_{\text{hd}}^2} \right|_{x_{\text{hd}}=\bar{x}_0} = \frac{\text{Im}_{\epsilon_1 \epsilon_2} G(\bar{x}_{\text{hd}})}{h_1 h_2}. \quad (5.86)$$

For the implementation of the models using the EoS based Helmholtz free energy a subprogram is used in order to compute the values of

$$\left. \frac{\partial(\rho \hat{\psi}(\rho, \nabla \rho))}{\partial \rho} \right|_{\rho=\rho(\vec{\xi}_p)} = \left. \frac{\partial(\rho a^{\text{PeTS}}(\rho))}{\partial \rho} \right|_{\rho=\rho(\vec{\xi}_p)} \quad (5.87)$$

and

$$\left. \frac{\partial^2(\rho\hat{\psi}(\rho, \nabla\rho))}{\partial\rho^2} \right|_{\rho=\rho(\vec{\xi}_p)} = \left. \frac{\partial^2(\rho a^{\text{PeTS}}(\rho))}{\partial\rho^2} \right|_{\rho=\rho(\vec{\xi}_p)} \quad (5.88)$$

at each quadrature point $\vec{\xi}_p$. The subprogram, which is written in Fortran, uses operator overloading, implemented by Becker [2015], to extend the mathematical operations to the new variable class of hyper-dual numbers. The subprogram contains the explicit expression for $\rho a^{\text{PeTS}}(\rho)$ but not for its derivatives. As it is demonstrated above, the values of the derivatives (5.87) and (5.88) can be obtained by simply calling the subprogram with $\bar{\rho}_{\text{hd}} = \rho(\vec{\xi}_p) + \epsilon_1 h_1 + \epsilon_2 h_2 + \epsilon_1 \epsilon_2 0$, cf. Figure 5.6. This implementation allows the exchange of the EoS, and thereby of the fluid under consideration, in a fast and straightforward manner. The expression for $\rho a^{\text{PeTS}}(\rho)$ needs to be changed in the subprogram, only, without having to derive the analytic expressions for its derivatives.

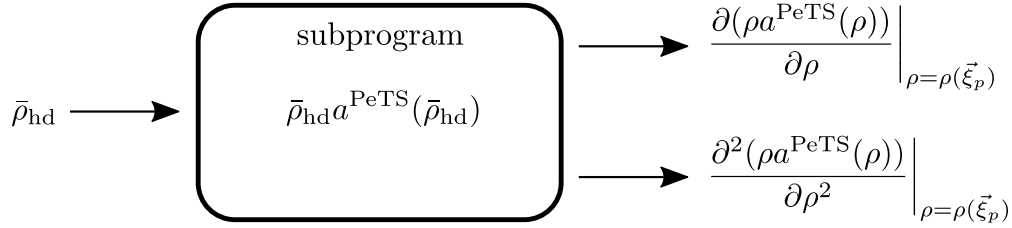


Figure 5.6: A subprogram computes (5.87) and (5.88). Input: $\bar{\rho}_{\text{hd}} = \rho(\vec{\xi}_p) + \epsilon_1 h_1 + \epsilon_2 h_2 + \epsilon_1 \epsilon_2 0$. Output: derivatives with respect to ρ at quadrature point.

6 Numerical Results

The PF model and its implementation that are discussed in the previous chapters shall be put to the test. Thus, this chapter presents examples of different wetting and also other scenarios.

The first two sections are concerned with static scenarios. Firstly, wetting scenarios on different surfaces are investigated using the empirical Helmholtz free energy. Secondly, a comprehensive investigation of the physical properties of the static PF model with the EoS based Helmholtz free energy is conducted. The third section presents dynamic wetting scenarios with the EoS based Helmholtz free energy.

To demonstrate the significance of the results from the PF simulations, some of them are compared to MD simulations of the same scenario. This is done for static as well as dynamic scenarios that use the EoS based Helmholtz free energy. The comparison validates the PF model on the nanoscale and demonstrates its strong physical foundation. The MD simulations themselves are not part of this work. The details of the MD setups are not stated here. Instead, the reader is referred to the corresponding publications.

6.1 Static Scenarios using the empirical Helmholtz Free Energy

The empirical Helmholtz free energy is used for the scenarios that are presented in this section. Therefore, the results have a phenomenological character. Nevertheless, they demonstrate some of the key capabilities of the underlying model. These include the prediction of equilibrium states for static wetting. Such equilibrium states are computed for plane as well as structured and more complex surfaces. Subsequently a post-processing of eigenvalues and eigenvectors of the system matrix is presented in order to investigate the stability of equilibrium states. Since the results of this section are valid on all length scales, the input parameters for the numerical computations are stated in a dimensionless manner.

6.1.1 Wetting of Plane Surfaces

The static equilibrium configuration of a droplet on a plane surface is computed. The computational domain is a cube with edge length 10 and 67 elements across each edge. Into this domain a single droplet with interface width $l^e = 1.5$ is placed.

Two different sets of surface tensions and droplet sizes are considered. The first set is given by $\gamma_{lv} = 1.000$, $\gamma_{sl} = 0.500$, $\gamma_{sv} = 1.000$ which yields a theoretical contact angle of $\Theta = 60^\circ$, cf. (2.2). The second set is given by $\gamma_{lv} = 1.000$, $\gamma_{sl} = 1.000$, $\gamma_{sv} = 0.134$ which yields a theoretical contact angle of $\Theta = 150^\circ$. The initialization is chosen to roughly match the theoretical contact angles with a droplet initialization radius of $r_{ini} = 3.0$ for the first set of surface tensions and $r_{ini} = 3.5$ for the second set of surface tensions. Gravitational effects are neglected.

Iso-surfaces of the computed equilibrium configurations for the first and second setup are shown in Figure 6.1 (left) and (right), respectively. As can be seen, the contact angles of the computed equilibrium configurations represent the theoretical contact angles. The agreement between computed and theoretical contact angles has been studied in more detail in [Blauwhoff 2015; Teto 2018]. However, for the sake of conciseness this is not shown here. This basic example demonstrates that the model is capable of computing equilibrium configurations of droplets for different wettability conditions. It also shows that the inclusion of the energy contributions of the surface tensions γ_{sl} and γ_{sv} by additional surface elements, cf. section 5.2, is suitable.

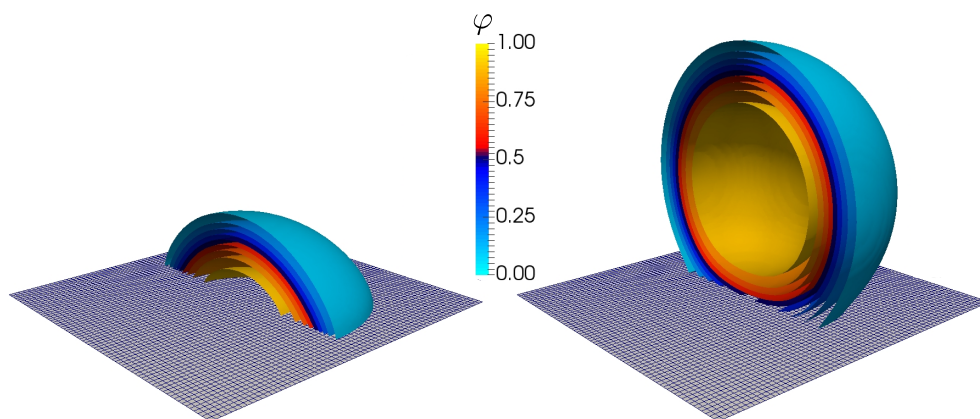


Figure 6.1: Droplet on plane surface. The plots show iso-surfaces of the computed equilibrium configurations for the first set of surface tensions that leads to a theoretical contact angle of $\Theta = 60^\circ$ (left) and for the second set of surface tensions that leads to a theoretical contact angle of $\Theta = 150^\circ$ (right). The contact angles of the computed equilibrium configurations represent the theoretical contact angles.

6.1.2 Wetting of Structured Surfaces

The FE implementation allows the modeling of structured and therefore more complex surfaces. Two examples are given in this section. The first example shows a two-dimensional representation of a droplet on a spike structure. The second example shows the relaxation and equilibrium configuration of a droplet on a circular pedestal. The examples are originally published in [Diewald et al. 2016, 2017].

For the droplet on spikes, the surface tensions from the second set of section 6.1.1 are used, $\gamma_{lv} = 1.000$, $\gamma_{sv} - \gamma_{sl} = -0.866$. Again, this gives a theoretical contact angle of $\Theta = 150^\circ$. As only the difference between γ_{sv} and γ_{sl} influences the contact angle but not their absolute values, only this difference is stated in the following. Mobility parameter, time step size, and the tolerance value for abandoning the evolution equation are $M = 0.5$, $\Delta t = 0.005$, and $e_{tol}/(\rho' - \rho'')^2 = 10^{-3}$. Gravitational effects are neglected and the backward Euler time integration scheme is used. The interface width is set to $l^e = 0.5$. The spikes are $5l^e$ high and have a distance of $2.5l^e$ between each other. The discretization uses 6.2 element edges per l^e . The droplet is initialized such that it sits inside of the spike structure.

Figure 6.2 (left) shows the distribution of φ for different times t . As it was already mentioned in section 3.5, the time t should not be understood as the physical time but as the time of the numerical relaxation when the static Allen-Cahn model is used. The top most plot shows the initialization state and the bottom most plot the static equilibrium. During the relaxation, the droplet is traveling upwards which reduces its contact area with the solid surface. In the static equilibrium, the droplet is not in contact with the solid surface. This dewetting behavior mimics the self-cleaning properties of artificial as well as natural surfaces like the one of the lotus flower.

For the droplet on a circular pedestal, the surface tensions are $\gamma_{lv} = 0.403$, $\gamma_{sv} - \gamma_{sl} = 0.285$. The resulting theoretical contact angle is $\Theta = 45^\circ$. Mobility parameter, time step size, and the tolerance value for abandoning the evolution equation are $M = 500$, $\Delta t = 0.005$, and $e_{tol}/(\rho' - \rho'')^2 = 10^{-3}$. Gravitational effects are neglected and the backward Euler time integration scheme is used. The interface width is set to $l^e = 3$. The diameter of the pedestal is approximately $13.3l^e$ and the height of the pedestal is approximately $4.2l^e$. The discretization uses approximately 5 element edges per l^e . The droplet is initialized such that it sits on the side of the pedestal.

Figure 6.2 (right) shows iso-surfaces of φ for different times t . Again, the top most plot shows the initialization state and the bottom most plot the static equilibrium. During the relaxation, the droplet moves towards the top of the pedestal.

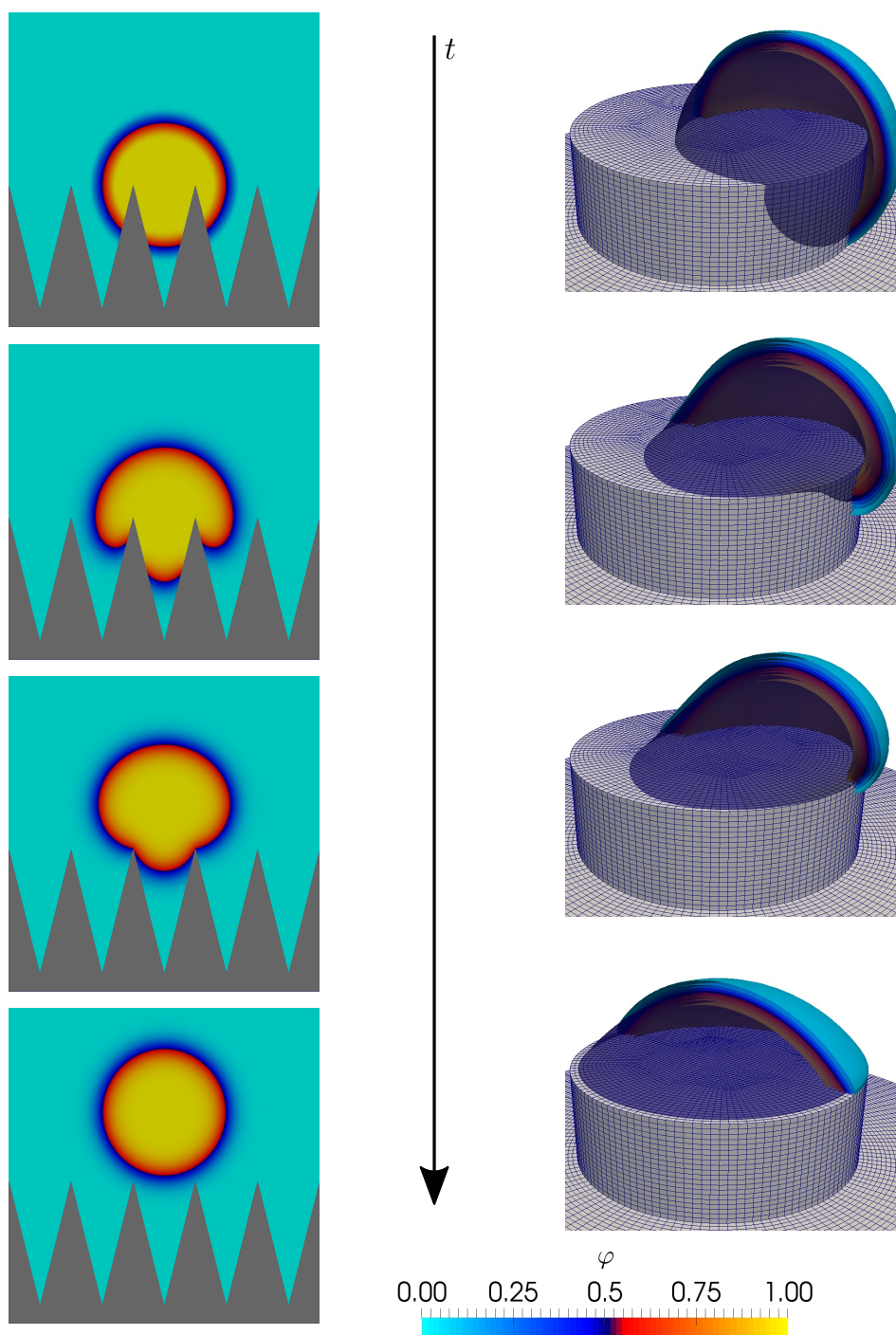


Figure 6.2: Contour plots of φ for droplet on spikes (left column) and iso-surfaces for droplet on circular pedestal (right column) at different relaxation times t . The top row shows the initialization states and the bottom row the static equilibrium. [Diewald et al. 2016, 2017]

In the static equilibrium, the droplet is sitting symmetrically at the middle of the pedestal. This configuration is known as the epitaxial Cassie state. The evolution shows that the droplet position on top of the pedestal is energetically more favorable than the droplet position on the side of the pedestal.

The examples above demonstrate that the presented phase field approach is capable of computing static equilibrium configurations for wetting scenarios that include structured and more complex surface geometries. Especially for such surface geometries, the question arises whether the static solution that was found represents a true energy minimum or just a local minimum or possibly a saddle point. It is not possible to compute the static solution for these scenarios analytically. Instead, a post-processing of eigenvalues and eigenvectors of the system matrix can be used to determine the character of the found solution. This is demonstrated in the next section.

6.1.3 Stability of the Solution

As it is shown in section 3.5.2, the static equilibrium solution of the static Allen-Cahn model is equivalent to the first order optimality condition of an energy functional. Naturally, this includes the possibility of obtaining a saddle point or a maximum rather than a minimum of the energy functional. In order to investigate if such an unstable solution was found, the eigenvalues and eigenvectors of the system matrix can be evaluated in a post-processing step. The approach is originally published in [Diewald et al. 2018b] on which this section is based.

Solving the quasi-static limit condition (3.73), which is equivalent to solving (3.2), can lead to the computation of saddle points and maxima rather than minima of the energy. The usage of an evolution equation, cf. (3.68) and (3.3), can relax the order parameter towards a solution that represents a saddle point.

The evolution equation does not lead away from a saddle point or maximum if (by chance) an initialization is chosen that represents a saddle point or maximum. The evolution equation does lead away from a saddle point or maximum towards a local minimum if an initialization is chosen that is just close to a saddle point or maximum. However, since $\delta_\varphi F$ is very small in the vicinity of a saddle point or maximum, the evolution towards the local minimum would be very slow. A velocity norm, cf. (3.72), is used to facilitate the cumbersome determination of when the evolution is close to a solution. The slow evolution towards the local minimum in the vicinity of a saddle point or maximum would promote the conclusion that the evolution is close to a solution and can be stopped. Solving the quasi-static limit condition in a subsequent step would eventually lead to the convergence of the order parameter to a configuration representing a saddle point or maximum.

But even if the quasi-static limit condition is not solved in a subsequent step, the solution state would potentially still be close to a saddle point or maximum. The post-processing of eigenvalues and eigenvectors of the system matrix as it is presented in the following can reveal the fact that the found configuration (which would be viewed as a solution) is in fact not a solution. This post-processing can not only be helpful if an initialization was chosen that is close to a saddle point or maximum (which is in general not known beforehand). In the field of PF models for coupled problems the suggested post-processing can gain additional relevance. The energy landscape of PF models for fracture can change due to outer loads. The present post-processing can be used to determine if this change turned a former local minimum into a saddle point or maximum. The approach does not depend on the choice of evolution equation. It can easily be adapted to models utilizing a different evolution equation.

The approach presented here should not be confused with classical stability analysis of droplets as it has been undertaken for a variety of different substrates, see e.g. [Blecula et al. 2009; Brinkmann et al. 2005; Brinkmann and Lipowsky 2002; Checco et al. 2012; Dorfler et al. 2013; Honisch et al. 2015; Kargupta et al. 2000; Mechkov et al. 2007; Rosso and Virga 2004; Thiele et al. 2003]. In contrast to these works, the approach presented here is concerned with the investigation of the character of a static solution state of a PF model for droplets.

The eigenproblem that is considered in the following reads

$$(\mathbf{S}_{\text{sol}} - \Lambda \mathbf{1}) \vec{s} = \vec{0}. \quad (6.1)$$

In this, \mathbf{S}_{sol} is the system matrix for the solution state of the quasi-static limit condition, cf. (5.74) with $c^{\text{tint}} = 0$. Eigenvalue and eigenvector are denoted by Λ and \vec{s} . Solving (6.1) yields eigenpairs Λ_i, \vec{s}_i with $i \in [1, n_{\text{dof}}^\rho + 1]$, where n_{dof}^ρ is the total number of degrees of freedom for ρ , i.e. the length of $\vec{\rho}$. The additional eigenpair originates from the Lagrange multiplier constraint. The eigenvectors \vec{s}_i represent a perturbation from the solution state. If the corresponding change of the residual vector has the same sign as the perturbation, i.e. the solution lies within a convex (stable) region of the energy landscape, the eigenvalue Λ_i is positive. Analogously, a solution state that lies within a concave (unstable) region of the energy landscape yields a negative eigenvalue. A subspace iteration is used to extract the lowest eigenpairs.

In the following, the post-processing of eigenvalues and eigenvectors of the system matrix is demonstrated by means of three two-dimensional examples. The examples show a droplet without surface contact, a droplet that is in contact with a plane surface, and a droplet that is sitting on a pedestal. While the first two examples show how the obtained eigenpairs should be read, the third example presents

a case in which the unstable character of a solution configuration is revealed. All examples use an equidistant mesh and the interface width $l^e = 1$. Coarse, medium, and fine meshes are used. They have element sizes with 3.2, 6.4, and 12.8 element edges per l^e , respectively. Gravitational effects are neglected and the backward Euler time integration scheme is used where applicable.

Droplet without surface contact

For the first example, the static equilibrium configuration is directly computed from the initialization state without the use of the evolution equation.

Figure 6.3 (bottom) shows the eigenvalues with smallest absolute values for the coarse as well as the medium mesh. The eigenvalues come in pairs of similar size. The most substantial difference between the eigenvalues of the computation with the coarse and the medium mesh is found in the first pair. For the first pair, the computation with the medium mesh yields eigenvalues that are closer to zero by five orders of magnitude. The difference between the eigenvalues of the coarse and the fine mesh is much smaller for the other eigenvalue pairs.

Figure 6.3 (top) shows contour plots of $\vec{\rho} + \vec{s}_i$ for the coarse mesh. The plots do not show the entire domain. The white lines in the plots represent the $\varphi = 0.5$ iso-line of the static equilibrium configuration. The plots for $i = 1, 2$ reveal that the first two eigenvalues belong to a purely translational disturbance of the droplet. As this disturbance does not lead to an immediate energy change, the first two eigenvalues are zero. A first-degree droplet deformation can be seen in the plots for $i = 3, 4$. The second-degree droplet deformation is obtained for $i = 5, 6$. A rise of the degree of deformation (which is equivalent to an increase of the frequencies in the shape change along the perimeter of the droplet) is accompanied by a rise of the eigenvalues. The deformations belonging to the same degree of deformation differ by a rotation of the deformation, only. The corresponding eigenvalues are of almost equal size.

All deformations show positive eigenvalues. This indicates that if a droplet is deformed as shown in the contour plots, it will restore its circular shape in order to minimize its energy.

The coarse mesh is chosen for the contour plots since it yields larger deformations (a scaling of the eigenvectors does not scale the deformation). Nonetheless, the results obtained with the medium mesh emphasize the fact that there is no energy change for a purely translational movement of the droplet.

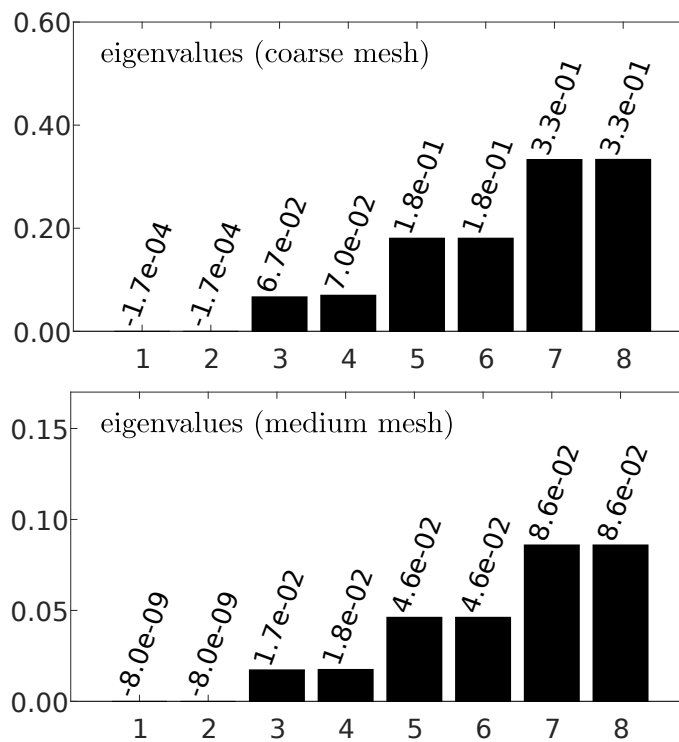
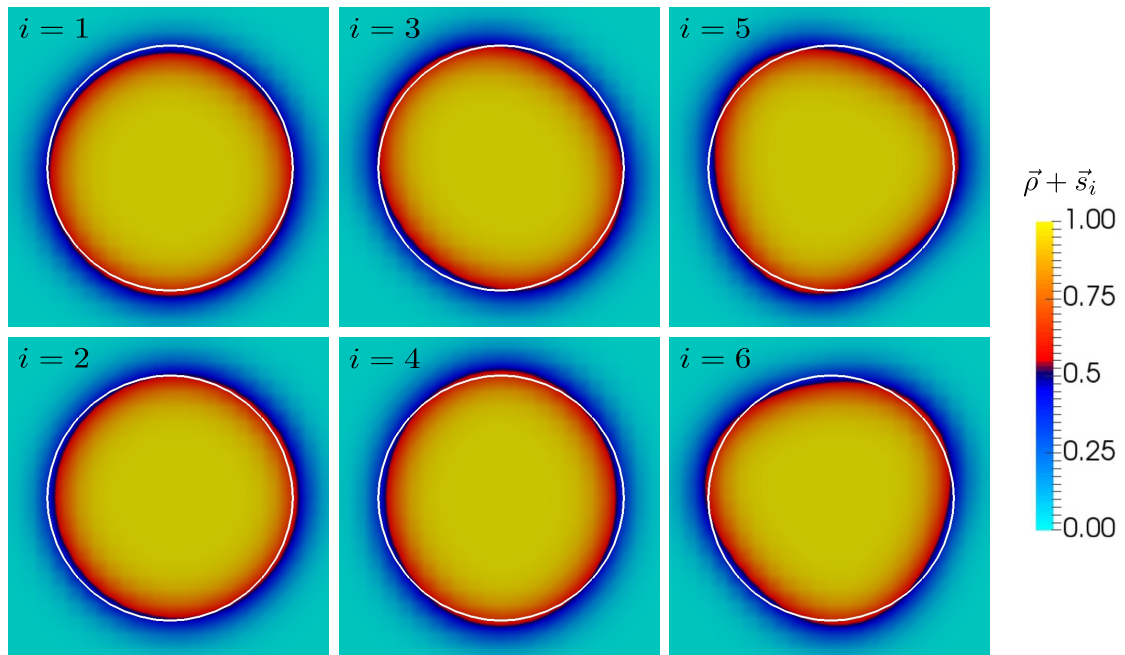


Figure 6.3: Droplet without surface contact. Top: Contour plots of $\vec{\rho} + \vec{s}_i$ for coarse mesh. Bottom: Eigenvalues with smallest absolute values for coarse and medium mesh. [Diewald et al. 2018b]

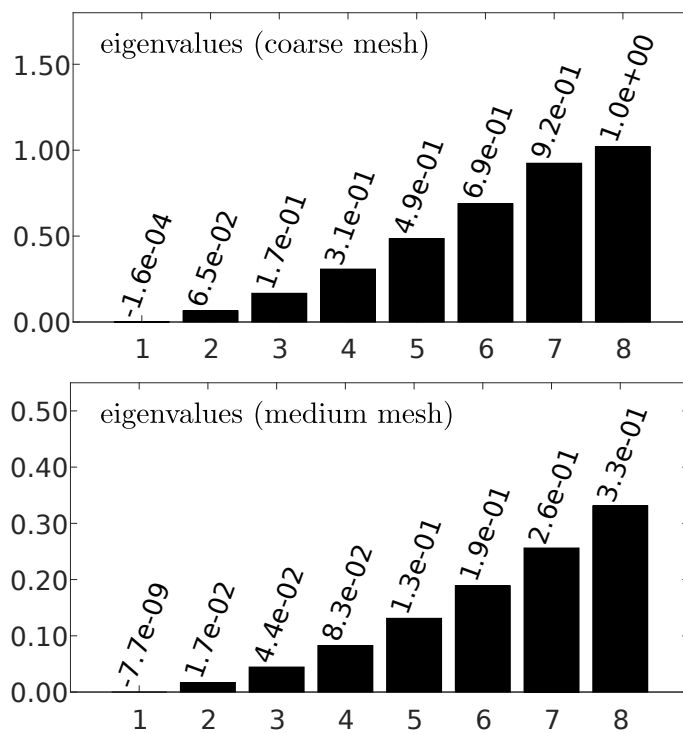
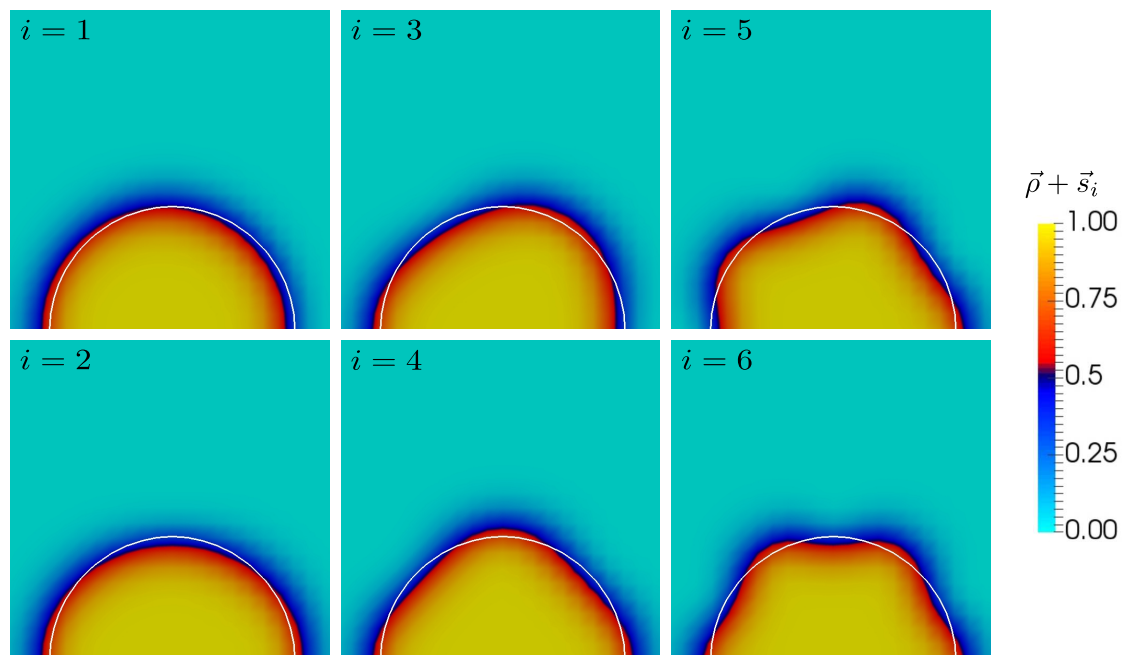


Figure 6.4: Droplet with surface contact. Top: Contour plots of $\vec{\rho} + \vec{s}_i$ for coarse mesh. Bottom: Eigenvalues with smallest absolute values for coarse and medium mesh. [Diewald et al. 2018b]

Droplet with surface contact

For the second example, the theoretical contact angle is set to $\Theta = 90^\circ$ ($\gamma_{lv} = 1.000$, $\gamma_{sv} - \gamma_{sl} = 0.000$). Again, the static equilibrium configuration is directly computed from the initialization state without the use of the evolution equation.

Figure 6.4 (bottom) shows the eigenvalues with smallest absolute values for the coarse as well as the medium mesh. Now, the eigenvalues do not come in pairs of similar size. The most substantial difference between the eigenvalues of the computation with the coarse and the medium mesh is only found in the first eigenvalue. The differences between the eigenvalues of the coarse and the fine mesh have the same order of magnitude as in the first example.

Figure 6.4 (top) shows contour plots of $\vec{\rho} + \vec{s}_i$ for the coarse mesh. The plots do not show the entire domain. As before, the white lines in the plots represent the $\varphi = 0.5$ iso-line of the static equilibrium configuration. The first eigenvalue belongs to a purely translational disturbance of the droplet in horizontal direction. The surface confines a translational disturbance of the droplet in vertical direction. Therefore, no such disturbance is found within the first eight eigenvalues. First- and second-degree droplet deformation can be seen for $i = 2$ and $i = 3$. Due to the confinement that is given by the surface, no rotated deformation of the same degree is found. The first- and second-degree of droplet deformation yield eigenvalues that are of similar size as in the first example. This holds true for the coarse and the fine mesh. The first example already revealed that a rise of the degree of droplet deformation is accompanied by a rise of the corresponding eigenvalue. This is confirmed by the plots for $i = 4, 5, 6$. The droplet deformations are similar to the shapes of vibrating droplets, see e.g. [Dong et al. 2006].

Droplet on pedestal

In the third example, a droplet that is sitting on a pedestal is investigated. Two different initialization states are used. The first initialization places the droplet centered on the edge of the pedestal such that the droplet has the same contact area with the top and the side of the pedestal. The second initialization is similar to the first initialization but shifts the droplet a little off-center such that the droplet has a slightly larger contact area with the top of the pedestal than the side of the pedestal. For both initializations eleven different theoretical contact angles between $\Theta = 50^\circ$ and $\Theta = 100^\circ$ ($\gamma_{lv} = 1.000$, $\gamma_{sv} - \gamma_{sl} \in [-0.174, 0.643]$) are considered. Mobility parameter, time step size, and the tolerance value for abandoning the evolution equation are $M = 100$, $\Delta t = 0.005$, and $e_{\text{tol}}/(\rho' - \rho'')^2 = 10^{-3}$. All computations use the fine mesh.

Figure 6.5 (a) and (b) show contour plots of the static equilibrium configurations

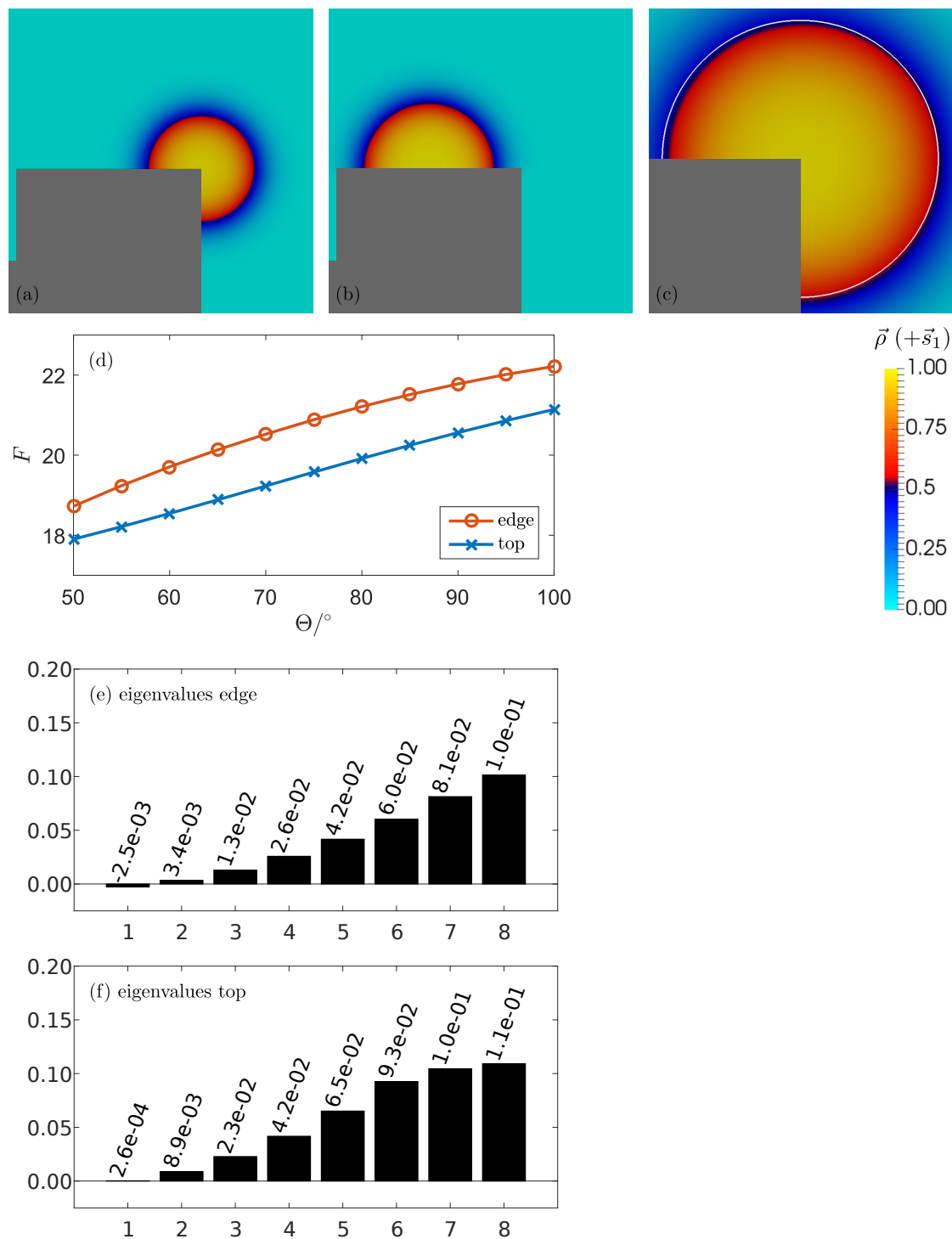


Figure 6.5: (a), (b): Contour plots of the static equilibrium configurations for first and second initialization and $\Theta = 90^\circ$, respectively. (c): Contour plot of $\vec{\rho} + \vec{s}_1$ for droplet on edge of pedestal and $\Theta = 90^\circ$. (d): Energy for droplet on edge and top of pedestal and different contact angles. (e), (f): Eigenvalues with smallest absolute values for droplet on edge and top of pedestal and $\Theta = 90^\circ$. [Diewald et al. 2018b]

for the first and second initialization and a theoretical contact angle $\Theta = 90^\circ$, respectively. It is evident that the two different initialization states lead to two different static equilibrium configurations. The droplet stays on the edge of the pedestal for the initialization that placed the droplet directly centered on the edge. Although the second initialization placed the droplet just a little off-center the edge of the pedestal, the droplet travels on top of the pedestal and does not have a contact area with the side of the pedestal in the static equilibrium configuration. By solely looking at the contour plots, it is not evident if both static equilibrium configurations represent a local energy minimum, i.e. if they are stable.

Figure 6.5 (d) compares the energy, i.e. the total PF potential F of the computational domain, cf. (3.74), for the droplet on the edge and the droplet on top of the pedestal for all considered contact angles. The total PF potential has higher values for the droplet that is sitting on the edge of the pedestal regardless of the contact angle. The configuration with the droplet on the edge of the pedestal cannot represent a global energy minimum. Still, no insights regarding the (local) stability of the configurations are gained. They might represent a local minimum, a saddle point, or a maximum of the energy landscape.

Figure 6.5 (e) and (f) show the eigenvalues with smallest absolute values for the droplet on the edge and the droplet on top of the pedestal. The first eigenvalue for the droplet on the edge of the pedestal is negative. Figure 6.5 (c) shows a contour plot of $\vec{\rho} + \vec{s}_1$. The white line represents the $\varphi = 0.5$ iso-line of the static equilibrium configuration. The negative eigenvalue belongs to a droplet disturbance away from the center of the edge of the pedestal. With this, it is evident that the configuration with the droplet on the edge of the pedestal is not stable. The smallest disturbance would cause it to travel away from the center of the edge of the pedestal. The configuration is not strictly unphysical. However, it can only be reached in an undisturbed environment which does in general represent a too ideal assumption. Without the present post-processing of eigenvalues and eigenvectors, this fact would not have been revealed and the static equilibrium configurations of the PF might have been misinterpreted as a true solution. The first eigenvalue for the droplet on top of the pedestal is positive but close to zero. Although the fine mesh was used, it is further away from zero (five orders of magnitude) than the first eigenvalues of the droplet without surface contact for the medium mesh. This suggests, that the droplet is still influenced by the confinement of the two edges to its right and left. The configuration with the droplet on top of the pedestal represents a (meta-)stable configuration.

The examples above demonstrate that for PF computations regarding droplets the post-processing of eigenvalues and eigenvectors of the system matrix can lead to a better understanding of the energy changes for basic droplet disturbances.

More than this, it can be a useful tool in order to determine the stability of a solution. The visualization of the eigenvectors can be especially useful. While the eigenvalues are sufficient to determine the character of a configuration, the eigenvectors tell in which direction the droplet would need to evolve in order to move away from that saddle point or maximum. The present approach lends itself for an application not only in the present PF model for droplets but also for other PF models that obtain their static equilibrium configurations by the first order optimality condition of an energy functional.

6.2 Static Scenarios using the EoS based Helmholtz Free Energy

The EoS based Helmholtz free energy is used for the scenarios that are presented in this section. The results do not only have a phenomenological character. Instead, they represent the physical behavior of the LJTS fluid. For validation purposes some of the results are compared to MD simulations. The scenarios, which include phase separation, planar interfaces and liquid droplets within a vapor phase, are originally published in [Diewald et al. 2018a].

For all PF simulations, the computational domain is a cube with edge length $20 \sigma^{\text{LJ}}$ and 80 elements across each edge. Gravitational effects are neglected and the backward Euler time integration scheme is used where applicable.

6.2.1 Phase Separation

The first scenario shall test the robustness of the model regarding phase separation. The computational domain is initialized with a random density distribution. This initialization is obtained by setting the density value for each of the 81^3 nodes to a random density value between ρ' and ρ'' . The generation of the random density values utilizes the MATLAB “rand” function ($\bar{\rho}^0 = \rho'' + (\rho' - \rho'') \text{rand}(81^3, 1)$). The resulting steep density gradients represent a challenging initialization for the PF model.

Temperature and total mass are $T = 0.7 \frac{\epsilon^{\text{LJ}}}{k_{\text{B}}}$ and $m_{\text{B}} = 3200 M^{\text{LJ}}$. Mobility parameter, time step size, and the tolerance value for abandoning the evolution equation are $M = 10 \frac{M^{\text{LJ}}}{(\sigma^{\text{LJ}})^4} \sqrt{\frac{M^{\text{LJ}}}{\epsilon^{\text{LJ}}}}$, $\Delta t = 0.005 \sigma^{\text{LJ}} \sqrt{M^{\text{LJ}}/\epsilon^{\text{LJ}}}$, and $e_{\text{tol}} = 10^{-3} \frac{(\epsilon^{\text{LJ}})^2 (\sigma^{\text{LJ}})^3}{(M^{\text{LJ}})^2}$.

Figure 6.6 shows iso-surfaces of ρ for different times t . The total computational runtime, i.e. the time at which the evolution equation is abandoned, is denoted by t_{r} . The first plot shows the initialization state and the last plot shows the static equilibrium configuration.

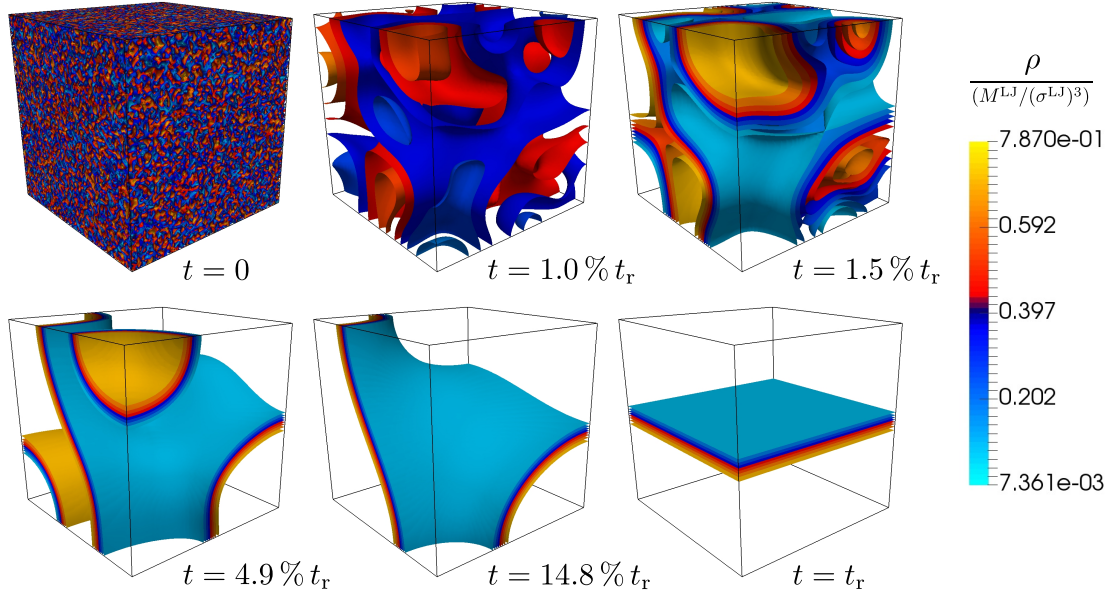


Figure 6.6: Phase separation. Iso-surfaces of ρ for different times t . The first plot shows the initialization state with a random density distribution. The last plot shows the static equilibrium configuration. [Diewald et al. 2018a]

During the evolution of the PF the phases start to separate from each other. At first numerous interfaces are created, cf. $t = 1.0\% t_r$ and $t = 1.5\% t_r$. Subsequently, the smaller interfaces vanish, cf. $t = 4.9\% t_r$ and $t = 14.8\% t_r$. The static equilibrium configuration shows a single planar interface between the liquid and the vapor phase. The results demonstrate that the PF model can handle the challenging random density initialization.

6.2.2 Planar Interface

The phase separation example shows that a planar interface configuration evolves from a random density distribution. This section gives a deeper investigation of the planar interface configuration.

The static equilibrium configurations for three temperatures $T \in \{0.7, 0.8, 0.9\} \frac{\epsilon^{LJ}}{k_B}$ are computed. The total mass is $m_B = 3200 M^{LJ}$ for all temperatures. The simulations are initialized with the same density profile. The initialization profile is shown by the dashed line in Figure 6.7 (a).

The density profiles of the equilibrium configurations are evaluated by plotting the density over a straight line that runs through the center of the computational area and is perpendicular to the interface, cf. Figure 6.7 (a). The width

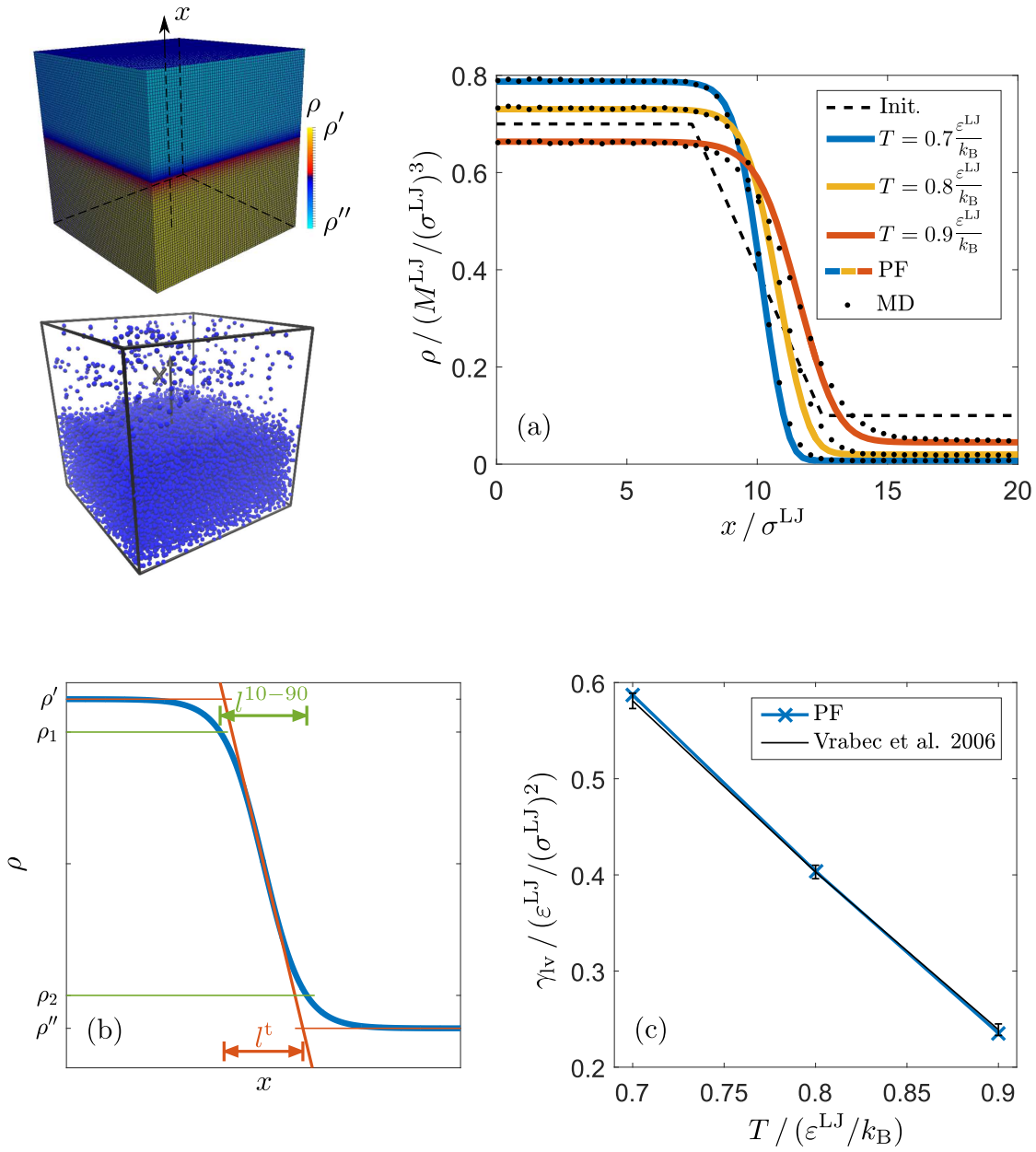


Figure 6.7: Planar interface. (a): Density profiles over a straight line that runs through the center of the computational area and is perpendicular to the interface for PF and MD simulations at three temperatures. The dashed line shows the initialization state of the PF simulations. (b): Comparison between the interface widths definitions l^{10-90} and l^t . (c): Comparison between the values for the surface tension γ_{IV} as obtained from the PF simulations and reported in [Vrabc et al. 2006] at three temperatures. [Diewald et al. 2018a]

of the interfaces is evaluated by means of two interface width definitions. The “10-90 thickness” l^{10-90} is defined as

$$l^{10-90} = |\vec{x}(\rho = \rho_2) - \vec{x}(\rho = \rho_1)| \quad (6.2)$$

with

$$\rho_1 = \rho'' + 0.9(\rho' - \rho'') \quad \text{and} \quad \rho_2 = \rho'' + 0.1(\rho' - \rho''). \quad (6.3)$$

The tangent interface width l^t is defined as the distance between the positions at which the tangent to the point where the density is in the arithmetic mean of the bulk phases reaches the values of the bulk phases. A comparison between l^{10-90} and l^t is shown in Figure 6.7 (b). For more details on the different interface widths see [Lekner and Henderson 1978].

The PF results are compared to MD results of the same scenario. For details on the MD simulations see [Diewald et al. 2018a].

Figure 6.7 (a) shows a comparison between the density profiles from the PF and the MD simulations. It is evident that the bulk density values of the PF and MD simulations show very good agreement. The values for l^{10-90} and l^t are reported in Table 6.1. The MD interface widths are wider than the PF interface widths. This is explainable by the fact that in the MD simulations a surface of equal density is not represented by a plane. Instead, it is a corrugated surface that changes its shape in time. The MD density profile is obtained by a time average, i.e. averaged in the directions tangential to the interface, of the density. The larger difference between the MD and PF interface widths for higher temperatures supports this explanation. The l^{10-90} interface widths are wider than the l^t interface widths. The only exception to this is the MD simulation at $T = 0.9 \frac{\varepsilon^{\text{LJ}}}{k_{\text{B}}}$.

The excess free energy Ω^{PeTS} , cf. (4.30), is computed in a post processing step. Dividing this energy by the surface area of the interface A yields the surface tension γ_{lv} from the PF simulations. Figure 6.7 (c) compares the resulting γ_{lv}

Table 6.1: Planar interface. Interface widths l^{10-90} and l^t , cf. Figure 6.7 (b), from PF and MD simulations for different temperatures. [Diewald et al. 2018a]

T	$0.7 \frac{\varepsilon^{\text{LJ}}}{k_{\text{B}}}$	$0.8 \frac{\varepsilon^{\text{LJ}}}{k_{\text{B}}}$	$0.9 \frac{\varepsilon^{\text{LJ}}}{k_{\text{B}}}$
l_{PF}^{10-90}	$2.070 \sigma^{\text{LJ}}$	$2.492 \sigma^{\text{LJ}}$	$3.229 \sigma^{\text{LJ}}$
l_{MD}^{10-90}	$2.353 \sigma^{\text{LJ}}$	$3.124 \sigma^{\text{LJ}}$	$4.232 \sigma^{\text{LJ}}$
l_{PF}^t	$2.042 \sigma^{\text{LJ}}$	$2.471 \sigma^{\text{LJ}}$	$3.122 \sigma^{\text{LJ}}$
l_{MD}^t	$2.205 \sigma^{\text{LJ}}$	$2.660 \sigma^{\text{LJ}}$	$4.274 \sigma^{\text{LJ}}$

values to the values reported in [Vrabec et al. 2006] which are obtained from MD simulations. Excellent agreement is found between the PF and the MD results. This confirms that the value for κ that is chosen in section 4.2 is valid for all three temperatures.

The computational effort is much lower for the PF simulations than for the MD simulations. The level of parallel computing is different between the PF and MD simulations and the PF implementation is not optimized for speed. The PF and MD simulations are also not carried out on the same machine. Solely to give an idea on how the computational effort differs between the PF and the MD simulations, the sums of the times spend on the individual CPUs are compared. This comparison shows a 50 times larger computational effort for the MD simulations ($\approx 1500\text{h}$) compared to the PF simulations ($\approx 30\text{h}$) at each temperature.

6.2.3 Liquid Droplet in Vapor Phase

The planar interface scenario shows that the PF simulations for the LJTS fluid show good agreement with MD simulations for the same fluid. This verifies that the PF results represent the physical behavior of the LJTS fluid in the static equilibria of planar interfaces. This section investigates if this is also the case for interfaces that are not planar.

Static equilibrium configurations for different values of the total mass $m_{\mathcal{B}}$ at $T = 0.7 \frac{\epsilon_{\text{LJ}}}{k_{\text{B}}}$ are computed. All simulations are initialized with a droplet that is surrounded by a vapor phase according to

$$\rho^0(r) = \frac{\rho'' - \rho'}{l_{\text{PF}}^t} \left(r - r_{\text{ini}} + \frac{l_{\text{PF}}^t}{2} \right) + \rho'. \quad (6.4)$$

In this, r is the distance to the center of the droplet and r_{ini} is the initialization radius. The initialization interface width and bulk density values are set to the values for l_{PF}^t , ρ' , and ρ'' obtained in section 6.2.2. With this, the total mass in the domain is defined by the initialization radius.

Firstly, the PF results for $m_{\mathcal{B}} = 800M^{\text{LJ}}$ are compared to MD results. Secondly, the PF results for several different $m_{\mathcal{B}}$ values are compared to analytic solutions.

Figure 6.8 (left) shows a contour plot of the static equilibrium configuration of the PF simulation for $m_{\mathcal{B}} = 800M^{\text{LJ}}$. The density inside the droplet is $\rho_l = 0.8060 \frac{M^{\text{LJ}}}{(\sigma^{\text{LJ}})^3}$. The density of the vapor phase is $\rho_v = 0.0113 \frac{M^{\text{LJ}}}{(\sigma^{\text{LJ}})^3}$. These values are compared to the density results from MD simulations of the same scenario in Figure 6.8 (right). For details on the MD simulations see [Diewald et al. 2018a]. The densities inside the droplet and in the vapor phase as obtained from the MD simulations

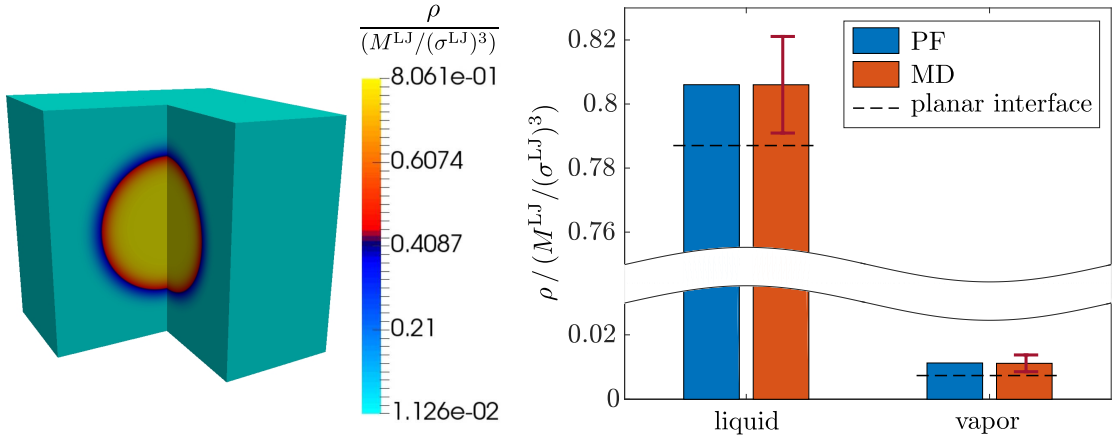


Figure 6.8: Liquid droplet in vapor phase with $m_B = 800M^{\text{LJ}}$ at $T = 0.7 \frac{\epsilon^{\text{LJ}}}{k_B}$. Contour plot of the static equilibrium configuration (left) and comparison of the liquid and vapor densities obtained from the PF simulation to the values obtained from MD simulations (right). [Diewald et al. 2018a]

are $\rho_l = 0.806(15) \frac{M^{\text{LJ}}}{(\sigma^{\text{LJ}})^3}$ and $\rho_v = 0.0112(26) \frac{M^{\text{LJ}}}{(\sigma^{\text{LJ}})^3}$. The number in parentheses indicates the statistical uncertainty in the last decimal digit. The PF simulations agree well with the MD simulations. The PF results lie within the error bars of the MD simulations. Figure 6.8 (right) does also show the bulk density from the planar interface scenario. These densities are depicted by dashed lines. Both, the density inside the droplet and the density in the vapor phase are higher for the droplet than they are for the planar interface. Due to the curvature of the interface, the surface tension γ_{lv} causes a rise of the pressure, and thereby of the density, inside the droplet. Following (3.73) the density of the vapor phase rises as well.

The remaining PF simulations of a liquid droplet in a vapor phase are initialized with

$$r_{\text{ini}} \in \{2, 3, 3.25, 3.5, 3.75, 4, 4.25, 4.5, 5\} \sigma^{\text{LJ}}. \quad (6.5)$$

Figure 6.9 shows the initialization state (left) and the static equilibrium state (right) for $r_{\text{ini}} = 3 \sigma^{\text{LJ}}$ (top) and $r_{\text{ini}} = 5 \sigma^{\text{LJ}}$ (bottom). As can be seen, small r_{ini} values can lead to a static equilibrium configuration with an (oversaturated) homogeneous vapor phase, i.e. the droplet disappears. If r_{ini} is chosen large enough the static equilibrium configuration shows a droplet inside a vapor phase. The smallest initialization radius that leads to the development of a stable droplet is investigated in the following.

An analytic prediction for the smallest initialization radius that leads to the deve-

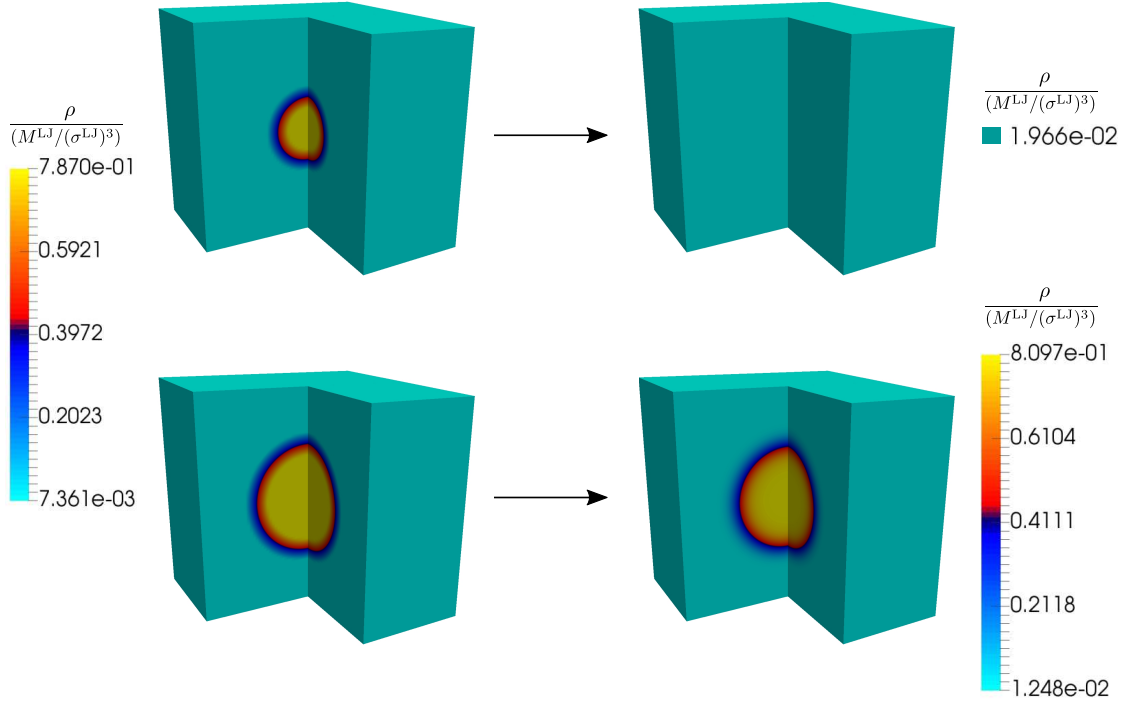


Figure 6.9: Liquid droplet in vapor phase. Initialization state (left) and the static equilibrium state (right) for $r_{\text{ini}} = 3\sigma^{\text{LJ}}$ (top) and $r_{\text{ini}} = 5\sigma^{\text{LJ}}$ (bottom). The droplet disappears for small r_{ini} values and a homogeneous density distribution is obtained. [Diewald et al. 2018a]

lopment of a stable droplet is made. For this, the values of the total PF potential F for two analytic equilibrium configurations are approximated. The analytic equilibrium configurations under consideration are a droplet in a vapor phase and a homogeneous density distribution. The total PF potential of the droplet in a vapor phase configuration is denoted by F_{d} . It is obtained by approximating the interface between the liquid and the vapor phase by a linear transition from ρ' to ρ'' , cf. Figure 6.10 (left). This configuration is equivalent to the initialization state, cf. (6.4). The value of F_{d} is computed by following the approach of Hofmann [2018] and assuming that the surface tension and width of the interface are constant. This is in accordance with classical nucleation theory based on the capillarity approximation [Farkas 1927; Volmer and Weber 1926]. The total PF potential of the homogeneous density distribution configuration is denoted by F_{h} . For further details on the computation of F_{d} and F_{h} see appendix C.

Figure 6.10 (right) shows a plot of F_{d} and F_{h} over r_{ini} . For small values of r_{ini} the total PF potential of the droplet in a vapor phase configuration F_{d} is larger than the

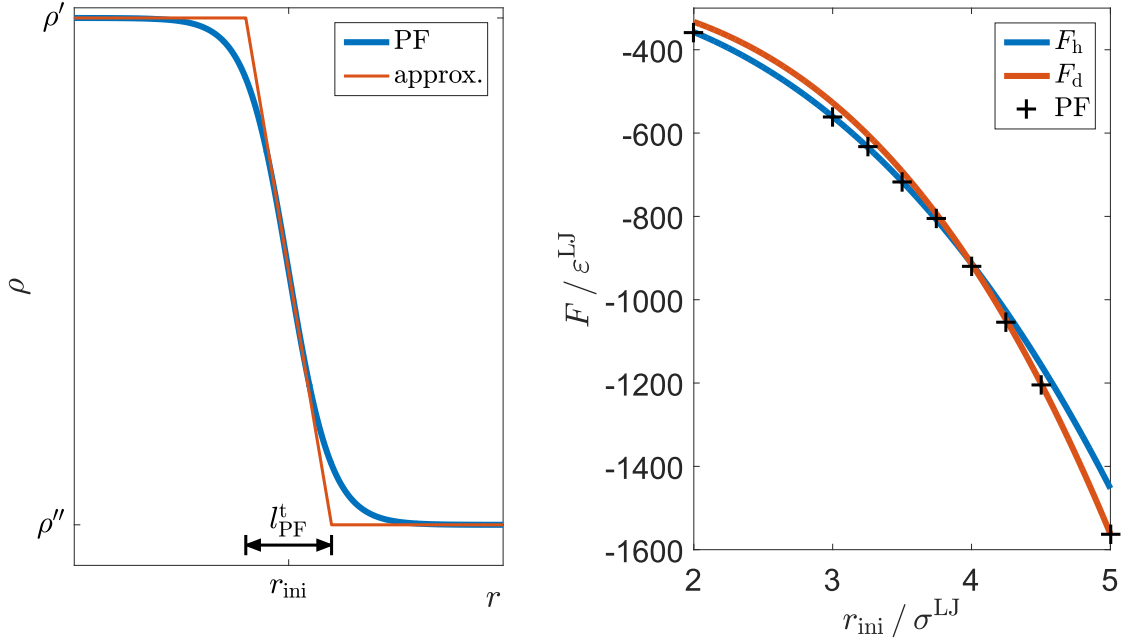


Figure 6.10: Liquid droplet in vapor phase. Left: Approximation of the interface between the liquid and the vapor phase by a linear transition from ρ' to ρ'' . Right: Analytic total PF potential for droplet in vapor phase (F_d) and homogeneous density distribution (F_h). The symbols show the total PF potential as obtained from the PF simulations. [Diewald et al. 2018a]

total PF potential of the homogeneous density distribution configuration F_h . This indicates that the droplet is not stable and the homogeneous density configuration is favored. Analogously, the droplet configuration is favored for larger values of r_{ini} where F_d is smaller than F_h . The r_{ini} value at which the curves of F_d and F_h cross each other represents the analytic prediction of the smallest initialization radius that leads to the development of a stable droplet. It is $r_{ini} = 3.99 \sigma^{LJ}$. The symbols in Figure 6.10 (right) show the total PF potential as obtained from the static equilibrium configurations of the PF simulations. They follow the low energy path of F_d and F_h . The simulation that is started with $r_{ini} = 3.75 \sigma^{LJ}$ is the first simulation that leads to a static equilibrium configuration with a droplet in a vapor phase. The analytic results and the simulation results show good agreement. An explanation for the small difference can be found in the linear approximation of the interface in the analytic expressions.

The liquid droplet in vapor phase scenario is investigated further by comparing the pressure difference between the inside and the outside of the droplet to the Young-Laplace equation as it is introduced in section 2.1. For this the equimolar

radius is computed for each static equilibrium configuration that shows a droplet in a vapor phase, i.e. for all simulations with $r_{\text{ini}} \geq 3.75 \sigma^{\text{LJ}}$.

The equimolar radius r_e is defined as

$$r_e = \left(\frac{3 \int_0^\infty (\rho(r) - \rho_v) r^2 dr}{\rho_l - \rho_v} \right)^{\frac{1}{3}}, \quad (6.6)$$

cf. [Hrubý et al. 2007]. Since $\rho(r) = \rho_v$ in the vapor phase, it is sufficient to evaluate the integral from 0 to $10 \sigma^{\text{LJ}}$, only. The pressure difference

$$\Delta p^{\text{h}} = p_l^{\text{h}} - p_v^{\text{h}} \quad (6.7)$$

is calculated by obtaining the pressure values p_l^{h} and p_v^{h} that correspond to ρ_l and ρ_v from the PeTS EoS for the LJTS fluid, respectively. For comparison, the Young-Laplace equation is evaluated, cf. (2.1). For this, the value of the surface tension γ_{lv} as computed in section 6.2.2 is used.

Figure 6.11 (left) shows the results for the equimolar radius over the total mass for each static equilibrium configuration that consists of a droplet in a vapor phase. The smallest stable droplet has an equimolar radius of $r_e = 3.17 \sigma^{\text{LJ}}$. Figure 6.11 (right) shows a plot of Δp^{h} and the pressure difference resulting from the Young-Laplace equation over r_e . For large r_e values, Δp^{h} and the pressure difference resulting from the Young-Laplace equation show good agreement. For smaller r_e values, a difference between the two is observed. These r_e values correspond to very small droplets with a droplet radius of similar size as the diffuse width of the interface between the liquid and the vapor phase. The disagreement between Δp^{h} and the pressure difference resulting from the Young-Laplace equation does therefore not surprise as the assumptions on which the Young-Laplace equation is based do not hold for such small droplets. The authors of [Falls et al. 1981] and [Langenbach et al. 2018] report a breakdown of the Young-Laplace equation for droplet radii smaller than approximately $5 \sigma^{\text{LJ}}$. This agrees well with the results of the PF simulations presented here.

The static Allen-Cahn model with the EoS based Helmholtz free energy proves to yield physically correct results for the LJTS fluid. For planar and non-planar interfaces, the PF simulations show good agreement with MD or analytic results. Not only the bulk properties but also those in the transition zone between the liquid and the vapor phase obtained from the PF simulations are physically meaningful. Furthermore, the PF model is robust with regard to unfavorable initialization states.

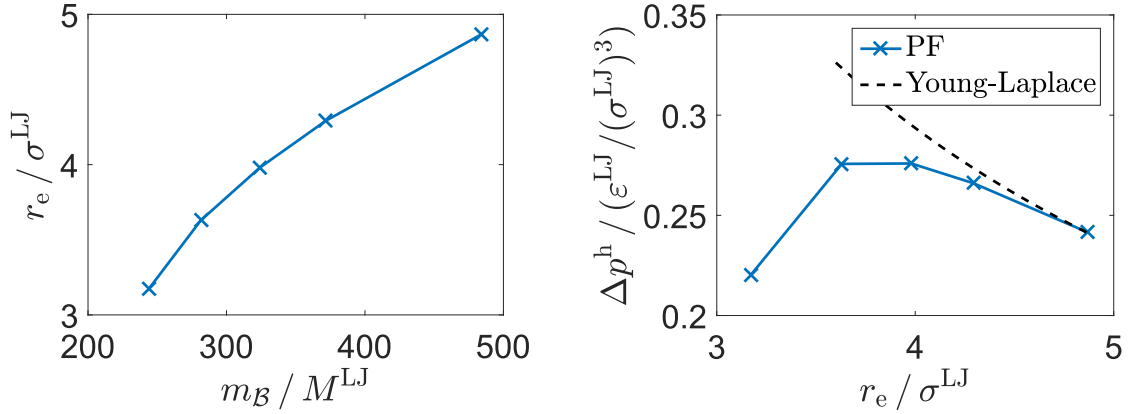


Figure 6.11: Liquid droplet in vapor phase. Left: Equimolar radius in the static equilibrium configuration over the total mass. Right: Pressure difference resulting from the PF simulations and pressure difference resulting from the Young-Laplace equation over the equimolar radius. [Diewald et al. 2018a]

6.3 Dynamic Scenarios using the EoS based Helmholtz Free Energy

For many engineering applications, the prediction of static equilibrium configurations is not sufficient. To determine the wetting properties of a machine component, the time dependent, i.e. dynamic, behavior of a droplet on a solid surface is of interest. The following scenarios demonstrate the ability of the dynamic Navier-Stokes-Korteweg model with the EoS based Helmholtz free energy to make predictions for dynamic wetting.

The scenarios show the wetting of structured surfaces as well as the movement of droplets on surfaces with a wettability gradient. Additionally, the properties of the newly developed semi-implicit energy stable time integration scheme, cf. section 5.1.2, are investigated by means of two basic scenarios. If not mentioned otherwise, a no-slip boundary condition ($\vec{v} = \vec{0}$) is prescribed on $\partial\mathcal{B}_s$.

6.3.1 Wetting of Structured Surfaces

The impact of a droplet on a structured component surface is investigated. The results are originally published in [Diewald et al. 2019].

A droplet with radius $r_{\text{ini}} = 5 \sigma^{\text{LJ}}$ is initialized with its center $12.5 \sigma^{\text{LJ}}$ above the bottom of the structured surface. The structure of the surface at the bottom of the computational domain can be seen in Figure 6.12. An equidistant mesh

with an element edge length of approximately $l_{\text{PF}}^t/13$ is used for the spatial discretization and the backward Euler time integration scheme with time step size $\Delta t = 0.05 \sigma^{\text{LJ}} \sqrt{M^{\text{LJ}}/\varepsilon^{\text{LJ}}}$ is used for the temporal discretization. The initial velocity in all of \mathcal{B} and the temperature are $\vec{v}^0 = \vec{0}$ and $T = 0.7 \frac{\varepsilon^{\text{LJ}}}{k_{\text{B}}}$. The gravitational acceleration is set to $g = 0.01 \frac{\varepsilon^{\text{LJ}}}{M^{\text{LJ}} \sigma^{\text{LJ}}}$. Instead of using the viscosity correlation of section 4.3 a constant viscosity $\eta^{\text{v}} = 0.01 \frac{\sqrt{\varepsilon^{\text{LJ}} M^{\text{LJ}}}}{(\sigma^{\text{LJ}})^2}$ is used.

Two different sets of surface tensions for the structured surface are considered. The first set $\gamma_{\text{sv}} - \gamma_{\text{sl}} = 0.000$ yields a theoretical contact angle of $\Theta = 90^\circ$. The second set $\gamma_{\text{sv}} - \gamma_{\text{sl}} = -0.503 \frac{\varepsilon^{\text{LJ}}}{(\sigma^{\text{LJ}})^2}$ yields a theoretical contact angle of $\Theta = 150^\circ$ (for the value of γ_{lv} at this temperature see section 6.2.2).

Figure 6.12 shows snapshots of the temporal evolution for $\Theta = 90^\circ$ (left) and $\Theta = 150^\circ$ (right). Until shortly before the impact, the temporal evolution of the droplet is identical for both contact angles, cf. first row of figures. Once the droplet is in contact with the structured component surface, the temporal evolution shows a contact angle dependent behavior. For $\Theta = 90^\circ$ the droplet fills the grooves of the structure and sinks in. The last plot shows a droplet that is sitting inside the structured surface (Wenzel state). For $\Theta = 150^\circ$ the droplet does not fill the grooves of the structure. It does not sink in and bounces off the structure. The last plot shows a droplet that is sitting on top of the structured surface (Cassie-Baxter state).

Comparing the temporal evolution of the droplet to the relaxation of the static scenarios that use the evolution equation, see e.g. Figure 6.2, the effects of inertial, that are inherent in the dynamic Navier-Stokes-Korteweg model, become apparent. The droplet impact scenario demonstrates that the dynamic Navier-Stokes-Korteweg model with the EoS based Helmholtz free energy can help the development of microstructures that are capable of retaining liquids or show self-cleaning properties.

6.3.2 Droplets on Surfaces with Wettability Gradient

In order to make significant predictions of the dynamic wetting behavior of a droplet, the dynamics of the Navier-Stokes-Korteweg model with the EoS based Helmholtz free energy and the viscosity correlation of section 4.3 need to be validated. This is done in the present section by investigating the dynamic behavior of droplets on surfaces with a wettability gradient. The PF results are compared to those from MD simulations.

A droplet that is sitting on a surface with spatially changing surface tensions $\gamma_{\text{sl}}, \gamma_{\text{sv}}$ shows different contact angles depending on the local value of γ_{sl} , and γ_{sv} . A spatial

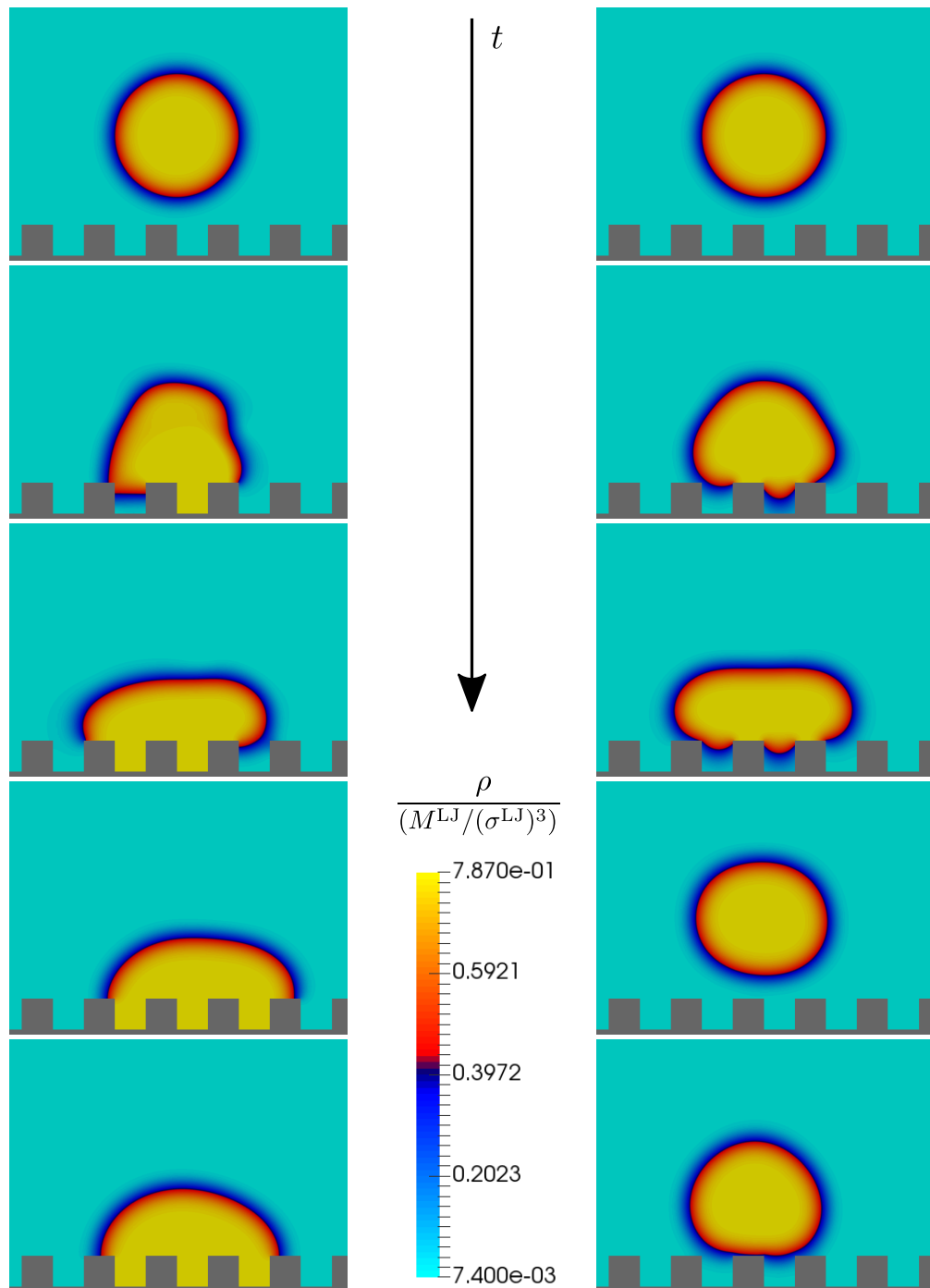


Figure 6.12: Wetting of structured surface. The snapshots of the temporal evolution show the impact of a droplet on a structured surface with $\Theta = 90^\circ$ (left) and $\Theta = 150^\circ$ (right). [Diewald et al. 2019]

gradient of the wettability, i.e. a gradient of the surface tensions, does therefore lead to a motion of the droplet on the surface. The effect is used by organisms that live in low-rainfall areas. The desert beetle uses surfaces with wettability gradients to collect water from the humid atmosphere [Chakraborty et al. 2015; Parker and Lawrence 2001]. The phenomenon can also be witnessed during the soldering of copper tubes where the motion of the tin droplets can to some extent be explained by the wettability gradient following from the temperature gradient [Brzoska et al. 1993]. There are also technical applications that make use of the phenomenon. To pump liquids through micro- or nanoscale pipes requires large pressure gradients [Halverson et al. 2008]. Instead of using classical pumps, surfaces with wettability gradients might be used in this area [Chakraborty et al. 2015]. The prescription of a controlled droplet motion by wettability gradients can also facilitate the development of lab-on-a-chip devices [Huang et al. 2014; Darhuber and Troian 2005].

Because of their evolving importance, surfaces that are characterized by a wettability gradient have been studied experimentally [Bliznyuk et al. 2011; Brzoska et al. 1993; Ichimura 2000; de Jong et al. 2019; Liu et al. 2017], theoretically [Brochard 1989; Pismen and Thiele 2006], by molecular and particle simulations [Chakraborty et al. 2015; Halverson et al. 2008; Li et al. 2013], as well as by continuum simulations [Chowdhury et al. 2019; Huang et al. 2014; de Jong et al. 2019; Kunti et al. 2018b; Li et al. 2017; Moosavi and Mohammadi 2011; Pan et al. 2015; Thiele et al. 2004]. The validation of PF simulations for surfaces with wettability gradients on the nanoscale by a comparison to MD simulations is, to the best of the author's knowledge, done in [Diewald et al. 2020a] for the first time. The present section is based on this work.

Figure 6.13 shows a sketch of the scenario studied in the following. A droplet is placed on a solid surface with a wettability gradient. The wettability gradient is characterized by a change of $\gamma_{sl} - \gamma_{sv}$ along the x -axis and causes a difference in the contact angles on the left and right side of the droplet. This difference leads to a net force and thus a motion of the droplet.

Two scenarios for the wettability gradient are simulated. In the first scenario, $\gamma_{sl} - \gamma_{sv}$ has a linear slope in x -direction and is symmetric with respect to the center of the solid surface. The maximum and minimum values of $\gamma_{sl} - \gamma_{sv}$ are chosen such that they correspond to theoretical contact angles of $\Theta = 150^\circ$ and $\Theta = 30^\circ$, respectively. In the second scenario, an almost identical slope of $\gamma_{sl} - \gamma_{sv}$ is used. The maximum and minimum values of $\gamma_{sl} - \gamma_{sv}$ are the same as for the first scenario. However, in contrast to the first scenario the value of $\gamma_{sl} - \gamma_{sv}$ jumps to the maximum value in the center of the solid surface. This discontinuous change of the wettability acts as a barrier. The simulation results reveal whether

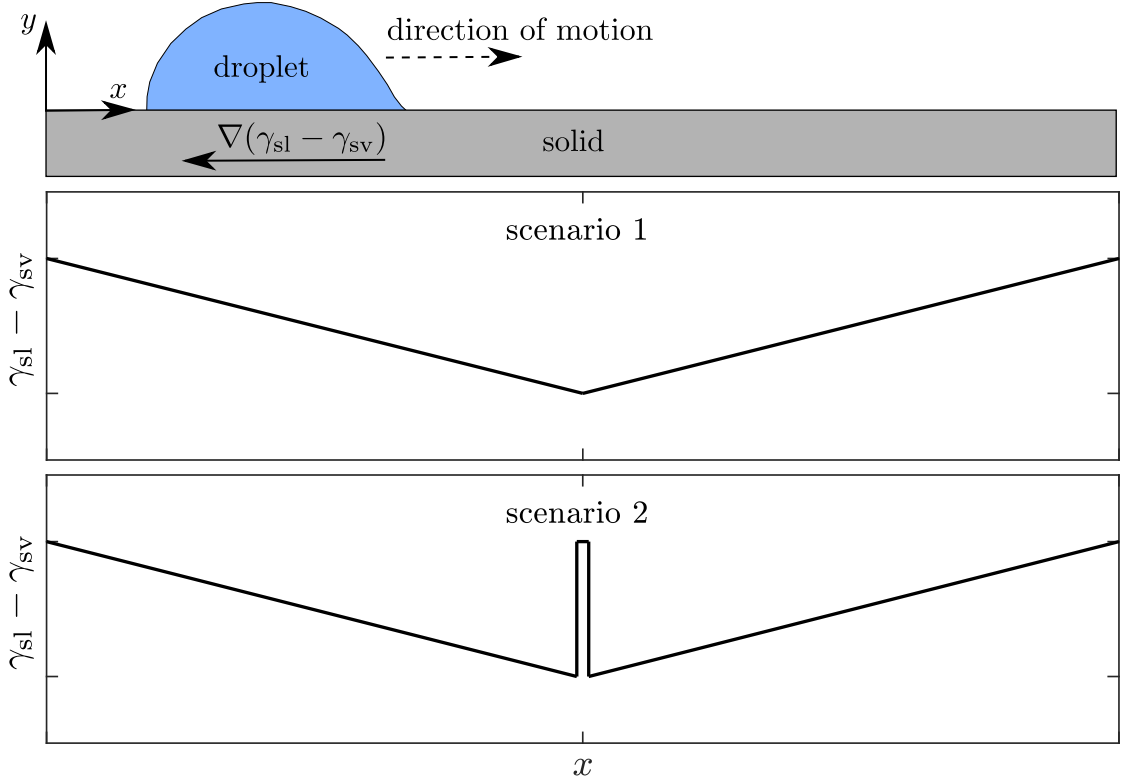


Figure 6.13: Sketch of droplet on surface with wettability gradient. A gradient of $\gamma_{sl} - \gamma_{sv}$ leads to different contact angles on the left and right side of the droplet and thus to a droplet motion. Two different slopes for $\gamma_{sl} - \gamma_{sv}$ are considered. [Diewald et al. 2020a]

the droplet is stopped by this barrier or whether it is able to overcome it.

The computational domain for both scenarios is a rectangle of size $180 \sigma^{LJ} \times 30 \sigma^{LJ}$ that is discretized by 768×128 elements. The initial velocity in all of \mathcal{B} and the temperature are $\vec{v}^0 = \vec{0}$ and $T = 0.7 \frac{\epsilon^{LJ}}{k_B}$. The backward Euler time integration scheme with time step size $\Delta t = 5 \sigma^{LJ} \sqrt{M^{LJ}/\epsilon^{LJ}}$ is used and gravitational effects are neglected. The initialization sets a hemispherical droplet with radius $r_{ini} = 20 \sigma^{LJ}$ on the bottom of the computational domain such that the distance between the center of the droplet and the left end of the computational domain in x -direction is $42 \sigma^{LJ}$,

$$\rho^0(r) = \frac{\rho' - \rho''}{2} \left[\tanh \left(\frac{-2(r - r_{ini})}{l_{PF}^t} \right) + 1 \right] + \rho''. \quad (6.8)$$

Again, r denotes the distance to the center of the droplet. The minimum and maximum values for $\gamma_{sl} - \gamma_{sv}$ that correspond to $\Theta = 150^\circ$ and $\Theta = 30^\circ$ are

$\gamma_{sl} - \gamma_{sv} = 0.5032 \sigma^{LJ}$ and $\gamma_{sl} - \gamma_{sv} = -0.5032 \sigma^{LJ}$ at $T = 0.7 \frac{\epsilon^{LJ}}{k_B}$. The width of the barrier in the second scenario is $0.469 \sigma^{LJ}$. The position of the centroid in x -direction is computed for each time step

$$x_c = \frac{\int_{\mathcal{B}} x \rho dV}{\int_{\mathcal{B}} \rho dV}. \quad (6.9)$$

Therefrom, the droplet velocity in x -direction v_x is evaluated. For details on the MD simulations see [Diewald et al. 2020a].

Figure 6.14 shows snapshots of the PF and MD simulations at different times t for the first scenario. Each MD particle is depicted by one bubble and a mirrored representation of the MD domain is shown. The first plot shows the initialization state and the last plot the static equilibrium configuration. In the initialization state the droplet has the same contact angle on its left and right side and is symmetric with respect to its center. Since a dynamic equilibration was used for the initialization of the MD simulation, the MD results do not show a perfectly symmetric droplet at $t = 0$. During the simulations, $t > 0$, the droplet shows different contact angles at its left and right side and exhibits a motion in positive x -direction. A good qualitative agreement is found between the PF and the MD snapshots regarding the transient development of the droplet's shape and position. The slight differences can be explained by the stochastic character of the MD simulations.

Figure 6.15 shows a quantitative comparison of the PF and MD results for the first scenario (left column) and the second scenario (right column). The first row shows the temporal evolution of the position of the centroid in x -direction. The second row shows the temporal evolution of the velocity in x -direction. The plots show raw as well as smoothed MD data. The MD data that is shown for $t < 0$ correspond to the equilibration of the MD droplet that is performed without applying the gradient of the surface tension. For $t > 0$, the gradient of the surface tension is applied and a droplet motion is observed.

In the first scenario, the influence of inertia becomes evident in the first time steps when the droplet accelerates to its maximum velocity, cf. $t \in [0, 200] \sigma^{LJ} \sqrt{M^{LJ}/\epsilon^{LJ}}$. In these time steps v_x shows a linear and x_c a quadratic behavior with respect to time. This indicates that the droplet motion is dominated by a constant driving force in positive x -direction. For this two-dimensional scenario the driving force is given by the difference between the values for $\gamma_{sl} - \gamma_{sv}$ at the left and right side of the droplet. In these early time steps, the droplet is not far from its initial position. The difference between the values for $\gamma_{sl} - \gamma_{sv}$ at the left and right side of the droplet is therefore roughly constant. This explains the temporal evolution of v_x and x_c . Once the maximum velocity is reached, the droplet motion shows

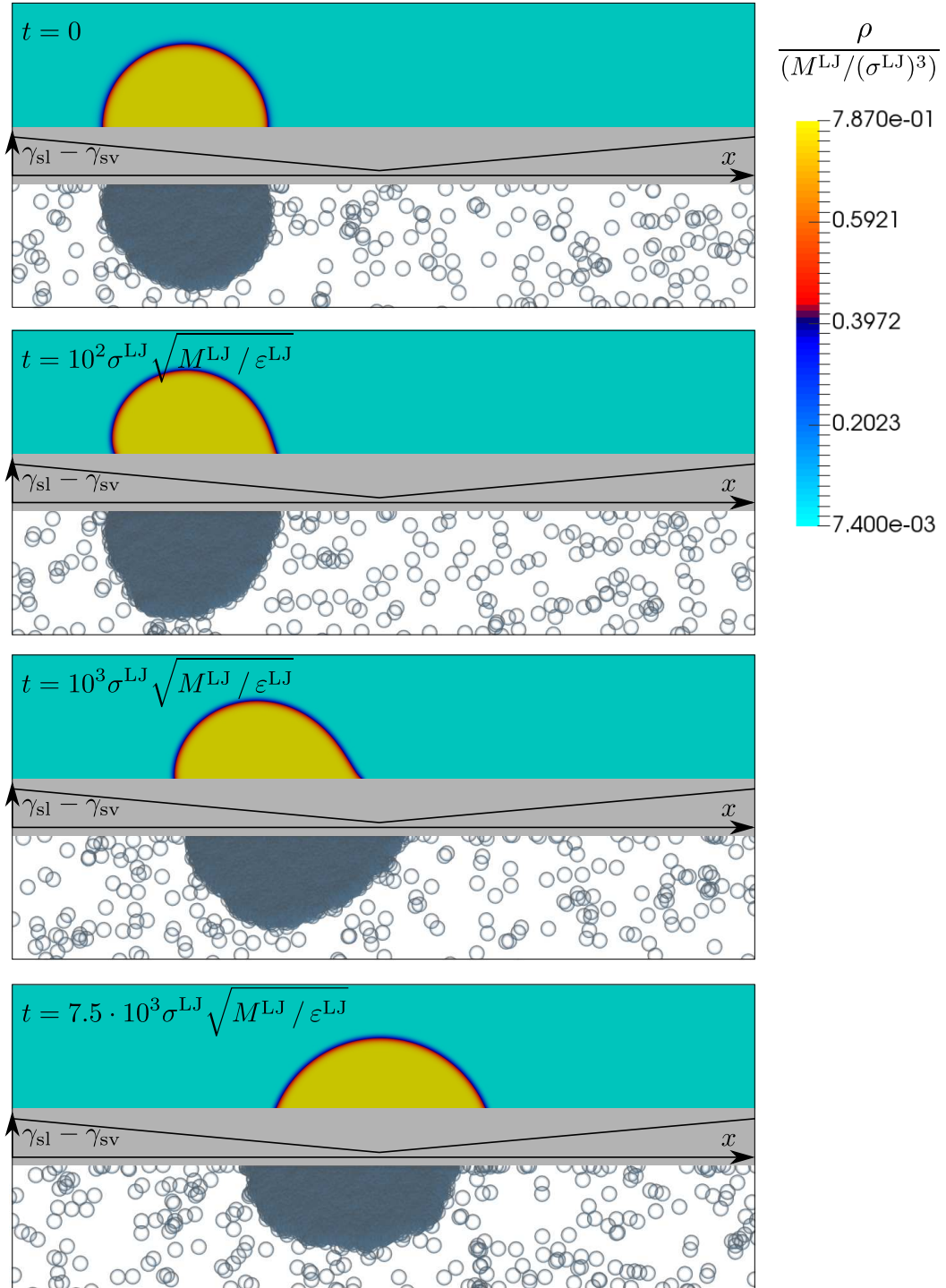


Figure 6.14: Droplet on surface with wettability gradient. Snapshots of the PF and (mirrored) MD simulation for the first scenario. The first plot shows the initialization state and the last plot the static equilibrium configuration. [Diewald et al. 2020a]

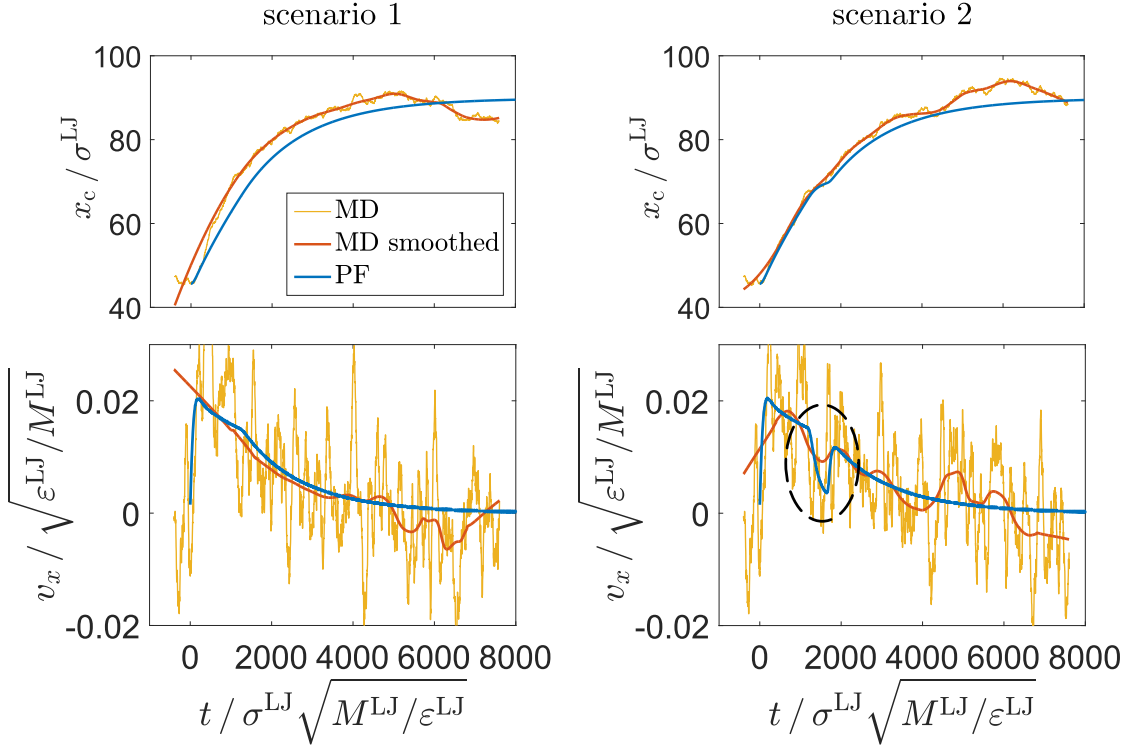


Figure 6.15: Droplet on surface with wettability gradient. MD and PF results for the temporal evolution of the centroid and the velocity in x -direction. [Diewald et al. 2020a]

a roughly constant velocity, cf. $t \in [200, 1400] \sigma^{LJ} \sqrt{M^{LJ} / \epsilon^{LJ}}$. This implies that an equilibrium between the driving force originating from the wettability gradient and forces originating from the viscous stresses is established. The next change in the motion of the droplet is observed after the right side of the droplet passes over the middle of the solid surface, cf. $t \in [1400, 8000] \sigma^{LJ} \sqrt{M^{LJ} / \epsilon^{LJ}}$. The sign of the wettability gradient changes in the middle of the solid surface. The difference between the values for $\gamma_{sl} - \gamma_{sv}$ at the left and right side of the droplet decreases. The resulting reduction of the driving force leads to a deceleration of the droplet. Once the center of the droplet is in the middle of the solid surface, the values for $\gamma_{sl} - \gamma_{sv}$ are the same for the left and right side of the droplet. Thus, the driving force fades and a static equilibrium is reached.

In the second scenario, the overall droplet behavior is similar to the first scenario. However, one main difference is observed. Once the right side of the droplet reaches the barrier that is imposed by the discontinuous change of the wettability, it is decelerated significantly, cf. $t \approx 1600 \sigma^{LJ} \sqrt{M^{LJ} / \epsilon^{LJ}}$ and dashed oval in Figure 6.15.

The right side of the droplet is able to overcome the barrier. After this, the barrier has no influence on the motion of the droplet. It reassumes speed and shows a similar behavior to the first scenario. The immediacy of regaining speed reveals that the motion of the droplet is mainly influenced by the interplay of the surface tensions and the viscous stresses. The effects of inertia play a minor role which is typical for the nanoscale.

Comparing the PF to the MD results, three main deviations are found:

1. The MD simulations show a faster droplet acceleration.
2. The last time steps of the MD simulation do not show a fully stationary droplet.
3. The deceleration of the droplet at the barrier of the second scenario is smaller in the MD simulations.

The first deviation can be explained by the non-homogeneous distribution of the vapor density in the MD simulations that is caused by an adsorption of particles at the solid surface. Such adsorption effects are not included in the PF model. The second and third deviation can be explained by the stochastic character of the MD simulations. Small imbalances of the contact angles on the left and right side of the droplet as well as the aforementioned density inhomogeneities disturb the equilibrium and lead to a scattering of the droplet around the equilibrium state. This stochastic behavior does also facilitate the overcoming of the barrier.

Apart from the mentioned deviations, the PF and MD results show very good qualitative and quantitative agreement for both scenarios. While the fluctuations of the MD simulations are clearly visible in the raw MD data, the smoothed representation of the MD data is well in line with the PF results. To learn more about the influence of temperature on the results see [Diewald et al. 2020a].

The results of this section validate the dynamics of the Navier-Stokes-Korteweg model with the EoS based Helmholtz free energy on the nanoscale. The viscosity correlation that is derived in section 4.3 is applicable for the LJTS fluid.

6.3.3 Semi-Implicit Time Integration Scheme

This section investigates the properties of the newly developed semi-implicit energy stable time integration scheme, cf. section 5.1.2. For this, two basic scenarios are regarded. The first scenario initializes the computational domain with an oval droplet. The second scenario shows a falling droplet. The results are also shown in [Diewald et al. 2020b].

For both scenarios the computational domain is a square with edge lengths $20 \sigma^{\text{LJ}}$ that is discretized by 128 elements across each edge. The initial velocity in all of \mathcal{B} and the temperature are $\vec{v}^0 = \vec{0}$ and $T = 0.7 \frac{\varepsilon^{\text{LJ}}}{k_{\text{B}}}$. The simulations are performed using the backward Euler (BE) as well as the semi-implicit (SI) time integration scheme and different time step sizes. In each time step, the energy of the computational domain is computed according to

$$E^n = \int_{\mathcal{B}} \left[\rho^n a^{\text{PeTS}}(\rho^n) + \frac{1}{2} \kappa |\nabla \rho^n|^2 + \frac{1}{2} \rho^n |\vec{v}^n|^2 + g x_g \rho^n \right] dV + \int_{\partial \mathcal{B}_s} (\gamma_{\text{sl}} - \gamma_{\text{sv}}) h(\rho^n) dA. \quad (6.10)$$

To improve stability, the interpolation function $h(\rho)$ is set to $h(\rho) = 0$ for $\rho < \rho''$ and $h(\rho) = 1$ for $\rho > \rho'$.

Oval Droplet Initialization

The density distribution for the oval droplet initialization is shown in the first contour plot of Figure 6.16 (a). From this initialization state the simulations are performed using the BE and the SI time integration scheme with the time step sizes

$$\Delta t \in \{10^0, 10^{-1}, 10^{-2}\} \sigma^{\text{LJ}} \sqrt{M^{\text{LJ}}/\varepsilon^{\text{LJ}}}. \quad (6.11)$$

The stabilization parameter for the SI time integration scheme is set in accordance with the value found in section 5.1.2, i.e. $\beta^{\text{s}} = 50 \frac{\varepsilon^{\text{LJ}}(\sigma^{\text{LJ}})^3}{(M^{\text{LJ}})^2}$. In addition, the SI simulations with $\Delta t = 10^{-1} \sigma^{\text{LJ}} \sqrt{M^{\text{LJ}}/\varepsilon^{\text{LJ}}}$ are also performed for

$$\beta^{\text{s}} \in \{12.5, 25, 100\} \frac{\varepsilon^{\text{LJ}}(\sigma^{\text{LJ}})^3}{(M^{\text{LJ}})^2}. \quad (6.12)$$

Gravitational effects are neglected.

Figure 6.16 (a) shows the temporal evolution of the droplet for the SI time integration scheme with $\Delta t = 10^{-2} \sigma^{\text{LJ}} \sqrt{M^{\text{LJ}}/\varepsilon^{\text{LJ}}}$ and $\beta^{\text{s}} = 50 \frac{\varepsilon^{\text{LJ}}(\sigma^{\text{LJ}})^3}{(M^{\text{LJ}})^2}$. During the simulations the oval initialization evolves to a round droplet, which reduces the energy of the computational domain.

Figure 6.16 (b) shows the energy of the computational domain, cf. (6.10), at different times t for the BE and SI simulations with different time step sizes and $\beta^{\text{s}} = 50 \frac{\varepsilon^{\text{LJ}}(\sigma^{\text{LJ}})^3}{(M^{\text{LJ}})^2}$. The solid lines show the BE results and the dashed lines the SI results. The colors indicate the time step size. The BE results show a very small time step dependency of the energy decrease, i.e. the curves are lying almost on top of each other. The SI results show that the decrease of energy is slowed down

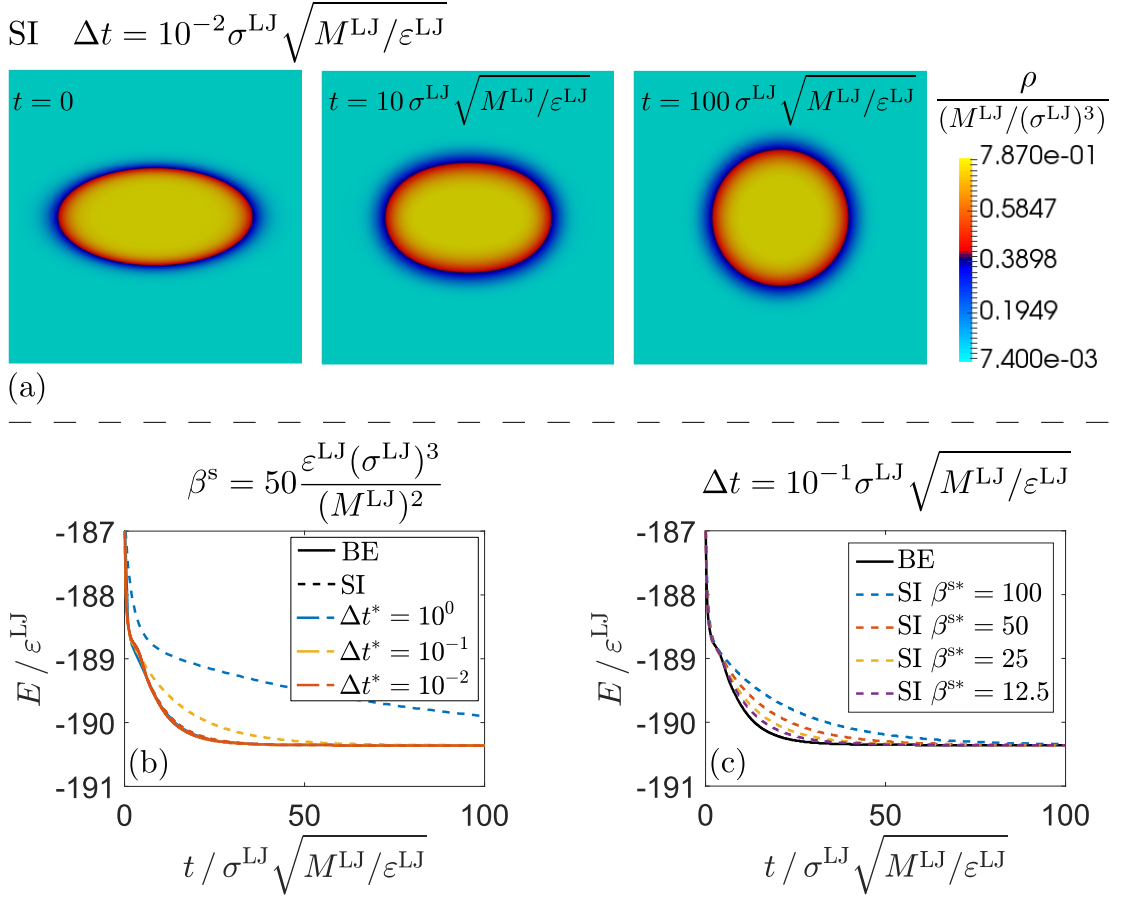


Figure 6.16: Oval droplet initialization. (a): Contour plots of ρ at different times t for the SI scheme with $\Delta t = 10^{-2} \sigma^{\text{LJ}} \sqrt{M^{\text{LJ}}/\varepsilon^{\text{LJ}}}$. (b): Energy evolution of the BE and SI scheme with different time step sizes. The solid lines show the BE results and the dashed lines the SI results. The colors indicate the time step size. The curves for the BE results are lying almost on top of each other. (c): Energy evolution of the SI scheme with different values for the stabilization parameter. [Diewald et al. 2020b]

for rising time step sizes. The larger the time step the longer it takes for the droplet to evolve to a round topology. For small time steps the temporal evolution of the SI simulations is identical to the BE simulations, cf. $\Delta t = 10^{-2} \sigma^{\text{LJ}} \sqrt{M^{\text{LJ}}/\varepsilon^{\text{LJ}}}$.

Figure 6.16 (c) shows the energy of the computational domain at different times t for the SI simulations with different values for the stabilization parameter and $\Delta t = 10^{-1} \sigma^{\text{LJ}} \sqrt{M^{\text{LJ}}/\varepsilon^{\text{LJ}}}$. Additionally, the BE results for the same time step size are plotted for reference. The slowing of the droplet evolution is not only found

for an increase of the time step size but also for an increase of the stabilization parameter.

The slowing of the temporal evolution for large values of the time step size or the stabilization parameter was first revealed by Xu et al. [2017] for a similar scheme. It is therefore the expected behavior.

Falling Droplet

For the falling droplet scenario, the gravitational acceleration is set to $g = 0.1 \frac{\varepsilon^{\text{LJ}}}{M^{\text{LJ}} \sigma^{\text{LJ}}}$. On the surface at the bottom of the computational domain, the surface tensions are set to $\gamma_{\text{sv}} - \gamma_{\text{sl}} = 0.412 \frac{\varepsilon^{\text{LJ}}}{(\sigma^{\text{LJ}})^2}$ which yields a theoretical contact angle of $\Theta = 45^\circ$. The initialization state is shown in the first contour plot of Figure 6.17 (a). From this initialization state the simulations are performed using the BE and the SI time integration scheme with the time step sizes

$$\Delta t \in \{10^1, 10^0, 10^{-1}, 10^{-2}\} \sigma^{\text{LJ}} \sqrt{M^{\text{LJ}}/\varepsilon^{\text{LJ}}}. \quad (6.13)$$

The stabilization parameters for the SI time integration scheme are set in accordance with the values found in section 5.1.2, i.e. $\beta^{\text{s}} = 50 \frac{\varepsilon^{\text{LJ}} (\sigma^{\text{LJ}})^3}{(M^{\text{LJ}})^2}$ and $\alpha^{\text{s}} = -5 \frac{(\sigma^{\text{LJ}})^6}{(M^{\text{LJ}})^2}$.

Figure 6.17 (a) shows the early temporal evolution of the droplet for the SI time integration scheme with $\Delta t = 10^{-2} \sigma^{\text{LJ}} \sqrt{M^{\text{LJ}}/\varepsilon^{\text{LJ}}}$. During the simulations the droplet falls onto the surface. After the impact, the contact angle evolves and the droplet starts to spread.

Figure 6.17 (b) shows the early temporal evolution of the droplet for the SI time integration scheme with $\Delta t = 10^1 \sigma^{\text{LJ}} \sqrt{M^{\text{LJ}}/\varepsilon^{\text{LJ}}}$. Comparing the contour plots of the SI simulations for $\Delta t = 10^{-2} \sigma^{\text{LJ}} \sqrt{M^{\text{LJ}}/\varepsilon^{\text{LJ}}}$ and $\Delta t = 10^1 \sigma^{\text{LJ}} \sqrt{M^{\text{LJ}}/\varepsilon^{\text{LJ}}}$ reveals that large time step sizes can lead to the evolution of alternative equilibria.

Figure 6.17 (c) shows the energy of the computational domain at different times t for the BE and SI simulations with different time step sizes. The solid lines show the BE results and the dashed lines the SI results. The colors indicate the time step size. For the BE simulations with the two largest time step sizes, the Newton-Raphson method does not converge. The crosses mark their termination point. The BE results for the remaining time step sizes do not show a time step size dependency, i.e. the curves are lying almost on top of each other. For the SI simulations, the residuum converges for all time step sizes. The SI time integration scheme can handle time step sizes for which the BE scheme fails. Again, a slowing of the droplet evolution is observed for large time step sizes. Figure 6.17 (d) shows the energy evolution of the SI simulations with the two largest time steps up to $t = 1000 \sigma^{\text{LJ}} \sqrt{M^{\text{LJ}}/\varepsilon^{\text{LJ}}}$. Despite the slowing, the simulations with the

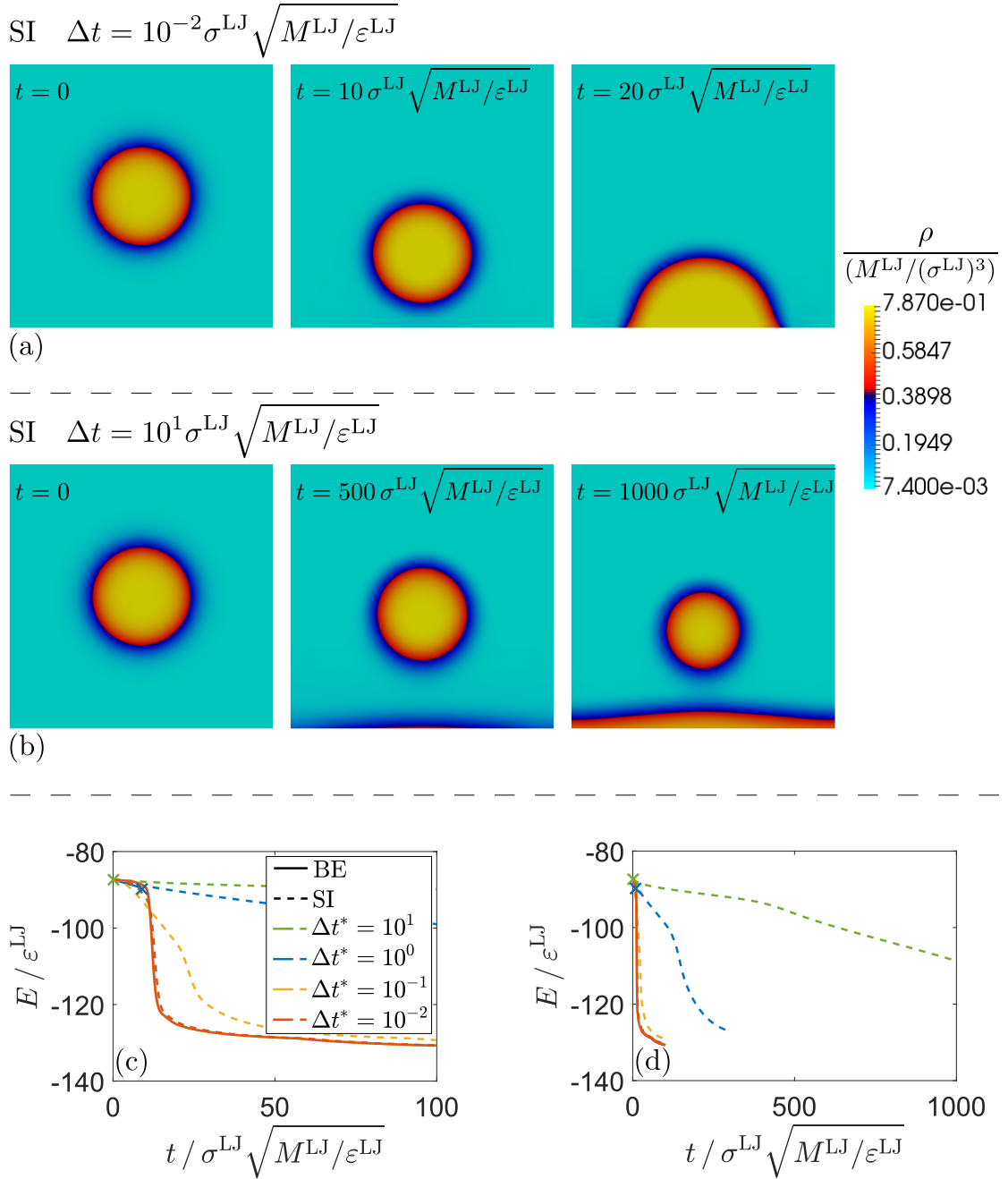


Figure 6.17: Falling droplet. (a, b): Contour plots of ρ at different times t for the SI scheme with $\Delta t = 10^{-2} \sigma^{\text{LJ}} \sqrt{M^{\text{LJ}}/\varepsilon^{\text{LJ}}}$ (a) and $\Delta t = 10^1 \sigma^{\text{LJ}} \sqrt{M^{\text{LJ}}/\varepsilon^{\text{LJ}}}$ (b). (c, d): Energy evolution of the BE and SI scheme with different time step sizes up to $t = 100 \sigma^{\text{LJ}} \sqrt{M^{\text{LJ}}/\varepsilon^{\text{LJ}}}$ (c) and for the SI simulations with the two largest time step sizes up to $t = 1000 \sigma^{\text{LJ}} \sqrt{M^{\text{LJ}}/\varepsilon^{\text{LJ}}}$ (d). The solid lines show the BE results and the dashed lines the SI results. The colors indicate the time step size. The crosses mark the termination point of the simulations for which the Newton-Raphson method does not converge. [Diewald et al. 2020b]

large time step sizes do eventually converge towards the minimum of the other simulations.

The oval droplet initialization scenario and the falling droplet scenario reveal the properties of the newly developed semi-implicit energy stable time integration scheme. The SI scheme shows some artificial properties as the slowing and the evolution of alternative equilibria for large time step sizes and large values of the stabilization parameter. However, the SI scheme does also possess some advantageous and interesting properties that the BE scheme does not have. It shows convergence of the residuum for very large time step sizes for which the BE scheme fails. Thus, the SI scheme is more robust. Even if large time step sizes are avoided in order to suppress the artificial properties and the same time step size is chosen for the BE and SI scheme, the SI scheme still has the advantage of leading to a linear system of equations. This brings large benefits with respect to the computational effort. As predicted by the proof in section 5.1.2 the SI scheme dissipates energy independent of the time step size.

7 Scale Bridging

The PF results obtained with the EoS based Helmholtz free energy agree well with MD results. Thus, the PF model properly describes the underlying physics on the nanoscale. The computational effort for the PF simulations is smaller than for the MD simulations. The gain in computational efficiency by itself does already qualify the PF model to compute larger scenarios. However, since the FE mesh used for the PF simulations needs to resolve the nanoscale width of the liquid-vapor interface, the PF simulations are still tied to small scales. To achieve a true scale bridging from the nano- to the microscale, the liquid-vapor interface needs to be artificially widened. The resulting EoS based and scaled PF model serves as an important link between the nanoscale approach of molecular simulations with a strong physical validity and the purely phenomenological approach of classical PF models.

Special care has to be taken not to violate the physical foundation of the EoS based PF model when introducing the widening. The approach is presented in the following. Subsequently, a numerical example for methane is given.

7.1 Adaption of the Equation of State Based Helmholtz Free Energy

The EoS based Helmholtz free energy shall be adapted such that the liquid-vapor interface can be widened without altering other properties of the interface or the bulk phases. This is achieved by introducing two parameters to the formulation of the EoS based Helmholtz free energy density. The first parameter α^{scal} scales the homogeneous excess free energy density ω , cf. (4.31), only. The Helmholtz free energy densities for ρ' and ρ'' remain unaltered. The second parameter β^{scal} scales the density gradient dependent part of the Helmholtz free energy density. The

scaled EoS based Helmholtz free energy density reads

$$\begin{aligned}\rho\hat{\psi}(\rho, \nabla\rho) &= \rho\psi^{\text{scal}}(\rho, \nabla\rho) \\ &= \alpha^{\text{scal}} \underbrace{(\rho a^{\text{PeTS}}(\rho) - \mu'\rho + p^{\text{h}})}_{\omega(\rho)} + \mu'\rho - p^{\text{h}} + \frac{1}{2}\beta^{\text{scal}}|\nabla\rho|^2.\end{aligned}\quad (7.1)$$

Analogous to the procedure for the empirical Helmholtz free energy density, cf. section 4.1, the two parameters α^{scal} and β^{scal} are used to define the width and the energy of the liquid-vapor interface. Figure 7.1 shows plots of the local part of the Helmholtz free energy density and the homogeneous excess free energy density for different values of α^{scal} . The thicker black lines show the original curves without scaling, i.e. $\alpha^{\text{scal}} = 1$. They are identical to the plots shown in Figure 4.4.

It is important to verify that the scaling does not change crucial properties of the local part of the Helmholtz free energy density. The bulk densities ρ' and ρ'' of a static equilibrium configuration with a planar interface remain unaltered since

$$\begin{aligned}\left.\frac{\partial(\rho\psi^{\text{scal}}(\rho, \nabla\rho))}{\partial\rho}\right|_{\rho\in\{\rho', \rho''\}} &= \alpha^{\text{scal}} \underbrace{\left(\left.\frac{\partial(\rho a^{\text{PeTS}}(\rho))}{\partial\rho}\right|_{\rho\in\{\rho', \rho''\}} - \mu'\right)}_{=0} + \mu' \\ &= \mu',\end{aligned}\quad (7.2)$$

which is the identical result as for the original EoS based Helmholtz free energy density. Furthermore, since

$$\frac{\partial^2(\rho\psi^{\text{scal}}(\rho, \nabla\rho))}{\partial\rho^2} = \alpha^{\text{scal}} \frac{\partial^2(\rho a^{\text{PeTS}}(\rho))}{\partial\rho^2},\quad (7.3)$$

the densities, for which the second derivative of the Helmholtz free energy density with respect to density is zero, are also not affected by the scaling and the boundaries of the unstable region are equally unaltered.

The computation of the parameters α^{scal} and β^{scal} , such that the interface can be widened without altering the surface tension, is presented in the following. The underlying idea was shown in [Cahn and Hilliard 1958]. Analogous to section 4.1, a planar interface, that is perpendicular to an axis x and is located at $x = 0$, is regarded. Gravitational effects are neglected ($g = 0$).

The excess free energy Ω^{scal} , which is the energy that is stored in that interface, is given by

$$\Omega^{\text{scal}} = A \int_{-\infty}^{\infty} \left[\alpha^{\text{scal}}\omega(\rho) + \frac{1}{2}\beta^{\text{scal}}|\nabla\rho|^2 \right] dx.\quad (7.4)$$

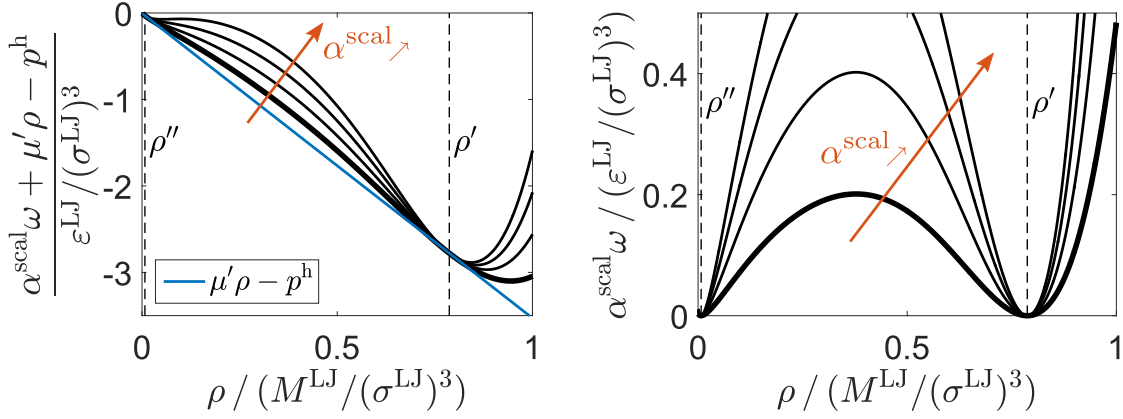


Figure 7.1: Left: Plot of the local part of the EoS based and scaled Helmholtz free energy density for different values of α^{scal} and $T = 0.7 \frac{\varepsilon^{\text{LJ}}}{k_{\text{B}}}$. Right: Plot of the scaled homogeneous excess free energy density. The scaling does not alter the Helmholtz free energy densities for ρ' and ρ'' .

The requirement regarding the energy or surface tension of the interface states that Ω^{scal} has to be equal to the surface tension between the liquid and the vapor phase γ_{lv} multiplied with the surface area of the interface A ,

$$\Omega^{\text{scal}} = A\gamma_{\text{lv}}. \quad (7.5)$$

The width of the interface shall be defined by l^{scal} ,

$$\left. \frac{d\rho}{dx} \right|_{x=0} = \frac{\rho' - \rho''}{l^{\text{scal}}}. \quad (7.6)$$

Reusing (4.11) and writing (4.35–4.38) for the scaled EoS based Helmholtz free energy (7.1) gives

$$\alpha^{\text{scal}} (\rho a^{\text{PeTS}}(\rho) - \mu' \rho + p^{\text{h}}) = \frac{1}{2} \beta^{\text{scal}} |\nabla \rho|^2 \quad \text{or} \quad \alpha^{\text{scal}} \omega(\rho) = \frac{1}{2} \beta^{\text{scal}} |\nabla \rho|^2. \quad (7.7)$$

With this the energy requirement can be written as

$$\int_{-\infty}^{\infty} \left[\alpha^{\text{scal}} \omega(\rho) + \frac{1}{2} \beta^{\text{scal}} |\nabla \rho|^2 \right] dx = \int_{-\infty}^{\infty} 2\alpha^{\text{scal}} \omega(\rho) dx = \gamma_{\text{lv}}. \quad (7.8)$$

Using

$$dx = \sqrt{\frac{\beta^{\text{scal}}}{2\alpha^{\text{scal}} \omega(\rho)}} d\rho, \quad (7.9)$$

cf. (7.7), the integral over x can be rewritten as an integral over ρ

$$\int_{-\infty}^{\infty} 2\alpha^{\text{scal}}\omega(\rho) dx = \int_{\rho''}^{\rho'} \sqrt{2\alpha^{\text{scal}}\beta^{\text{scal}}\omega(\rho)} d\rho = \gamma_{\text{lv}}. \quad (7.10)$$

Employing (7.9) in the requirement for the width of the interface as stated in (7.6) yields

$$\left. \frac{d\rho}{dx} \right|_{x=0} = \sqrt{\frac{2\alpha^{\text{scal}}\omega(\rho = \frac{\rho' + \rho''}{2})}{\beta^{\text{scal}}}} = \frac{\rho' - \rho''}{l^{\text{scal}}}. \quad (7.11)$$

Now, α^{scal} and β^{scal} can be determined by solving (7.10) and (7.11),

$$\alpha^{\text{scal}} = c_1^{\text{scal}} \frac{\gamma_{\text{lv}}}{l^{\text{scal}}} \quad \text{with} \quad c_1^{\text{scal}} = \frac{\rho' - \rho''}{2\sqrt{\omega(\rho = \frac{\rho' + \rho''}{2})} \int_{\rho''}^{\rho'} \sqrt{\omega(\rho)} d\rho},$$

$$\beta^{\text{scal}} = c_2^{\text{scal}} \gamma_{\text{lv}} l^{\text{scal}} \quad \text{with} \quad c_2^{\text{scal}} = \frac{\sqrt{\omega(\rho = \frac{\rho' + \rho''}{2})}}{(\rho' - \rho'') \int_{\rho''}^{\rho'} \sqrt{\omega(\rho)} d\rho}. \quad (7.12)$$

The constants c_1^{scal} and c_2^{scal} depend on the temperature, only. They are computed previous to the actual simulations by means of numerical integration. The EoS based and scaled Helmholtz free energy density reads

$$\rho\psi^{\text{scal}}(\rho, \nabla\rho) = c_1^{\text{scal}} \frac{\gamma_{\text{lv}}}{l^{\text{scal}}} (\rho a^{\text{PeTS}}(\rho) - \mu'\rho + p^{\text{h}}) + \mu'\rho - p^{\text{h}} + \frac{1}{2}c_2^{\text{scal}} \gamma_{\text{lv}} l^{\text{scal}} |\nabla\rho|^2. \quad (7.13)$$

It shall be mentioned that the sharp PF method [Finel et al. 2018] presents a way of resolving the PF interface with one grid point. However, the required adaptation of the Helmholtz free energy density would weaken the physical validity. The sharp PF method is therefore not used in the present work.

7.2 Droplet on Tilted Surface with Wettability Gradient

To give an example by means of a specific substance, the scale dependent dynamic behavior of a methane droplet on a tilted surface with a wettability gradient is investigated. For methane, the energy and size parameter of the LJ potential are given by $\varepsilon^{\text{LJ}} = 2.417 \cdot 10^{-21}$ J and $\sigma^{\text{LJ}} = 3.724 \cdot 10^{-10}$ m [Vrabec et al. 2006]. The mass per particle is $M^{\text{LJ}} = 2.664 \cdot 10^{-26}$ kg [Kurzweil and Scheipers 2012].

Analogous to section 6.3.2 the wettability gradient is characterized by a change of $\gamma_{sl} - \gamma_{sv}$ along the x -axis and causes a difference in the contact angles on the left and right side of the droplet. The maximum and minimum values of $\gamma_{sl} - \gamma_{sv}$ are chosen such that they correspond to theoretical contact angles of $\Theta = 150^\circ$ and $\Theta = 30^\circ$, respectively. A sketch of the scenario is shown in Figure 7.2. In contrast to the scenarios studied in section 6.3.2 the surface is tilted by 45° and gravity ($g = 9.81 \frac{\text{m}}{\text{s}^2}$) is applied.

To investigate how the droplet behavior depends on the length scale, all spatial dimensions are scaled by the scaling parameters p^{scal} for which different values are chosen

$$p^{\text{scal}} \in \{10^0, 10^1, 10^2, 10^3\}. \quad (7.14)$$

The computational domain is a rectangle of size $180 \sigma^{\text{LJ}} p^{\text{scal}} \approx 6.703 \cdot 10^{-8} \text{ m } p^{\text{scal}}$ in x -direction and $30 \sigma^{\text{LJ}} p^{\text{scal}} \approx 1.117 \cdot 10^{-8} \text{ m } p^{\text{scal}}$ in y -direction. This rectangle is discretized by 384×64 elements. The initial velocity in all of \mathcal{B} and the temperature are $\vec{v}^0 = \vec{0}$ and $T = 0.7 \frac{\varepsilon^{\text{LJ}}}{k_{\text{B}}} \approx 122.542 \text{ K}$. For the specific surface tension values that correspond to the contact angles of $\Theta = 150^\circ$ and $\Theta = 30^\circ$ at this temperature, see section 6.3.2. The backward Euler time integration scheme with varying time step sizes for the different values of p^{scal} is used. The initialization sets a hemispherical droplet with radius $r_{\text{ini}} = 20 \sigma^{\text{LJ}} p^{\text{scal}} \approx 7.448 \cdot 10^{-9} \text{ m } p^{\text{scal}}$ on the bottom of the computational domain, such that the distance between the center of the droplet and left end of the computational domain in x -direction is $90 \sigma^{\text{LJ}} p^{\text{scal}} \approx 3.352 \cdot 10^{-8} \text{ m } p^{\text{scal}}$, i.e. in the middle of the domain,

$$\rho^0(r) = \frac{\rho' - \rho''}{2} \left[\tanh \left(\frac{-2(r - r_{\text{ini}})}{l^{\text{scal}}} \right) + 1 \right] + \rho'', \quad (7.15)$$

where r denotes the distance to the center of the droplet. The interface width is set to $l^{\text{scal}} = 2l_{\text{pF}}^{\text{t}} p^{\text{scal}} \approx 1.521 \cdot 10^{-9} \text{ m } p^{\text{scal}}$ and the surface tension γ_{lv} is set in accordance with the value found in section 6.2.2. The position of the centroid in x -direction x_c is computed in each time step according to (6.9). Therefrom, the droplet velocity in x -direction v_x is evaluated. As a consequence of the initialization, the position of the centroid in x -direction for $t = 0$ is $x_c^0 = 90 \sigma^{\text{LJ}} p^{\text{scal}} \approx 3.352 \cdot 10^{-8} \text{ m } p^{\text{scal}}$.

Figure 7.3 shows the droplet velocity v_x over the relative droplet position $\frac{x_c}{x_c^0}$ for the different values of p^{scal} . The nanoscale droplet with $p^{\text{scal}} = 10^0$ reaches the highest absolute velocity value of all simulations. This velocity of $v_x \approx -3.72 \frac{\text{m}}{\text{s}} \approx -0.0124 \sqrt{\varepsilon^{\text{LJ}}/M^{\text{LJ}}}$ is reached very early during the evolution when the droplet is still close to its initialization position. The rapid acceleration with a subsequent slow deceleration is well in line with the result for the nanoscale droplet on a surface with wettability gradient from section 6.3.2, cf. Figure 6.15. The highest absolute

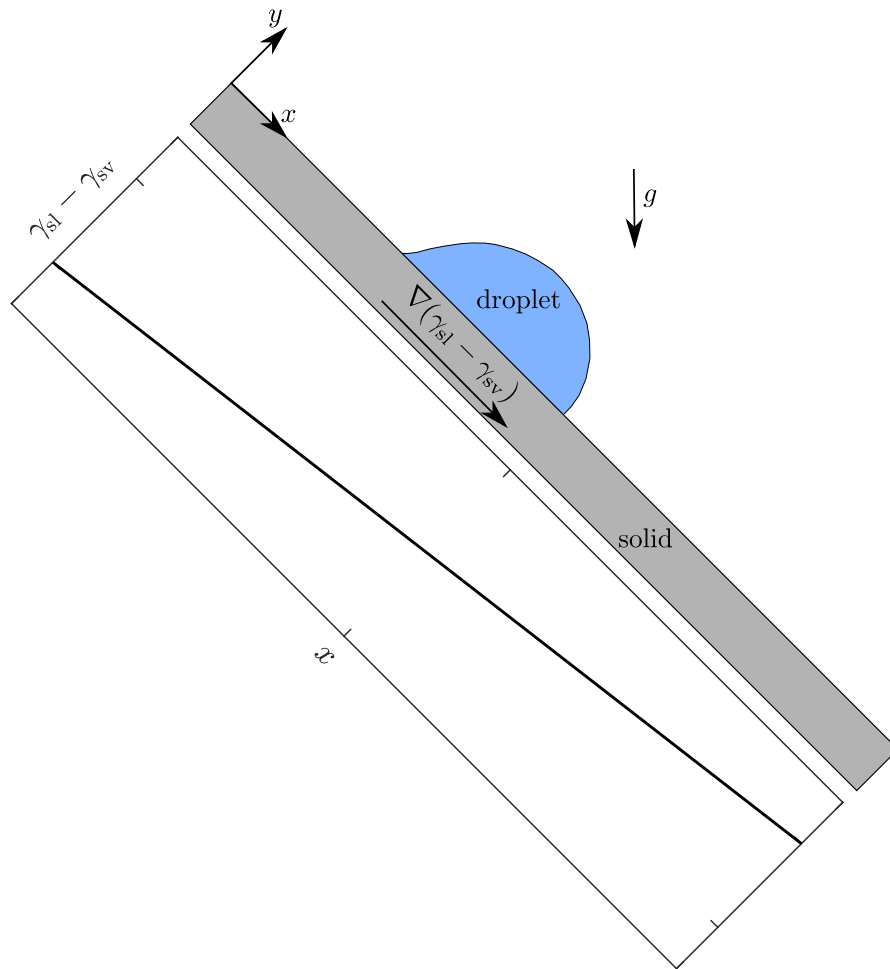


Figure 7.2: Sketch of methane droplet on tilted surface with wettability gradient.

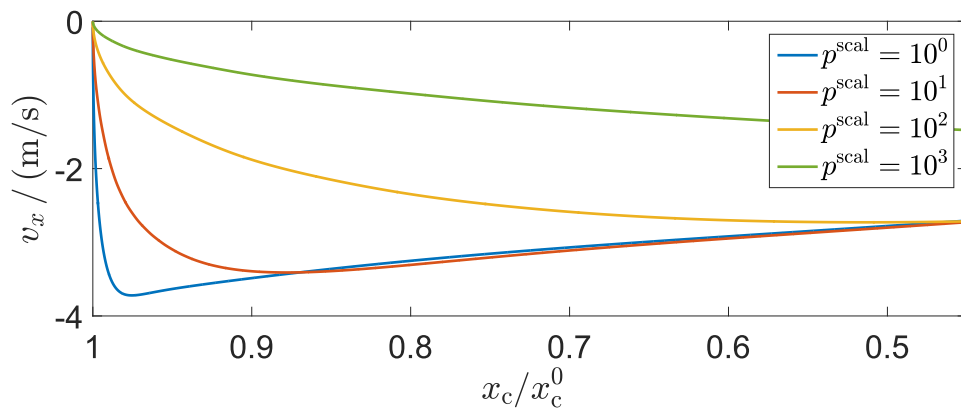


Figure 7.3: Methane droplet on tilted surface with wettability gradient. Velocity over relative position for different values of p^{scal} .

velocity value of the present example is smaller than the one in section 6.3.2 where it was $v_x \approx 0.0203\sqrt{\varepsilon^{\text{LJ}}/M^{\text{LJ}}}$. This is easily explained by the fact that the velocity gradient is only half as steep in the present example.

The results for the other values of p^{scal} show that a rise of the scaling parameter p^{scal} is accompanied by a decrease of the highest absolute velocity value. The simulation with $p^{\text{scal}} = 10^1$ does still show the same characteristics as the simulation with $p^{\text{scal}} = 10^0$. That is, a rapid acceleration with a subsequent slow deceleration. For $p^{\text{scal}} = 10^2$ and $p^{\text{scal}} = 10^3$, the influence of inertia is growing and the droplets show a significantly slower acceleration. The droplet for $p^{\text{scal}} = 10^2$ reaches its velocity with the highest absolute value just before arriving at the end of the computational domain. The droplet for $p^{\text{scal}} = 10^3$ is still accelerating when it reaches the end of the computational domain.

For $p^{\text{scal}} = 10^3$ the initialization radius of the droplet is $r_{\text{ini}} \approx 7.448 \cdot 10^{-6}$ m. Evidently, this simulation represents a scenario on the microscale. This example demonstrates how the PF model of this work can be used to bridge the gap between molecular models on the nanoscale and phenomenological models on the macroscale. The PF model inherits the information on the behavior of the fluid from nanoscale MD simulations and carries this strong physical foundation to the microscale.

8 Conclusion and Outlook

The derivation, implementation, and validation of a PF model, that is capable of simulating dynamic and static wetting scenarios in a precise and reliable manner, is presented in this work. The rational derivation utilizes the balance laws and the Coleman-Noll procedure yielding a model that is not fluid specific and serves as a common ground. From this dynamic Navier-Stokes-Korteweg model the static Allen-Cahn model is derived. This approach gives a coherent representation of the different models of this work as they originate from the same derivation.

The general model is made fluid specific by introducing different formulations of the Helmholtz free energy and a viscosity correlation. The formulations of the Helmholtz free energy include an empirically motivated Helmholtz free energy and an EoS based Helmholtz free energy. The empirical Helmholtz free energy allows to freely adjust parameters like the surface tension or the width of the interface between the liquid and the vapor phase leading to a very flexible model. The EoS based Helmholtz free energy utilized the PeTS EoS for the LJTS fluid. It does not include parameters that can be freely adjusted. Fluid properties like the surface tension or the width of the liquid-vapor interface are inherent in the formulation and represent the physical behavior of the LJTS fluid. The LJTS fluid together with the PeTS EoS is chosen to give an example on how the general PF model can be adapted to simulate a specific physical fluid. The approach can easily be repeated for other fluids.

The FE implementation of the models facilitates the exchange of the EoS, and thereby the specific fluid, under consideration. A straightforward exchangeability is achieved by employing the concept of hyper-dual numbers which allow for an exact and step size independent numerical differentiation of the Helmholtz free energy. Further characteristics of the implementation include a mixed Q2P1 formulation and a newly developed semi-implicit energy stable time integration scheme.

The numerical examples demonstrate that the model with the empirical Helmholtz free energy can reproduce basic wetting configurations. A variety of PF results

obtained with the EoS based Helmholtz free energy are compared to MD simulations of the same scenarios. Both, the static as well as the dynamic properties of the PF results are found to be in good agreement with the MD results. This validates the PF model on the nanoscale. The presented post-processing of eigenvalues and eigenvectors for static wetting configurations can be used to determine the stability of the found solution. This approach can also be helpful for other PF models that use the first order optimality condition of an energy functional for the determination of static equilibria. The semi-implicit time integration scheme shows convergence of the residuum for very large time step sizes, is energy stable, and yields a linear system of equations which is favorable with regard to the numerical effort. It also possesses some artificial properties, e.g. a slowing of the temporal evolution.

With its strong nanoscale foundation, the PF model of this work can bridge the gap between the precise but numerically costly molecular models on the nanoscale and the solely phenomenological continuum models on the macroscale. The scale bridging is enabled by the lower computational effort of the PF simulations compared to MD simulations and also by an artificial widening of the liquid-vapor interface.

Worthwhile extensions of the presented model could include a more elaborate modeling of the solid surface. This could include a description of the surface by means of a solid mechanics continuum model which would need to be coupled with the fluid model of this work. This coupling would include the challenge of combining the Eulerian type description of the fluid with a Lagrangian type description of the solid surface. The modeling of the solid surface could also be enhanced by including the influence of the solid surface on fluid particles that are not in contact, but are located in the vicinity of the solid surface. By extending the range of the solid fluid interaction, effects like adsorption could be included into the model. A MD study of adsorption of the LJTS fluid that could be used to gain reference data is presented in [Heier et al. 2019]. To investigate the effects of possible line tensions on the wetting behavior, these could be included into the formulation of the model. Such an extension seems straightforward as it could be achieved by including a density gradient dependent term in the formulation of the surface energy density.

The work of Jamet et al. [2002] reports on the existence and elimination of parasitic currents for the dynamic Navier-Stokes-Korteweg model. Such artificial effects have also been found for the model of this work, see [Bilz 2018], and could be investigated in more detail.

From a numerical perspective, the utilization of isogeometric analysis (IGA) [Hug-

hes et al. 2005] would be an appealing modification of the implementation as it would eliminate the need for a mixed formulation. IGA has successfully been applied for dynamic Navier-Stokes-Korteweg models by Gomez et al. [2010] and Liu et al. [2013, 2015]. Regarding the semi-implicit time integration scheme, the development of adaptive time stepping strategies could likely yield further improvement.

In addition to the aforementioned extensions, the model of this work can also be used in its current form for future investigations of a variety of wetting scenarios with a variety of different fluids, provided that an appropriate EoS exists.

A Details of the Continuous Global Energy Dissipation Relation

This section is based on [Diewald et al. 2020b]. First, (3.52) is multiplied with $(\mu + x_g g)$, (3.53) with $\cdot \vec{v}$, and (3.56) with $(-\frac{\partial \rho}{\partial t})$. Thereafter, each equation is integrated over \mathcal{B} . Then, by invoking integration by parts and inserting the boundary conditions (3.58) and (3.59) the following three equations are derived:

- $\int_{\mathcal{B}} (3.52)(\mu + x_g g) \, dV$

$$\int_{\mathcal{B}} \left(\frac{\partial \rho}{\partial t} + \operatorname{div}(\rho \vec{v}) \right) (\mu + x_g g) \, dV = 0 \quad (\text{A.1})$$

- $\int_{\mathcal{B}} (3.53) \cdot \vec{v} \, dV$

$$\begin{aligned} & \int_{\mathcal{B}} \frac{1}{2} \frac{\partial(\rho \vec{v})}{\partial t} \cdot \vec{v} + \frac{1}{2} \rho \frac{\partial \vec{v}}{\partial t} \cdot \vec{v} \, dV \\ &= \int_{\mathcal{B}} \left[-2\eta^v(\rho) \left(\nabla^s \vec{v} - \frac{1}{3} \operatorname{tr}(\nabla^s \vec{v}) \mathbf{1} \right) : \nabla \vec{v} - \nabla \mu \rho \cdot \vec{v} - \rho g \vec{e}_g \cdot \vec{v} \right] \, dV \\ & \stackrel{[\text{Gurtin et al. 2010}]}{=} \int_{\mathcal{B}} \left[-2\eta^v(\rho) \left| \nabla^s \vec{v} - \frac{1}{3} \operatorname{tr}(\nabla^s \vec{v}) \mathbf{1} \right|^2 - \nabla \mu \rho \cdot \vec{v} - \rho g \vec{e}_g \cdot \vec{v} \right] \, dV \end{aligned} \quad (\text{A.2})$$

- $\int_{\mathcal{B}} (3.56) \left(-\frac{\partial \rho}{\partial t} \right) \, dV$

$$\int_{\mathcal{B}} -\mu \frac{\partial \rho}{\partial t} \, dV = \int_{\mathcal{B}} \left[-\frac{\partial(\rho \hat{\psi})}{\partial \rho} \frac{\partial \rho}{\partial t} - \frac{\partial(\rho \hat{\psi})}{\partial \nabla \rho} \cdot \nabla \frac{\partial \rho}{\partial t} \right] \, dV - \int_{\partial \mathcal{B} \cap \partial \mathcal{B}_s} \frac{\partial(\rho \hat{\phi})}{\partial \rho} \frac{\partial \rho}{\partial t} \, dA \quad (\text{A.3})$$

In (A.2) the identity (3.60) and

$$\rho \dot{\vec{v}} = \rho \frac{\partial \vec{v}}{\partial t} + \rho \nabla \vec{v} \vec{v} = \frac{1}{2} \frac{\partial(\rho \vec{v})}{\partial t} + \frac{1}{2} \rho \frac{\partial \vec{v}}{\partial t} + \frac{1}{2} \rho \nabla \vec{v} \vec{v} + \frac{1}{2} \operatorname{div}(\rho \vec{v} \otimes \vec{v}), \quad (\text{A.4})$$

which uses (3.13) are applied. Adding (A.1) and (A.2) gives

$$\begin{aligned} & \int_{\mathcal{B}} \frac{1}{2} \frac{\partial(\rho \vec{v})}{\partial t} \cdot \vec{v} + \frac{1}{2} \rho \frac{\partial \vec{v}}{\partial t} \cdot \vec{v} + \frac{\partial \rho}{\partial t} x_g g \, dV \\ &= \int_{\mathcal{B}} \left[-2\eta^v(\rho) \left| \nabla^s \vec{v} - \frac{1}{3} \operatorname{tr}(\nabla^s \vec{v}) \mathbf{1} \right|^2 - \frac{\partial \rho}{\partial t} \mu \right] dV. \end{aligned} \quad (\text{A.5})$$

Using (A.3) and (A.5) in the first line of (3.62) yields

$$\begin{aligned} \dot{E} &= \int_{\mathcal{B}} \left[\frac{\partial(\rho \hat{\psi})}{\partial t} - 2\eta^v(\rho) \left| \nabla^s \vec{v} - \frac{1}{3} \operatorname{tr}(\nabla^s \vec{v}) \mathbf{1} \right|^2 - \frac{\partial(\rho \hat{\psi})}{\partial \rho} \frac{\partial \rho}{\partial t} - \frac{\partial(\rho \hat{\psi})}{\partial \nabla \rho} \cdot \nabla \frac{\partial \rho}{\partial t} \right] dV \\ &+ \int_{\partial \mathcal{B} \cap \partial \mathcal{B}_s} \left[\frac{\partial(\rho \hat{\phi})}{\partial t} - \frac{\partial(\rho \hat{\phi})}{\partial \rho} \frac{\partial \rho}{\partial t} \right] dA. \end{aligned} \quad (\text{A.6})$$

This leads to the energy dissipation statement of section 3.4.3

$$\dot{E} = \int_{\mathcal{B}} -2\eta^v(\rho) \left| \nabla^s \vec{v} - \frac{1}{3} \operatorname{tr}(\nabla^s \vec{v}) \mathbf{1} \right|^2 dV. \quad (\text{A.7})$$

B Details of the Discrete Global Energy Dissipation Relation

This section is based on [Diewald et al. 2020b]. First, (5.14) is multiplied with $\Delta t(\mu^{n+1} + x_g g)$, (5.15) with $\cdot \Delta t \vec{v}^{n+1}$, and (5.16) with $-(\rho^{n+1} - \rho^n)$. Thereafter, each equation is integrated over \mathcal{B} . Then, by invoking integration by parts and inserting the boundary conditions (5.17), (5.18), and (5.19) the following 3 equations are derived:

- $\int_{\mathcal{B}} (5.14) \Delta t (\mu^{n+1} + x_g g) \, dV$

$$\int_{\mathcal{B}} [\rho^{n+1} - \rho^n + \Delta t \operatorname{div}(\rho^n \vec{v}^{n+1})] [\mu^{n+1} + x_g g] \, dV = 0 \quad (\text{B.1})$$

- $\int_{\mathcal{B}} (5.15) \cdot \Delta t \vec{v}^{n+1} \, dV$

$$\begin{aligned} & \int_{\mathcal{B}} \left[\frac{1}{2} (\rho^n \vec{v}^{n+1} - \rho^{n-1} \vec{v}^n) \cdot \vec{v}^{n+1} + \frac{1}{2} \rho^{n-1} (\vec{v}^{n+1} - \vec{v}^n) \cdot \vec{v}^{n+1} \right] \, dV \\ &= \int_{\mathcal{B}} \left[-\Delta t 2\eta^v(\rho^n) \left(\nabla^s \vec{v}^{n+1} - \frac{1}{3} \operatorname{tr}(\nabla^s \vec{v}^{n+1}) \mathbf{1} \right) : \nabla^s \vec{v}^{n+1} \right. \\ & \quad \left. - \Delta t \rho^n \nabla \mu^{n+1} \cdot \vec{v}^{n+1} - \Delta t \rho^n g \vec{e}_g \cdot \vec{v}^{n+1} \right] \, dV \\ & \stackrel{[\text{Gurtin et al. 2010}]}{=} \int_{\mathcal{B}} \left[-\Delta t 2\eta^v(\rho^n) \left| \nabla^s \vec{v}^{n+1} - \frac{1}{3} \operatorname{tr}(\nabla^s \vec{v}^{n+1}) \mathbf{1} \right|^2 \right. \\ & \quad \left. - \Delta t \rho^n \nabla \mu^{n+1} \cdot \vec{v}^{n+1} - \Delta t \rho^n g \vec{e}_g \cdot \vec{v}^{n+1} \right] \, dV \end{aligned} \quad (\text{B.2})$$

- $\int_{\mathcal{B}} (5.16) (-(\rho^{n+1} - \rho^n)) \, dV$

$$\begin{aligned}
& \int_{\mathcal{B}} -\mu^{n+1} (\rho^{n+1} - \rho^n) \, dV \\
&= \int_{\mathcal{B}} \left[-\beta^s (\rho^{n+1} - \rho^n)^2 - \frac{\partial (\rho a^{\text{PeTS}})}{\partial \rho} \Big|_{\rho^n} (\rho^{n+1} - \rho^n) \right. \\
&\quad \left. - \kappa \nabla \rho^{n+1} \cdot \nabla (\rho^{n+1} - \rho^n) \right] \, dV \\
&+ \int_{\partial \mathcal{B}} \kappa \nabla \rho^{n+1} (\rho^{n+1} - \rho^n) \cdot \vec{n} \, dA \\
&= \int_{\mathcal{B}} \left[-\beta^s (\rho^{n+1} - \rho^n)^2 - \frac{\partial (\rho a^{\text{PeTS}})}{\partial \rho} \Big|_{\rho^n} (\rho^{n+1} - \rho^n) \right. \\
&\quad \left. - \kappa |\nabla \rho^{n+1}|^2 + \kappa \nabla \rho^{n+1} \cdot \nabla \rho^n \right] \, dV \\
&- \int_{\partial \mathcal{B}_s} (\gamma_{\text{sl}} - \gamma_{\text{sv}}) \left[\alpha^s (\rho^{n+1} - \rho^n) + \frac{\partial h(\rho)}{\partial \rho} \Big|_{\rho^n} \right] (\rho^{n+1} - \rho^n) \, dA \quad (\text{B.3})
\end{aligned}$$

Adding (B.1) and (B.2) gives,

$$\begin{aligned}
& \int_{\mathcal{B}} \left[\frac{1}{2} (\rho^n \vec{v}^{n+1} - \rho^{n-1} \vec{v}^n) \cdot \vec{v}^{n+1} + \frac{1}{2} \rho^{n-1} (\vec{v}^{n+1} - \vec{v}^n) \cdot \vec{v}^{n+1} + (\rho^{n+1} - \rho^n) x_g g \right] \, dV \\
&= \int_{\mathcal{B}} \left[-\Delta t 2\eta^v(\rho^n) \left| \nabla^s \vec{v}^{n+1} - \frac{1}{3} \text{tr}(\nabla^s \vec{v}^{n+1}) \mathbf{1} \right|^2 \right. \\
&\quad - \Delta t \rho^n \nabla \mu^{n+1} \cdot \vec{v}^{n+1} - \Delta t \rho^n g \vec{e}_g \cdot \vec{v}^{n+1} \\
&\quad \left. - (\rho^{n+1} - \rho^n) \mu^{n+1} - \Delta t \text{div}(\rho^n \vec{v}^{n+1}) (\mu^{n+1} + x_g g) \right] \, dV \quad (\text{B.4})
\end{aligned}$$

and with (B.3)

$$\begin{aligned}
& \int_{\mathcal{B}} \left[\frac{1}{2} (\rho^n \vec{v}^{n+1} - \rho^{n-1} \vec{v}^n) \cdot \vec{v}^{n+1} + \frac{1}{2} \rho^{n-1} (\vec{v}^{n+1} - \vec{v}^n) \cdot \vec{v}^{n+1} + (\rho^{n+1} - \rho^n) x_g g \right] dV \\
&= \int_{\mathcal{B}} \left[-\Delta t 2\eta^v(\rho^n) \left| \nabla^s \vec{v}^{n+1} - \frac{1}{3} \text{tr}(\nabla^s \vec{v}^{n+1}) \mathbf{1} \right|^2 \right. \\
&\quad - \beta^s (\rho^{n+1} - \rho^n)^2 - \left. \frac{\partial(\rho a^{\text{PeTS}})}{\partial \rho} \Big|_{\rho^n} (\rho^{n+1} - \rho^n) \right. \\
&\quad \left. - \kappa |\nabla \rho^{n+1}|^2 + \kappa \nabla \rho^{n+1} \cdot \nabla \rho^n \right] dV \\
&- \int_{\partial \mathcal{B}_s} (\gamma_{\text{sl}} - \gamma_{\text{sv}}) \left[\alpha^s (\rho^{n+1} - \rho^n) + \frac{\partial h(\rho)}{\partial \rho} \Big|_{\rho^n} \right] (\rho^{n+1} - \rho^n) dA. \tag{B.5}
\end{aligned}$$

C Details of the Analytic Total Phase Field Potential

This section is based on [Diewald et al. 2018a]. The total PF potential of the droplet in a vapor phase configuration F_d consists of three parts. The potential of the liquid inside the droplet F_{dl} , the potential of the vapor phase F_{dv} , and the potential of the interface between liquid and gas F_{di} ,

$$F_d = F_{dl} + F_{dv} + F_{di}. \quad (\text{C.1})$$

The potential of the liquid domain \mathcal{B}_l inside the droplet is

$$F_{dl} = \int_{\mathcal{B}_l} \rho' a^{\text{PeTS}}(\rho') dV = \rho' a(\rho') V' \quad \text{with} \quad V' = \frac{4}{3}\pi \left(r_{\text{ini}} - \frac{l_{\text{PF}}^t}{2} \right)^3. \quad (\text{C.2})$$

The potential of the vapor domain \mathcal{B}_v is

$$F_{dv} = \int_{\mathcal{B}_v} \rho'' a^{\text{PeTS}}(\rho'') dV = \rho'' a(\rho'') V'' \quad \text{with} \quad V'' = V_{\mathcal{B}} - \frac{4}{3}\pi \left(r_{\text{ini}} + \frac{l_{\text{PF}}^t}{2} \right)^3. \quad (\text{C.3})$$

In this, $V_{\mathcal{B}}$ is the volume of the entire computational domain. The potential of the interface between the liquid and the vapor phase (domain \mathcal{B}_i) is

$$\begin{aligned} F_{di} &= \int_{\mathcal{B}_i} \left[\rho a^{\text{PeTS}}(\rho) + \frac{1}{2} \kappa |\nabla \rho|^2 \right] dV \\ &= \int_{\mathcal{B}_i} \left[\omega(\rho) + \frac{1}{2} \kappa |\nabla \rho|^2 + \mu' \rho - p^h \right] dV \\ &= \gamma_{lv} 4\pi r_{\text{ini}}^2 + \int_{\mathcal{B}_i} [\mu' \rho - p^h] dV. \end{aligned} \quad (\text{C.4})$$

With the approximation of the interface by a linear transition from ρ' to ρ'' , cf. (6.4), and using a spherical coordinate system, F_{di} is given by

$$F_{\text{di}} = \gamma_{\text{lv}} 4\pi r_{\text{ini}}^2 + 4\pi \int_{r_{\text{ini}} - 0.5l_{\text{PF}}^t}^{r_{\text{ini}} + 0.5l_{\text{PF}}^t} \left[r^2 \mu' \left(\frac{\rho'' - \rho'}{l_{\text{PF}}^t} \left(r - r_{\text{ini}} + \frac{l_{\text{PF}}^t}{2} \right) + \rho' \right) - r^2 p^{\text{h}} \right] dr. \quad (\text{C.5})$$

The total PF potential of the homogeneous density distribution configuration F_{h} is

$$F_{\text{h}} = \rho_{\text{h}} a^{\text{PeTS}}(\rho_{\text{h}}) V_{\mathcal{B}}, \quad (\text{C.6})$$

with

$$\begin{aligned} \rho_{\text{h}} &= \left[\rho' V' + \rho'' V'' + \int_{\mathcal{B}_i} \rho dV \right] \frac{1}{V_{\mathcal{B}}} \\ &= \left[\rho' V' + \rho'' V'' + 4\pi \int_{r_{\text{ini}} - 0.5l_{\text{PF}}^t}^{r_{\text{ini}} + 0.5l_{\text{PF}}^t} r^2 \left(\frac{\rho'' - \rho'}{l_{\text{PF}}^t} \left(r - r_{\text{ini}} + \frac{l_{\text{PF}}^t}{2} \right) + \rho' \right) dr \right] \frac{1}{V_{\mathcal{B}}}. \end{aligned} \quad (\text{C.7})$$

Bibliography

- Amirfazli, Kwok, Gaydos, and Neumann (1998). Line Tension Measurements through Drop Size Dependence of Contact Angle. *Journal of colloid and interface science*, 205(1):1–11.
- Amirfazli, A. and Neumann, A. W. (2004). Status of the three-phase line tension: a review. *Advances in colloid and interface science*, 110(3):121–141.
- Anders, D. and Weinberg, K. (2011a). A variational approach to the decomposition of unstable viscous fluids and its consistent numerical approximation. *ZAMM*, 91(8):609–629.
- Anders, D. and Weinberg, K. (2011b). Numerical simulation of diffusion induced phase separation and coarsening in binary alloys. *Computational Materials Science*, 50(4):1359–1364.
- Anderson, D. M., McFadden, G. B., and Wheeler, A. A. (1998). Diffuse-Interface Methods in Fluid Mechanics. *Annual Review of Fluid Mechanics*, 30(1):139–165.
- Arrabiyeh, P. A., Kirsch, B., and Aurich, J. C. (2017). Development of Micro Pencil Grinding Tools Via an Electroless Plating Process. *Journal of Micro and Nano-Manufacturing*, 5(1):011002.
- Balter, M. (2009). Archaeology. Clothes make the (hu) man. *Science*, 325(5946):1329.
- Bathe, K.-J. (1996). *Finite element procedures*. Prentice Hall, Englewood Cliffs, NJ.
- Becker, S. (2015). *Anwendung Automatischer Differentiationsalgorithmen für die Finite-Elemente-Methode*. Master thesis, Technische Universität Kaiserslautern.
- Becker, S., Urbassek, H. M., Horsch, M., and Hasse, H. (2014). Contact angle of sessile drops in Lennard-Jones systems. *Langmuir*, 30(45):13606–13614.

- Becker, W. and Gross, D. (2002). *Mechanik elastischer Körper und Strukturen*. Springer Berlin Heidelberg, Berlin, Heidelberg.
- Beckermann, C., Diepers, H.-J., Steinbach, I., Karma, A., and Tong, X. (1999). Modeling Melt Convection in Phase-Field Simulations of Solidification. *Journal of Computational Physics*, 154(2):468–496.
- Ben Said, M., Selzer, M., Nestler, B., Braun, D., Greiner, C., and Garcke, H. (2014). A phase-field approach for wetting phenomena of multiphase droplets on solid surfaces. *Langmuir*, 30(14):4033–4039.
- Berry, M. V. (1971). The molecular mechanism of surface tension. *Physics Education*, 6(2):79–84.
- Bilz, R. (2018). *Implementierung eines 3D Finite Elemente Modells zur Beschreibung der Dynamischen Benetzung von Oberflächen*. Diploma thesis, Technische Universität Kaiserslautern.
- Bishop, C. M. and Craig Carter, W. (2002). Relating atomistic grain boundary simulation results to the phase-field model. *Computational Materials Science*, 25(3):378–386.
- Blauwhoff, R. (2015). *FE-Implementierung eines Phasenfeldmodells für Tropfenbildung und Benetzung*. Master thesis, Technische Universität Kaiserslautern.
- Blecura, P., Brinkmann, M., Lipowsky, R., and Kierfeld, J. (2009). Morphological transitions of liquid droplets on circular surface domains. *Langmuir*, 25(23):13493–13502.
- Bliznyuk, O., Jansen, H. P., Kooij, E. S., Zandvliet, H. J. W., and Poelsema, B. (2011). Smart design of stripe-patterned gradient surfaces to control droplet motion. *Langmuir*, 27(17):11238–11245.
- Bohley, M., Reichenbach, I., Kieren-Ehse, S., Heberger, L., Arrabiyeh, P., Merz, R., Böhme, L., Hering, J., Kirsch, B., Kopnarski, M., Kerscher, E., von Freymann, G., and Aurich, J. (2018). Coating of Ultra-Small Micro End Mills: Analysis of Performance and Suitability of Eight Different Hard-Coatings. *Journal of Manufacturing and Materials Processing*, 2(2):22.
- Bonnet, J. and Wood, R. D. (2009). *Nonlinear continuum mechanics for finite element analysis*. Cambridge Univ. Press, Cambridge, 2nd edition.
- Böswirth, L., Bschorer, S., and Buck, T. (2014). *Technische Strömungslehre: Lehr- und Übungsbuch*. Springer Vieweg, Wiesbaden, 10th edition.

- Braack, M. and Prohl, A. (2013). Stable discretization of a diffuse interface model for liquid-vapor flows with surface tension. *ESAIM: Mathematical Modelling and Numerical Analysis*, 47(2):401–420.
- Bragard, J., Karma, A., Lee, Y. H., and Plapp, M. (2002). Linking Phase-Field and Atomistic Simulations to Model Dendritic Solidification in Highly Undercooled Melts. *Interface Science*, 10(2/3):121–136.
- Brezzi, F. and Fortin, M. (1991). *Mixed and hybrid finite element methods*, volume 15 of *Springer series in computational mathematics*. Springer, New York, NY.
- Brinkmann, M., Kierfeld, J., and Lipowsky, R. (2005). Stability of liquid channels or filaments in the presence of line tension. *Journal of Physics: Condensed Matter*, 17(15):2349–2364.
- Brinkmann, M. and Lipowsky, R. (2002). Wetting morphologies on substrates with striped surface domains. *Journal of Applied Physics*, 92(8):4296–4306.
- Brochard, F. (1989). Motions of droplets on solid surfaces induced by chemical or thermal gradients. *Langmuir*, 5(2):432–438.
- Brzoska, J. B., Brochard-Wyart, F., and Rondelez, F. (1993). Motions of droplets on hydrophobic model surfaces induced by thermal gradients. *Langmuir*, 9(8):2220–2224.
- Bueno, J., Bazilevs, Y., Juanes, R., and Gomez, H. (2018). Wettability control of droplet durotaxis. *Soft Matter*, 52:2412.
- Bueno, J. and Gomez, H. (2016). Liquid-vapor transformations with surfactants. Phase-field model and Isogeometric Analysis. *Journal of Computational Physics*, 321:797–818.
- Cahn, J. W. and Allen, S. M. (1977). A Microscopic Theory for Domain Wall Motion and its Experimental Verification in Fe-Al Alloy Domain Growth Kinetics. *Journal de Physique Colloques*, 38(C7):C7_51–C7_54.
- Cahn, J. W. and Hilliard, J. E. (1958). Free Energy of a Nonuniform System. I. Interfacial Free Energy. *The Journal of Chemical Physics*, 28(2):258.
- Cassie, A. B. D. and Baxter, S. (1944). Wettability of porous surfaces. *Transactions of the Faraday Society*, 40:546.

- Chakraborty, M., Chowdhury, A., Bhusan, R., and DasGupta, S. (2015). Molecular Dynamics Study of Thermally Augmented Nanodroplet Motion on Chemical Energy Induced Wettability Gradient Surfaces. *Langmuir*, 31(41):11260–11268.
- Checco, A., Ocko, B. M., Tasinkevych, M., and Dietrich, S. (2012). Stability of thin wetting films on chemically nanostructured surfaces. *Physical Review Letters*, 109(16):166101.
- Chowdhury, I. U., Sinha Mahapatra, P., and Sen, A. K. (2019). Self-driven droplet transport: Effect of wettability gradient and confinement. *Physics of Fluids*, 31(4):042111.
- Coleman, B. D. and Noll, W. (1963). The thermodynamics of elastic materials with heat conduction and viscosity. *Archive for Rational Mechanics and Analysis*, 13(1):167–178.
- CRC 926 (2018). Microscale Morphology of Component Surfaces. *Research Proposal for 3rd Funding Period, TU Kaiserslautern*.
- Danilov, D., Nestler, B., Guerdane, M., and Teichler, H. (2009). Bridging the gap between molecular dynamics simulations and phase-field modelling: Dynamics of a [Ni_xZr_{1-x}] liquid-Zr crystal solidification front. *Journal of Physics D: Applied Physics*, 42(1):015310.
- Darhuber, A. A. and Troian, S. M. (2005). Principles of Microfluidic Actuation by Modulation of Surface Stresses. *Annual Review of Fluid Mechanics*, 37(1):425–455.
- Davies, J. T. and Rideal, E. K. (1963). *Interfacial Phenomena*. Academic Press Inc., London.
- de Jong, E., Wang, Y., Den Toonder, J. M. J., and Onck, P. R. (2019). Climbing droplets driven by mechanowetting on transverse waves. *Science advances*, 5(6):eaaw0914.
- Diehl, D., Kremser, J., Kröner, D., and Rohde, C. (2016). Numerical solution of Navier–Stokes–Korteweg systems by Local Discontinuous Galerkin methods in multiple space dimensions. *Applied Mathematics and Computation*, 272:309–335.
- Diewald, F., Heier, M., Horsch, M., Kuhn, C., Langenbach, K., Hasse, H., and Müller, R. (2018a). Three-dimensional phase field modeling of inhomogeneous gas-liquid systems using the PeTS equation of state. *The Journal of Chemical Physics*, 149(6):064701.

- Diewald, F., Heier, M., Lautenschlaeger, M., Horsch, M., Kuhn, C., Langenbach, K., Hasse, H., and Müller, R. (2019). A Navier-Stokes-Korteweg Model for Dynamic Wetting based on the PeTS Equation of State. *PAMM*, 19(1).
- Diewald, F., Kuhn, C., Blauwhoff, R., Heier, M., Becker, S., Werth, S., Horsch, M., Hasse, H., and Müller, R. (2016). Simulation of Surface Wetting by Droplets Using a Phase Field Model. *PAMM*, 16(1):519–520.
- Diewald, F., Kuhn, C., Heier, M., Horsch, M., Langenbach, K., Hasse, H., and Müller, R. (2017). Surface Wetting with Droplets: A Phase Field Approach. *PAMM*, 17(1):501–502.
- Diewald, F., Kuhn, C., Heier, M., Langenbach, K., Horsch, M., Hasse, H., and Müller, R. (2018b). Investigating the stability of the phase field solution of equilibrium droplet configurations by eigenvalues and eigenvectors. *Computational Materials Science*, 141:185–192.
- Diewald, F., Lautenschlaeger, M. P., Stephan, S., Langenbach, K., Kuhn, C., Seckler, S., Bungartz, H.-J., Hasse, H., and Müller, R. (2020a). Molecular dynamics and phase field simulations of droplets on surfaces with wettability gradient. *Computer Methods in Applied Mechanics and Engineering*, 361:112773.
- Diewald, F., van der Zee, K. G., and Müller, R. (2020b). On the Rational Derivation of the Navier-Stokes-Korteweg Model and a Semi-Implicit Energy Dissipative Time Integration Scheme. *in preparation*.
- Dong, L., Chaudhury, A., and Chaudhury, M. K. (2006). Lateral vibration of a water drop and its motion on a vibrating surface. *European Physical Journal E*, 21(3):231–242.
- Dorfler, F., Rauscher, M., and Dietrich, S. (2013). Stability of thin liquid films and sessile droplets under confinement. *Physical Review E*, 88(1):012402.
- Dunn, J. E. and Serrin, J. (1985). On the thermomechanics of interstitial working. *Archive for Rational Mechanics and Analysis*, 88(2).
- Eyre, D. J. (1998). Unconditionally Gradient Stable Time Marching the Cahn-Hilliard Equation. *MRS Proceedings*, 529:304.
- Falls, A. H., Scriven, L. E., and Davis, H. T. (1981). Structure and stress in spherical microstructures. *The Journal of Chemical Physics*, 75(8):3986–4002.
- Farkas, L. (1927). Keimbildungsgeschwindigkeit in übersättigten Dämpfen. *Zeitschrift für Physikalische Chemie*, 125U(1).

- FEAP (8.4). A Finite Element Analysis Program. <http://projects.ce.berkeley.edu/feap/>.
- Fike, J. A. (2013). *Multi-Objective Optimization using Hyper-Dual Numbers*. PhD thesis, Stanford University.
- Fike, J. A. and Alonso, J. J. (2011). The Development of Hyper-Dual Numbers for Exact Second Derivative Calculations. *49th AIAA Aerospace Sciences Meeting*, AIAA 2011-886:1–17.
- Finel, A., Le Bouar, Y., Dabas, B., Appolaire, B., Yamada, Y., and Mohri, T. (2018). Sharp Phase Field Method. *Physical Review Letters*, 121(2):025501.
- Fried, E. and Gurtin, M. E. (2007). Thermomechanics of the interface between a body and its environment. *Continuum Mechanics and Thermodynamics*, 19(5):253–271.
- Gellrich, M. (2019). *A Better VTU Output Routine for the Finite Element Analysis Program (FEAP)*. Bachelor thesis, Technische Universität Kaiserslautern.
- Gomez, H., Hughes, T. J., Nogueira, X., and Calo, V. M. (2010). Isogeometric analysis of the isothermal Navier–Stokes–Korteweg equations. *Computer Methods in Applied Mechanics and Engineering*, 199(25-28):1828–1840.
- Gomez, H. and van der Zee, K. G. (2017). Computational Phase-Field Modeling. In *Encyclopedia of Computational Mechanics Second Edition*, pages 1–35. American Cancer Society.
- Gurtin, M. E. (1996). Generalized Ginzburg-Landau and Cahn-Hilliard equations based on a microforce balance. *Physica D*, 92(3-4):178–192.
- Gurtin, M. E., Fried, E., and Anand, L. (2010). *The mechanics and thermodynamics of continua*. Cambridge Univ. Press, Cambridge u.a., 1. publ edition.
- Halverson, J. D., Maldarelli, C., Couzis, A., and Koplik, J. (2008). A molecular dynamics study of the motion of a nanodroplet of pure liquid on a wetting gradient. *The Journal of Chemical Physics*, 129(16):164708.
- Heier, M., Diewald, F., Horsch, M. T., Langenbach, K., Müller, R., and Hasse, H. (2019). Molecular Dynamics Study of Adsorption of the Lennard-Jones Truncated and Shifted Fluid on Planar Walls. *Journal of Chemical & Engineering Data*, 64(2):386–394.

- Heier, M., Stephan, S., Liu, J., Chapman, W. G., Hasse, H., and Langenbach, K. (2018). Equation of state for the Lennard-Jones truncated and shifted fluid with a cut-off radius of 2.5 sigma based on perturbation theory and its applications to interfacial thermodynamics. *Molecular Physics*, 116(15-16):2083–2094.
- Heinen, M., Vrabec, J., and Fischer, J. (2016). Communication: Evaporation: Influence of heat transport in the liquid on the interface temperature and the particle flux. *The Journal of Chemical Physics*, 145(8):081101.
- Hering, J., Eifler, M., Seewig, J., von Freymann, G., Hofherr, L., and Ziegler, C. (2018). Two-photon laser lithography in optical metrology. *Proceedings of SPIE OPTO*, page 36.
- Hofmann, T. (2018). *Phase-Field Methods for Deformation Processes in Lithium-Ion Batteries*. PhD thesis, Technische Universität Kaiserslautern.
- Holzappel, G. A. (2010). *Nonlinear solid mechanics: A continuum approach for engineering*. Wiley, Chichester.
- Honisch, C., Lin, T.-S., Heuer, A., Thiele, U., and Gurevich, S. V. (2015). Instabilities of Layers of Deposited Molecules on Chemically Stripe Patterned Substrates: Ridges versus Drops. *Langmuir*, 31(38):10618–10631.
- Horsch, M., Hasse, H., Shchekin, A. K., Agarwal, A., Eckelsbach, S., Vrabec, J., Müller, E. A., and Jackson, G. (2012). Excess equimolar radius of liquid drops. *Physical Review E*, 85(3 Pt 1):031605.
- Horsch, M., Heitzig, M., Dan, C., Harting, J., Hasse, H., and Vrabec, J. (2010). Contact angle dependence on the fluid-wall dispersive energy. *Langmuir*, 26(13):10913–10917.
- Horsch, M., Miroshnichenko, S., and Vrabec, J. (2009). Steady-State Molecular Dynamics Simulation of Vapour to Liquid Nucleation with McDonald’s Deamon. *Journal of Physical Studies*, 13(4):4004.
- Horsch, M., Vrabec, J., and Hasse, H. (2008). Modification of the classical nucleation theory based on molecular simulation data for surface tension, critical nucleus size, and nucleation rate. *Physical Review E*, 78(1 Pt 1):011603.
- Hrubý, J., Labetski, D. G., and van Dongen, M. E. H. (2007). Gradient theory computation of the radius-dependent surface tension and nucleation rate for n-nonane clusters. *The Journal of Chemical Physics*, 127(16):164720.

- Huang, J.-J., Huang, H., and Wang, X. (2014). Numerical study of drop motion on a surface with stepwise wettability gradient and contact angle hysteresis. *Physics of Fluids*, 26(6):062101.
- Hughes, T., Cottrell, J. A., and Bazilevs, Y. (2005). Isogeometric analysis: CAD, finite elements, NURBS, exact geometry and mesh refinement. *Computer Methods in Applied Mechanics and Engineering*, 194(39-41):4135–4195.
- Ichimura, K. (2000). Light-Driven Motion of Liquids on a Photoresponsive Surface. *Science*, 288(5471):1624–1626.
- Jamet, D., Torres, D., and Brackbill, J. U. (2002). On the Theory and Computation of Surface Tension: The Elimination of Parasitic Currents through Energy Conservation in the Second-Gradient Method. *Journal of Computational Physics*, 182(1):262–276.
- Johnson, J. K., Zollweg, J. A., and Gubbins, K. E. (1993). The Lennard-Jones equation of state revisited. *Molecular Physics*, 78(3):591–618.
- Jones, J. E. (1924). On the Determination of Molecular Fields. II. From the Equation of State of a Gas. *Proceedings of the Royal Society A: Mathematical, Physical and Engineering Sciences*, 106(738):463–477.
- Kalikmanov, V. I. (2013). *Nucleation Theory*. Springer Netherlands, Dordrecht.
- Kargupta, K., Konnur, R., and Sharma, A. (2000). Instability and Pattern Formation in Thin Liquid Films on Chemically Heterogeneous Substrates. *Langmuir*, 16(26):10243–10253.
- Kim, J. S. (2012). Phase-Field Models for Multi-Component Fluid Flows. *Communications in Computational Physics*, 12:613–661.
- Kneip, L. (2019). *Finite Elemente Untersuchung zum Einfluss der Längenskala auf die Tropfenform bei Oberflächenbenetzung*. Bachelor thesis, Technische Universität Kaiserslautern.
- Kuhn, C. (2013). *Numerical and analytical investigation of a phase field model for fracture*. PhD thesis, Technische Universität Kaiserslautern.
- Kuhn, C. and Müller, R. (2010). A continuum phase field model for fracture. *Engineering Fracture Mechanics*, 77(18):3625–3634.
- Kunti, G., Bhattacharya, A., and Chakraborty, S. (2018a). Alteration in contact line dynamics of fluid-fluid interfaces in narrow confinements through competition between thermocapillary and electrothermal effects. *Physics of Fluids*, 30(8):082005.

- Kunti, G., Bhattacharya, A., and Chakraborty, S. (2018b). Electrothermally actuated moving contact line dynamics over chemically patterned surfaces with resistive heaters. *Physics of Fluids*, 30(6):062004.
- Kurzweil, P. and Scheipers, P. (2012). *Chemie: Grundlagen, Aufbauwissen, Anwendungen und Experimente*. Naturwissenschaftliche Grundlagen. Vieweg+Teubner Verlag /Springer Fachmedien Wiesbaden GmbH, Wiesbaden, 9th edition.
- Kvavadze, E., Bar-Yosef, O., Belfer-Cohen, A., Boaretto, E., Jakeli, N., Matskevich, Z., and Meshveliani, T. (2009). 30,000-year-old wild flax fibers. *Science*, 325(5946):1359.
- Lamorgese, A. G. and Mauri, R. (2009). Diffuse-interface modeling of liquid-vapor phase separation in a van der Waals fluid. *Physics of Fluids*, 21(4):044107.
- Langenbach, K., Heilig, M., Horsch, M., and Hasse, H. (2018). Study of homogeneous bubble nucleation in liquid carbon dioxide by a hybrid approach combining molecular dynamics simulation and density gradient theory. *The Journal of Chemical Physics*, 148(12):124702.
- Lautenschlaeger, M. P. and Hasse, H. (2019). Transport properties of the Lennard-Jones truncated and shifted fluid from non-equilibrium molecular dynamics simulations. *Fluid Phase Equilibria*, 482:38–47.
- Lauth, G. J. and Kowalczyk, J. (2015). *Thermodynamik: Eine Einführung*. Lehrbuch. Springer Spektrum, Berlin.
- Law, K.-Y. and Zhao, H. (2016). *Surface Wetting*. Springer International Publishing, Cham.
- Lekner, J. and Henderson, J. R. (1978). Theoretical determination of the thickness of a liquid-vapour interface. *Physica A*, 94(3-4):545–558.
- Li, Q., Yu, Y., Zhou, P., and Yan, H. J. (2017). Droplet migration on hydrophobic–hydrophilic hybrid surfaces: A lattice Boltzmann study. *RSC Advances*, 7(24):14701–14708.
- Li, Z., Hu, G.-H., Wang, Z.-L., Ma, Y.-B., and Zhou, Z.-W. (2013). Three dimensional flow structures in a moving droplet on substrate: A dissipative particle dynamics study. *Physics of Fluids*, 25(7):072103.
- Liu, C., Sun, J., Li, J., Xiang, C., Che, L., Wang, Z., and Zhou, X. (2017). Long-range spontaneous droplet self-propulsion on wettability gradient surfaces. *Scientific reports*, 7(1):7552.

- Liu, J., Gomez, H., Evans, J. A., Hughes, T. J., and Landis, C. M. (2013). Functional entropy variables: A new methodology for deriving thermodynamically consistent algorithms for complex fluids, with particular reference to the isothermal Navier–Stokes–Korteweg equations. *Journal of Computational Physics*, 248:47–86.
- Liu, J., Landis, C. M., Gomez, H., and Hughes, T. J. (2015). Liquid–vapor phase transition: Thermomechanical theory, entropy stable numerical formulation, and boiling simulations. *Computer Methods in Applied Mechanics and Engineering*, 297:476–553.
- Lotfi, A., Vrabec, J., and Fischer, J. (2014). Evaporation from a free liquid surface. *International Journal of Heat and Mass Transfer*, 73:303–317.
- Marchand, A., Weijs, J. H., Snoeijer, J. H., and Andreotti, B. (2011). Why is surface tension a force parallel to the interface? *American Journal of Physics*, 79(10):999–1008.
- Marmur, A. (1997). Line Tension and the Intrinsic Contact Angle in Solid–Liquid–Fluid Systems. *Journal of colloid and interface science*, 186(2):462–466.
- Mechkov, S., Oshanin, G., Rauscher, M., Brinkmann, M., Cazabat, A. M., and Dietrich, S. (2007). Contact line stability of ridges and drops. *Europhysics Letters*, 80(6):66002.
- Moelans, N., Blanpain, B., and Wollants, P. (2008). An introduction to phase-field modeling of microstructure evolution. *Calphad*, 32(2):268–294.
- Moosavi, A. and Mohammadi, A. (2011). Dynamics of nanodroplets on wettability gradient surfaces. *Journal of Physics: Condensed Matter*, 23(8):085004.
- Nestler, B., Garcke, H., and Stinner, B. (2005). Multicomponent alloy solidification: phase-field modeling and simulations. *Physical Review E*, 71(4 Pt 1):041609.
- Nestler, B., Selzer, M., and Danilov, D. (2009). Phase-field simulations of nuclei and early stage solidification microstructures. *Journal of Physics: Condensed Matter*, 21(46):464107.
- Onuki, A. (2007). Dynamic van der Waals theory. *Physical Review E*, 75(3 Pt 2):036304.
- Pan, S., Zhu, M., and Rettenmayr, M. (2015). Phase-field modeling of liquid droplet migration in a temperature gradient. *IOP Conference Series: Materials Science and Engineering*, 84:012073.

- Parker, A. R. and Lawrence, C. R. (2001). Water capture by a desert beetle. *Nature*, 414(6859):33–34.
- Pecenko, A., Kuerten, J., and van der Geld, C. (2010). A diffuse-interface approach to two-phase isothermal flow of a Van der Waals fluid near the critical point. *International Journal of Multiphase Flow*, 36(7):558–569.
- Pecenko, A., van Deurzen, L., Kuerten, J., and van der Geld, C. (2011). Non-isothermal two-phase flow with a diffuse-interface model. *International Journal of Multiphase Flow*, 37(2):149–165.
- Pismen, L. M. and Thiele, U. (2006). Asymptotic theory for a moving droplet driven by a wettability gradient. *Physics of Fluids*, 18(4):042104.
- Poisson, S.-D. (1831). *Nouvelle Théorie de l’Action Capillaire*. Bachelier père et fils, Paris.
- Rajagopal, A., Fischer, P., Kuhl, E., and Steinmann, P. (2010). Natural element analysis of the Cahn–Hilliard phase-field model. *Computational Mechanics*, 46(3):471–493.
- Rosso, R. and Virga, E. G. (2004). Local stability for a general wetting functional. *Journal of Physics A: Mathematical and General*, 37(13):3989–4015.
- Rowlinson, J. S. and Widom, B. (1982). *Molecular Theory of Capillarity*. Oxford University Press, New York.
- Schlüter, A. (2018). *Phase Field Modeling of Dynamic Brittle Fracture*. PhD thesis, Technische Universität Kaiserslautern.
- Schlüter, A., Kuhn, C., Noll, T., Diewald, F., and Müller, R. (2017). Numerical Solution Strategies for a Dynamic Phase Field Fracture Model. *Applied Mechanics and Materials*, 869:29–49.
- Schmidt, S., Dornisch, W., and Müller, R. (2017). A phase field model for martensitic transformation coupled with the heat equation. *GAMM-Mitteilungen*, 40(2):138–153.
- Schmitt, R., Kuhn, C., and Müller, R. (2017). On a phase field approach for martensitic transformations in a crystal plastic material at a loaded surface. *Continuum Mechanics and Thermodynamics*, 29(4):957–968.
- Schweigler, K. M., Ben Said, M., Seifritz, S., Selzer, M., and Nestler, B. (2017). Experimental and numerical investigation of drop evaporation depending on the shape of the liquid/gas interface. *International Journal of Heat and Mass Transfer*, 105:655–663.

- Shen, J., Xu, J., and Yang, J. (2017). A New Class of Efficient and Robust Energy Stable Schemes for Gradient Flows. *arXiv*.
- Shokrpour Roudbari, M., Şimşek, G., van Brummelen, E. H., and van der Zee, K. G. (2018). Diffuse-interface two-phase flow models with different densities: A new quasi-incompressible form and a linear energy-stable method. *Mathematical Models and Methods in Applied Sciences*, 28(04):733–770.
- Sibley, D. N., Nold, A., and Kalliadasis, S. (2013). Unifying binary fluid diffuse-interface models in the sharp-interface limit. *Journal of Fluid Mechanics*, 736:5–43.
- Stephan, S., Liu, J., Langenbach, K., Chapman, W. G., and Hasse, H. (2018). Vapor–Liquid Interface of the Lennard-Jones Truncated and Shifted Fluid: Comparison of Molecular Simulation, Density Gradient Theory, and Density Functional Theory. *The Journal of Physical Chemistry C*, 122(43):24705–24715.
- Strasser, P. J., Tierra, G., Dünweg, B., and Lukáčová-Medvid’ová, M. (2019). Energy-stable linear schemes for polymer–solvent phase field models. *Computers & Mathematics with Applications*, 77(1):125–143.
- Taylor, C. and Hughes, T. G. (1981). *Finite element programming of the Navier-Stokes equations*. Pineridge Press, Swansea, UK.
- Teto, J. O. D. (2018). *FE-Implementierung eines Phasenfeld-Elements zur Modellierung der Wechselwirkung zwischen Fluiden und Festkörpern*. Bachelor thesis, Technische Universität Kaiserslautern.
- Thiele, U., Bruschi, L., Bestehorn, M., and Bar, M. (2003). Modelling thin-film dewetting on structured substrates and templates: bifurcation analysis and numerical simulations. *European Physical Journal E*, 11(3):255–271.
- Thiele, U., John, K., and Bär, M. (2004). Dynamical model for chemically driven running droplets. *Physical Review Letters*, 93(2):027802.
- Thol, M., Rutkai, G., Span, R., Vrabec, J., and Lustig, R. (2015). Equation of State for the Lennard-Jones Truncated and Shifted Model Fluid. *International Journal of Thermophysics*, 36(1):25–43.
- Thomasset, F. (1981). *Implementation of finite element method for Navier-Stokes equations*. Springer series in computational physics. Springer, New York.
- Tian, L., Xu, Y., Kuerten, J., and van der Vegt, J. (2015). A local discontinuous Galerkin method for the (non)-isothermal Navier–Stokes–Korteweg equations. *Journal of Computational Physics*, 295:685–714.

- Vaithyanathan, V., Wolverton, C., and Chen, L. Q. (2002). Multiscale modeling of precipitate microstructure evolution. *Physical Review Letters*, 88(12):125503.
- Vaithyanathan, V., Wolverton, C., and Chen, L. Q. (2004). Multiscale modeling of theta' precipitation in Al-Cu binary alloys. *Acta Materialia*, 52(10):2973–2987.
- van Brummelen, E. H., Roudbari, M. S., Şimşek, G., and van der Zee, K. G. (2017). 8. Binary-fluid–solid interaction based on the Navier–Stokes–Cahn–Hilliard Equations. In Frei, S., Holm, B., Richter, T., Wick, T., and Yang, H., editors, *Fluid-Structure Interaction*. De Gruyter, Berlin, Boston.
- van der Waals, J. D. (1979). The thermodynamic theory of capillarity under the hypothesis of a continuous variation of density. *Journal of Statistical Physics*, 20(2):200–244.
- Völker, B., Landis, C. M., and Kamlah, M. (2012). Multiscale modeling for ferroelectric materials: Identification of the phase-field model's free energy for PZT from atomistic simulations. *Smart Materials and Structures*, 21(3):035025.
- Völker, B., Marton, P., Elsässer, C., and Kamlah, M. (2011). Multiscale modeling for ferroelectric materials: A transition from the atomic level to phase-field modeling. *Continuum Mechanics and Thermodynamics*, 23(5):435–451.
- Volmer, M. and Weber, t. (1926). Keimbildung in übersättigten Gebilden. *Zeitschrift für Physikalische Chemie*, 119U(1).
- Vrabec, J., Kedia, G. K., Fuchs, G., and Hasse, H. (2006). Comprehensive study of the vapour–liquid coexistence of the truncated and shifted Lennard–Jones fluid including planar and spherical interface properties. *Molecular Physics*, 104(9):1509–1527.
- Wang, Y., Minh, D.-Q., and Amberg, G. (2015). Dynamic wetting of viscoelastic droplets. *Physical Review E*, 92(4):043002.
- Wells, G. N., Kuhl, E., and Garikipati, K. (2006). A discontinuous Galerkin method for the Cahn–Hilliard equation. *Journal of Computational Physics*, 218(2):860–877.
- Wenzel, R. N. (1936). Resistance of Solid Surfaces to Wetting by Water. *Industrial & Engineering Chemistry*, 28(8):988–994.
- Weyer, F., Ben Said, M., Hötzer, J., Berghoff, M., Dreesen, L., Nestler, B., and Vandewalle, N. (2015). Compound Droplets on Fibers. *Langmuir*, 31(28):7799–7805.

- Wriggers, P. (2001). *Nichtlineare Finite-Element-Methoden*. Springer Berlin Heidelberg, Berlin, Heidelberg and s.l.
- Wu, K.-A. and Karma, A. (2007). Phase-field crystal modeling of equilibrium bcc-liquid interfaces. *Physical Review B*, 76(18):121.
- Wu, Y., Wang, F., Selzer, M., and Nestler, B. (2019). Investigation of Equilibrium Droplet Shapes on Chemically Striped Patterned Surfaces Using Phase-Field Method. *Langmuir*, 35(25):8500–8516.
- Xiao, J., Pan, F., Xia, H., Zou, S., Zhang, H., George, O. A., Zhou, F., and Huang, Y. (2018). Computational Study of Single Droplet Deposition on Randomly Rough Surfaces: Surface Morphological Effect on Droplet Impact Dynamics. *Industrial & Engineering Chemistry Research*, 57(22):7664–7675.
- Xu, B.-X., Schrade, D., Gross, D., and Mueller, R. (2010). Fracture simulation of ferroelectrics based on the phase field continuum and a damage variable. *International Journal of Fracture*, 166(1-2):163–172.
- Xu, J., Li, Y., Wu, S., and Bousquet, A. (2017). On the Stability and Accuracy of Partially and Fully Implicit Schemes for Phase Field Modeling. *arXiv*.
- Xu, X. and Wang, X. (2010). Derivation of the Wenzel and Cassie Equations from a Phase Field Model for Two Phase Flow on Rough Surface. *SIAM Journal on Applied Mathematics*, 70(8):2929–2941.
- Yang, X., Feng, J. J., Liu, C., and Shen, J. (2006). Numerical simulations of jet pinching-off and drop formation using an energetic variational phase-field method. *Journal of Computational Physics*, 218(1):417–428.
- Young, T. (1805). An Essay on the Cohesion of Fluids. *Philosophical Transactions of the Royal Society of London*, 95(0):65–87.
- Yue, P., Zhou, C., and Feng, J. J. (2010). Sharp-interface limit of the Cahn–Hilliard model for moving contact lines. *Journal of Fluid Mechanics*, 645:279.
- Yurkiv, V., Yarin, A. L., and Mashayek, F. (2018). Modeling of Droplet Impact onto Polarized and Nonpolarized Dielectric Surfaces. *Langmuir*, 34(34):10169–10180.
- Zienkiewicz, O. C. and Taylor, R. L. (2006). *The finite element method for solid and structural mechanics*. Elsevier Butterworth-Heinemann, Amsterdam, 6th edition.

Zienkiewicz, O. C., Taylor, R. L., and Nithiarasu, P. (2009). *The finite element method for fluid dynamics*. Elsevier Butterworth-Heinemann, Amsterdam, 6. ed. edition.

List of Figures

1.1	Sketch: The PF model of this work bridges the gap between molecular models on the nanoscale and phenomenological continuum models on the macroscale.	3
1.2	The PF model is connected to MD simulations by an equation of state and dissipative properties. Both are obtained from MD simulations. After a validation of the PF results on the nanoscale, a scale bridging can be applied in order to enable the investigation of larger and more complex scenarios.	4
2.1	(a): Spherical droplet cut in half. The green arrow depicts the resultant pressure difference Δp^h on the cut plane. The balance of forces yields a positive value for Δp^h according to (2.1), i.e. the hydrostatic pressure in the liquid phase is larger than in the vapor phase. (b): Droplet on solid surface with contact angle Θ	10
2.2	(a): Wenzel wetting state. (b): Cassie-Baxter wetting state.	11
3.1	Sketch of a double-well potential (left) and change of the order parameter across the diffuse interface (right). The scale and dimensions depend on the type of application.	15
3.2	Classification of PF models for fluids. The models of relevance for this work are “Allen-Cahn” and “Navier-Stokes-Korteweg”. The static “Allen-Cahn” model can be derived from the dynamic “Navier-Stokes-Korteweg” model by a simplification, cf. section 3.5.	16
3.3	Body with arbitrary forces acting on its boundary surface cut by a plane surface. The two parts of the body interact with each other by internal forces.	17
3.4	Material volume \mathcal{B}_t with physical quantity \mathcal{A}	18
3.5	The domain \mathcal{B} is fixed in space and part of its boundary may be given by a solid surface $\partial\mathcal{B}_s$. The material volume \mathcal{B}_t is any subset of the domain \mathcal{B}	22

4.1	Left: The double-well function ρa^e yields two stable bulk phases at ρ'' and ρ' . Since the values of ρ'' and ρ' depend on the fluid under consideration, the density is normalized such that the bulk phases are given by $\varphi'' = 0$ and $\varphi' = 1$. Right: Plot of φ along an axis x that is perpendicular to a vapor-liquid interface. The interface width is l^e	35
4.2	Plot of the interpolation function $h(\varphi)$. It is chosen because of its numerically advantageous properties.	38
4.3	Plot of the LJ potential. The distance between two particles is denoted by r^{LJ} . The energy and size parameter are ε^{LJ} and σ^{LJ} . The LJ potential leads to an attraction between particles if r^{LJ} is larger than the position of the potential well and to a repulsion if r^{LJ} is smaller than the position of the potential well.	40
4.4	Left: Plot of $\rho a^{\text{PeTS}}(\rho)$ for $T = 0.7 \frac{\varepsilon^{\text{LJ}}}{k_{\text{B}}}$. The densities of the bulk phases ρ'' and ρ' are depicted with dashed lines. The blue line represents the energy that results from simply mixing the energies of the homogeneous bulk phases. Right: Homogeneous excess free energy density. This energy results from subtracting the (blue) mixing energy from $\rho a^{\text{PeTS}}(\rho)$. [Heier et al. 2018; Diewald et al. 2018a]	42
4.5	Two-dimensional droplet. The integral over the pressure drop that is found in the direction of the interface defines the surface tension between the liquid and the vapor phase γ_{lv}	47
4.6	Viscosity of the LJTS fluid η^{v} as a function of density ρ and temperature T . The plot compares the viscosity data of MD simulations as reported in [Lautenschlaeger and Hasse 2019] with the viscosity correlation stated in (4.54). The symbols represent the MD data and the surface shows the results from the correlation. For meta- and unstable states, Lautenschlaeger and Hasse [2019] do not report any viscosity data. Nevertheless, the correlation is also used for these states. [Diewald et al. 2020a]	50
4.7	Viscosity of the LJTS fluid η^{v} along two isotherms. The plot compares the viscosity data of MD simulations as reported in [Lautenschlaeger and Hasse 2019] with the viscosity correlation stated in (4.54). The symbols represent the MD data and the lines show the results from the correlation. For meta- and unstable states, Lautenschlaeger and Hasse [2019] do not report any viscosity data. Nevertheless, the correlation is also used for these states. [Diewald et al. 2020a]	51
5.1	Temporal discretization.	54
5.2	Sketch of first steps of a one-dimensional Newton-Raphson method.	57

5.3	Plots of the second derivatives of the local part of the Helmholtz free energy per volume ρa^{PeTS} (top) and the interpolation function $h(\rho)$ (bottom) at $T = 0.7 \frac{\epsilon_{\text{LJ}}}{k_{\text{B}}}$. [Diewald et al. 2020b]	62
5.4	The domain \mathcal{B} is discretized with finite elements \mathcal{B}_e . The reference element \mathcal{B}_{\square} represents a finite element in natural coordinates with $\xi \in [-1, 1]$ and $\eta \in [-1, 1]$	64
5.5	Sketch of the discretization for the dynamic Navier-Stokes-Korteweg model for two-dimensional scenarios (Q2P1). The contributions on $\partial\mathcal{B}_e \cap \partial\mathcal{B}_s$ are addressed by additional line elements.	71
5.6	A subprogram computes (5.87) and (5.88). Input: $\bar{\rho}_{\text{hd}} = \rho(\vec{\xi}_p) + \epsilon_1 h_1 + \epsilon_2 h_2 + \epsilon_1 \epsilon_2 0$. Output: derivatives with respect to ρ at quadrature point.	75
6.1	Droplet on plane surface. The plots show iso-surfaces of the computed equilibrium configurations for the first set of surface tensions that leads to a theoretical contact angle of $\Theta = 60^\circ$ (left) and for the second set of surface tensions that leads to a theoretical contact angle of $\Theta = 150^\circ$ (right). The contact angles of the computed equilibrium configurations represent the theoretical contact angles. .	78
6.2	Contour plots of φ for droplet on spikes (left column) and iso-surfaces for droplet on circular pedestal (right column) at different relaxation times t . The top row shows the initialization states and the bottom row the static equilibrium. [Diewald et al. 2016, 2017] .	80
6.3	Droplet without surface contact. Top: Contour plots of $\vec{\rho} + \vec{s}_i$ for coarse mesh. Bottom: Eigenvalues with smallest absolute values for coarse and medium mesh. [Diewald et al. 2018b]	84
6.4	Droplet with surface contact. Top: Contour plots of $\vec{\rho} + \vec{s}_i$ for coarse mesh. Bottom: Eigenvalues with smallest absolute values for coarse and medium mesh. [Diewald et al. 2018b]	85
6.5	(a), (b): Contour plots of the static equilibrium configurations for first and second initialization and $\Theta = 90^\circ$, respectively. (c): Contour plot of $\vec{\rho} + \vec{s}_1$ for droplet on edge of pedestal and $\Theta = 90^\circ$. (d): Energy for droplet on edge and top of pedestal and different contact angles. (e), (f): Eigenvalues with smallest absolute values for droplet on edge and top of pedestal and $\Theta = 90^\circ$. [Diewald et al. 2018b]	87
6.6	Phase separation. Iso-surfaces of ρ for different times t . The first plot shows the initialization state with a random density distribution. The last plot shows the static equilibrium configuration. [Diewald et al. 2018a]	90

6.7	Planar interface. (a): Density profiles over a straight line that runs through the center of the computational area and is perpendicular to the interface for PF and MD simulations at three temperatures. The dashed line shows the initialization state of the PF simulations. (b): Comparison between the interface widths definitions l^{10-90} and l^t . (c): Comparison between the values for the surface tension γ_{lv} as obtained from the PF simulations and reported in [Vrabec et al. 2006] at three temperatures. [Diewald et al. 2018a]	91
6.8	Liquid droplet in vapor phase with $m_B = 800M^{LJ}$ at $T = 0.7\frac{\epsilon^{LJ}}{k_B}$. Contour plot of the static equilibrium configuration (left) and comparison of the liquid and vapor densities obtained from the PF simulation to the values obtained from MD simulations (right). [Diewald et al. 2018a]	94
6.9	Liquid droplet in vapor phase. Initialization state (left) and the static equilibrium state (right) for $r_{ini} = 3\sigma^{LJ}$ (top) and $r_{ini} = 5\sigma^{LJ}$ (bottom). The droplet disappears for small r_{ini} values and a homogeneous density distribution is obtained. [Diewald et al. 2018a]	95
6.10	Liquid droplet in vapor phase. Left: Approximation of the interface between the liquid and the vapor phase by a linear transition from ρ' to ρ'' . Right: Analytic total PF potential for droplet in vapor phase (F_d) and homogeneous density distribution (F_h). The symbols show the total PF potential as obtained from the PF simulations. [Diewald et al. 2018a]	96
6.11	Liquid droplet in vapor phase. Left: Equimolar radius in the static equilibrium configuration over the total mass. Right: Pressure difference resulting from the PF simulations and pressure difference resulting from the Young-Laplace equation over the equimolar radius. [Diewald et al. 2018a]	98
6.12	Wetting of structured surface. The snapshots of the temporal evolution show the impact of a droplet on a structured surface with $\Theta = 90^\circ$ (left) and $\Theta = 150^\circ$ (right). [Diewald et al. 2019]	100
6.13	Sketch of droplet on surface with wettability gradient. A gradient of $\gamma_{sl} - \gamma_{sv}$ leads to different contact angles on the left and right side of the droplet and thus to a droplet motion. Two different slopes for $\gamma_{sl} - \gamma_{sv}$ are considered. [Diewald et al. 2020a]	102
6.14	Droplet on surface with wettability gradient. Snapshots of the PF and (mirrored) MD simulation for the first scenario. The first plot shows the initialization state and the last plot the static equilibrium configuration. [Diewald et al. 2020a]	104

6.15	Droplet on surface with wettability gradient. MD and PF results for the temporal evolution of the centroid and the velocity in x -direction. [Diewald et al. 2020a]	105
6.16	Oval droplet initialization. (a): Contour plots of ρ at different times t for the SI scheme with $\Delta t = 10^{-2} \sigma^{\text{LJ}} \sqrt{M^{\text{LJ}}/\varepsilon^{\text{LJ}}}$. (b): Energy evolution of the BE and SI scheme with different time step sizes. The solid lines show the BE results and the dashed lines the SI results. The colors indicate the time step size. The curves for the BE results are lying almost on top of each other. (c): Energy evolution of the SI scheme with different values for the stabilization parameter. [Diewald et al. 2020b]	108
6.17	Falling droplet. (a, b): Contour plots of ρ at different times t for the SI scheme with $\Delta t = 10^{-2} \sigma^{\text{LJ}} \sqrt{M^{\text{LJ}}/\varepsilon^{\text{LJ}}}$ (a) and $\Delta t = 10^1 \sigma^{\text{LJ}} \sqrt{M^{\text{LJ}}/\varepsilon^{\text{LJ}}}$ (b). (c, d): Energy evolution of the BE and SI scheme with different time step sizes up to $t = 100 \sigma^{\text{LJ}} \sqrt{M^{\text{LJ}}/\varepsilon^{\text{LJ}}}$ (c) and for the SI simulations with the two largest time step sizes up to $t = 1000 \sigma^{\text{LJ}} \sqrt{M^{\text{LJ}}/\varepsilon^{\text{LJ}}}$ (d). The solid lines show the BE results and the dashed lines the SI results. The colors indicate the time step size. The crosses mark the termination point of the simulations for which the Newton-Raphson method does not converge. [Diewald et al. 2020b]	110
7.1	Left: Plot of the local part of the EoS based and scaled Helmholtz free energy density for different values of α^{scal} and $T = 0.7 \frac{\varepsilon^{\text{LJ}}}{k_{\text{B}}}$. Right: Plot of the scaled homogeneous excess free energy density. The scaling does not alter the Helmholtz free energy densities for ρ' and ρ''	115
7.2	Sketch of methane droplet on tilted surface with wettability gradient.	118
7.3	Methane droplet on tilted surface with wettability gradient. Velocity over relative position for different values of p^{scal}	118

Liste der betreuten studentischen Arbeiten mit Bezug zur Dissertation

- Teto, J. O. D. (2018). *FE-Implementierung eines Phasenfeld-Elements zur Modellierung der Wechselwirkung zwischen Fluiden und Festkörpern*. Bachelorarbeit, Technische Universität Kaiserslautern.
- Bilz, R. (2018). *Implementierung eines 3D Finite Elemente Modells zur Beschreibung der Dynamischen Benetzung von Oberflächen*. Diplomarbeit, Technische Universität Kaiserslautern.
- Gellrich, M. (2019). *A Better VTU Output Routine for the Finite Element Analysis Program (FEAP)*. Bachelorarbeit, Technische Universität Kaiserslautern.
- Kneip, L. (2019). *Finite Elemente Untersuchung zum Einfluss der Längenskala auf die Tropfenform bei Oberflächenbenetzung*. Bachelorarbeit, Technische Universität Kaiserslautern.

Lebenslauf

Name: Felix Diewald

Geburtsdatum: 25.12.1989

Geburtsort: Kaiserslautern

Staatsangehörigkeit: deutsch

1996 – 2000 Carl-Bosch-Grundschule, Frankenthal

2000 – 2009 Albert-Einstein-Gymnasium, Frankenthal
2009 Abitur

2009 – 2010 Zivildienst als Rettungssanitäter beim ASB, Ludwigshafen

2010 – 2015 Studium Maschinenbau,
Technische Universität Kaiserslautern
2015 Diplom

seit 2015 Wissenschaftlicher Mitarbeiter,
Lehrstuhl für Technische Mechanik, Prof. R. Müller,
Technische Universität Kaiserslautern